NTNU – Trondheim
Norwegian University of
Science and Technology

Numerical Simulations of Viscous Flow Around Stepped Circular Cylinder

Rune Bjørkli

Marine Technology
Submission date: June 2012
Supervisor: Bjørnar Pettersen, IMT

Norwegian University of Science and Technology
Department of Marine Technology

Summary

A stepped cylinder could be a desired design for an offshore buoy or SPAR platform. The geometry of a stepped cylinder consists of a small diameter cylinder (d) placed on top of a large diameter cylinder (D). This master thesis has investigated numerically the flow around a stepped cylinder with different diameter ratios (d/D) for a Reynolds number, $Re_D = 150$. The commercial software *Fluent v13.0* by Ansys was used for the numerical investigation.

The aim of the study has been exploring the nearby wake flow as well as the region where the two cylinders are joined. The hydrodynamic forces and vortex shedding frequency have been analysed and compared for the four different diameter ratios: d/D = 0.3, 0.5, 0.8 and 0.9

The major part of the published papers on the topic is based on experimental studies. Only two papers are based on numerical studies, having considered d/D = 0.5 exclusively. Earlier studies have focused mainly on vortex shedding in the wake flow, omitting the forces acting on the stepped cylinder.

The stepped cylinder has been modelled using the software GAMBIT. A convergence study investigating the domain size and element density was conducted to ensure a grid independent solution. Special attention was directed at the step region to fully resolve the complex flow in this region. The numerical model was verified to be in good agreement with previous experimental- and numerical studies.

For the stepped cylinders significant spanwise velocity was detected in the step region. For d/D = 0.3 and 0.5, upflow was detected over the leading edge of the step whereas downwash characterised the trailing edge of the step. Similarities to the flow around a finite length cylinder could be drawn for d/D = 0.3 and 0.5, whereas d/D = 0.8 and 0.9 resembled that of a straight cylinder.

The step was found to affect the wake flow $\approx$ 10D into D independent of diameter ratio. The wake flow behind the small diameter cylinder was less affected by the step than the large for d/D $<$ 0.5. In the step region two distinct streamwise vortices were detected. A pair of edge vortices as well as a junction vortex were readily detected for d/D = 0.3 and 0.5. The junction vortex was not detected for d/D = 0.8 and 0.9 due to the small step change in diameter.

The drag force on D was found to increase as d/D increased. Similarly, the amplitude of the lift force was also found to increase as d/D increased. The mean drag-coefficient varied along the span with peaks in the local drag-coefficient observed in close vicinity of the step.

Regular spanwise vortex shedding was detected away from the step at a frequency similar

to that of a straight cylinder. In the step region, located mainly on D, a cell of lower vortex shedding frequency was detected for d/D = 0.3 and 0.5. As d/D increased this cell seemed to disappear. Suppression of regular vortex shedding close to the step for d/D = 0.3 was observed for $Re_D = 150, 300$ and 600. For $Re_D > 150$ the large spanwise vortex structures were still discernible, but the presence of small-scale streamwise vortices complicated the flow.

Preface

This report is the result of my master thesis written at the Department of Marine Technology at the Norwegian University of Science and Technology. The report contains work conducted over the last 5 months during the spring of 2012.

When I visited my supervisor the autumn of 2011 I was immediately mesmerized by the suggested topic for the project and master thesis: ”flow around a stepped cylinder.” What caught my attention first was how the wake flow behind such a structure would be like. From my year studying abroad I was introduced to computational fluid dynamics (CFD), which was selected as the desired *tool* for this master thesis.

My experience using CFD as a tool I would say have increased exponentially while working on the master thesis. A lot of knowledge has been gained in creating grids, along with skills in extracting data and post-processing. Another issue is to judge the accuracy of the CFD results, and quite some time was spent troubleshooting bad results.

I would like to thank the following persons, both for their time, but also for valuable (and time saving!) tips and motivation:

- Professor Bjørnar Pettersen (supervisor)
- Pål Levold (for his invaluable expertise in general computing and fruitful discussions)
- Tufan Arslan (PhD candidate. Fluent- and gridding expert)
- Ina Teutsch (fellow student doing PIV experiments on a stepped cylinder)

Rune Bjørkli

Trondheim

(June 10, 2012)

NTNU
Norges teknisk-naturvitenskapelige universitet
Institutt for marin teknikk

HOVEDOPPGAVE I MARIN HYDRODYNAMIKK

VÅR 2012

FOR

Stud.techn. Rune Bjørkli

NUMERISK SIMULERING AV VISKØS STRØMNING OMKRING SIRKULÆR SYLINDER MED VARIERENDE DIAMETER
(Numerical simulations of viscous flow around stepped circular cylinder)

Studenten skal gjøre en litteraturstudie og redegjøre for eksperimentelle og numeriske resultater som foreligger.
I samråd med veileder velges parametere knyttet til geometri og strømningen. Programmet Fluent skal brukes i simuleringen. I forbindelse med modelleringen skal det gjøres grid-konvergensstudier.
Strømningen i nær-waken skal kartlegges for forskjellige geometrier. Spesielt skal området nært steppet studeres. Visualiseringsmetodene som brukes skal redegjøres for.
I den grad tiden tillater det skal det gjøres sammenlikninger med eksperimentelle resultater fra Sirkulasjonstanken.

Kandidaten skal i besvarelsen legge frem sitt personlige bidrag til løsning av de problemer som oppgaven stiller. Påstander og konklusjoner som legges frem, skal underbygges med matematiske utledninger og logiske resonnementer der de forskjellige trinn tydelig fremgår. I besvarelsen skal det klart fremgå hva som er kandidatens eget arbeid, og hva som er tatt fra andre kilder.
Kandidaten skal utnytte de muligheter som finnes til å skaffe seg relevant litteratur for det problemområdet kandidaten skal bearbeide.
Besvarelsen skal være oversiktlig og gi en klar fremstilling av resultater og vurderinger. Det er viktig at teksten er velskrevet og klart redigert med tabeller og figurer. Besvarelsen skal gjøres så kortfattet som mulig, men skrives i klart språk.
Besvarelsen skal inneholde oppgaveteksten, forord, innholdsfortegnelse, sammendrag, hoveddel, konklusjon med anbefalinger for videre arbeid, symbolliste, referanser og eventuelle vedlegg. Alle figurer, tabeller og ligninger skal nummereres.
Det forutsettes at Institutt for marin teknikk, NTNU, fritt kan benytte seg av resultatene i sitt forskningsarbeid, da med referanse til studentens besvarelse.

Besvarelsen leveres innen 11. juni 2012.

Bjørnar Pettersen
Professor

Faglig veileder: Stipendiat Tufan Arslan

Contents

Nomenclature

Δy	The distance to the first grid element normal to the body
δ	Boundary layer thickness
μ	Dynamics viscosity
ν	Kinematic viscosity
ω_x	Streamwise vorticity $= (\frac{\partial w}{\partial y} - \frac{\partial v}{\partial z})$
ω_y	Vorticity in x-z-plane $= (\frac{\partial u}{\partial z} - \frac{\partial w}{\partial x})$
ω_z	Spanwise vorticity $= (\frac{\partial v}{\partial x} - \frac{\partial u}{\partial y})$
$\overline{C_D}$	Mean drag-coefficient $= \overline{F_D/0.5\rho V^2 A}$
$\overline{C_f}$	Mean friction coefficient $= \overline{\tau_{wall}}/0.5\rho U_\infty^2$
ρ	Fluid density
τ_w	Tangential wall shear stress $= \mu du/dy$
θ	Angular distance measured from forward stagnation point in degrees
C_D	Dimensionless drag force $= F_D/0.5\rho U^2 A$
C_L	Dimensionless lift force $= F_L/0.5\rho U^2 A$
C_p	Pressure coefficient $= (p - p_\infty)/0.5\rho U^2$
C_L r.m.s	Root-mean-square value of C_L
F_D	Drag force
F_L	Lift force
f_v	Vortex shedding frequency $= 1/s$
N_r	Number of elements in the radial direction normal to the cylinder
N_θ	Number of elements in the circumferential direction
St	Dimensionless vortex shedding frequency $= f_v D/U$
T_v	Vortex shedding period
U	Inviscid free stream velocity

u	Velocity in x-direction
v	Velocity in y-direction
w	Velocity in z-direction
AR	Aspect ratio
D	Large cylinder diameter
D	Large diameter cylinder
d	Small diameter cylinder
DNS	Direct numerical simulation
L	Length of large diameter cylinder D
l	Length of small diameter cylinder d
Lx	Distance from cylinder center to velocity inflow boundary
Ly	Distance from cylinder cetner to lateral boundary
Re	Reynolds number = UD/ν
t	Flow-time in seconds
U	Uniform flow velocity

Abbreviations

2-D Two-dimensional
3-D Three-dimensional
CFD fluid dynamics
DES Detached-Eddy Simulation
LES Large-Eddy Simulation
PIV Particle Image Velocimetry
RANS Reynolds-Averaged Navier-Stokes
Re Reynolds number
URANS Unsteady Reynolds-Averaged Navier-Stokes

Chapter 1

Introduction

The circular cylinder is a central building component in most marine structures. Almost all semi-submersibles have circular cylinders as columns, whereas the hull of SPAR-buoys solely consists of a circular cylinder. Pipes carrying the oil from the sea-bed to the process plant are all of cylindrical shape although having a smaller cross section. Further, as onshore windmill parks are moved offshore, circular cylinders are a typical underwater hull design. In addition to extensive use offshore, the circular cylinder is a common engineering application onshore; chimneys, television towers and radio masts all represent utilisation of a circular cylinder shape.

Owing to its many engineering applications, numerous papers have been published during the last decade regarding the flow around circular cylinders. Indeed, several papers are entirely devoted to revising the state of the art (see for example Berger and Wille (1972); Niemann and Hölscher (1990); Roshko (1993)).

The flow around a circular cylinder is characterised with a large and usually unsteady flow, thus it is in the literature commonly described as a *bluff body* (Zdravkovich, 1997). In the wake region, downstream of the separation point, bluff bodies experience similarities in the development of flow structures. These large flow structures, known as *vortices*, are formed in the near wake and shifted downstream and eventually decay due to viscous dissipation (Zdravkovich, 1997).

The wake region has been the emphasis of most past research. Recent studies have discovered three-dimensional flow effects in the cylinder wake at low Reynolds numbers ($Re \sim 194 - 260$), which has lead to new insight in opposition to flows believed to be nominally two-dimensional (Williamson, 1996).

In his study of vortex dislocations, Williamson (1992) passively generated vortex dislocations by placing a small ring disturbance at the midspan of a circular cylinder. Asymmetric 'one-sided' vortex dislocations were created between two adjacent cells of different vortex shedding frequency as they moved out of phase. Due to a step change in diameter, one-sided vortex dislocations are assumed to be present for flow around stepped cylinders.

The geometry of a stepped cylinder consists of a small diameter cylinder (d) placed on top of a large diameter cylinder (D). One-sided vortex dislocations are thus expected to occur due to a difference in vortex shedding frequency in the wake of a stepped cylinder. Contrary to tapered cylinders with multiple vortex interaction zones, the interaction of vortex filaments are for a stepped cylinder restricted to the step. Lewis and Gharib (1992)

investigated a series of high aspect ratio stepped cylinders, with diameter ratios (d/D) in the range $0.87 - 0.56$ for Reynolds numbers, $Re \sim 35 - 200$. Two distinct sorts of wake behaviour, named as *mode A* and *mode B* was identified in the wake flow. The different modes were found to be function of Reynolds number and diameter ratio with different cells of vortex shedding frequency along the span.

Dunn and Tavoularis (2006) have performed experiments and thorough flow visualisation on a stepped cylinder with a diameter ratio $d/D = 0.51$. The Reynolds number based on D ($Re_D = UD/\nu$) was in the range $63 - 1100$. A wake behaviour similar to the indirect mode detected by Lewis and Gharib (1992) was observed. Away from the step, two-dimensional vortex shedding detected at vortex shedding frequencies similar to that of a straight cylinder. Close to the junction between the d and D, a cell of much lower shedding frequency was detected occurring (Dunn and Tavoularis, 2006; Lewis and Gharib, 1992; Norberg, 1992).

In addition to regular spanwise vortices, two types of streamwise vortices have been detected in the stepped cylinder wake. A pair of edge vortices rolled up over the edge of the D whereas a junction vortex was observed wrapping around the base of d (Dunn and Tavoularis, 2006). The edge vortex may be the same as found by Kawamura et al. (1984); Park and Lee (2000); Sumner et al. (2004) in the wake of a finite length cylinder characterised as two distinct streamwise counter-rotating tip vortices, separating at the free end.

The combination of both spanwise- and streamwise vortices enriches the wake flow making an understanding of the flow physics complex. The present thesis will thus perform a study of the flow around stepped cylinders using a numerical solver. The strengths of a numerical solver is that velocities and pressure are readily known in the whole fluid domain at each step in time, thus being a powerful tool in gaining further understanding of the problem. Stepped cylinders with different diameter ratio (d/D) will be analysed at low Reynolds numbers, $Re_D = 150$, using the commercial code Fluent v13.0 by Ansys.

1.1 Motivation

The Reynolds number employed in the present thesis ($Re_D < 600$) represents an idealistic case and does not represent real conditions. In real life conditions the Reynolds number on a SPAR buoy (figure 1.1 page, 3) of diameter, say, D = 50m in a current of U = 1 m/s is in the range of 50×10^6. The current study will be positioned in the *laminar* flow regime whereas real life conditions *always* include turbulence.

Regardless of difference in Reynolds number, studying the physics of the problem and the qualitative behaviour of the flow problem is important. The quantitative values of the drag-coefficient may not be similar as for a full-scale Reynolds number, but the basic flow physics *may* be similar.

It is in the author's interest to conduct a numerical study of the problem. The author

believes that computational fluid dynamics (CFD) in the future will be a valuable asset to study flow phenomena connected to marine structures. Gaining knowledge and experience through using CFD program is thus advantageous and has been a motivation for selecting a numerical study.

Figure 1.1: Aker Solutions idea of a SPAR platform with a stepped cylinder design producing oil at a record depth of 1300 meters. To give an impression of its size the platform is compared against high-rise buildings in Oslo. Reprinted from www.aftenposten.no, PHOTO: Aker Solutions/Giga pix AS

1.2 Scope of thesis

1.2.1 Disposition of thesis

- **Chapter 2** starts with a review available literature on the topic of flow around a circular cylinder. Important fluid mechanic phenomena such as flow separation and vortex shedding are reviewed. The chapter continues by studying literature concerning the flow around tapered and finite length cylinders to investigate their relationship to a stepped cylinder. The chapter concludes by studying published literature on the flow around a single stepped cylinder and a dual stepped cylinder.
- **Chapter 3** is devoted to the modelling process of a stepped cylinder. A sensitivity study of the model is performed in a grid convergence study. The chapter concludes on model(s) that are to be used in the numerical simulation.
- **Chapter 4** validates the solution against published experimental results, in order to gain confidence that the physics are correctly represented.
- **Chapter 5** presents- and discusses the results from simulations of the flow around a stepped cylinder with different diameter ratios. The variations in wake flow for the different diameter ratios, as well as the flow around the step change in diameter are studied.
- **Chapter 6** concludes the findings of the thesis and relates the findings to marine applications. The thesis ends by a recommending further work related to flow around stepped cylinders.

1.2.2 Research questions

- **Streamwise vortices**. How are the streamwise vortices detected at the step affect by a change in diameter?
- **Forces**. How are the hydrodynamic forces (drag-forces and lift-forces) distributed along the span of the stepped cylinder?
- **Vortex shedding**. By performing a frequency analysis and visualising vortices through vortex identification schemes, how is the wake vortex structures affected by a change in diameter?

Chapter 2

Literature Review

Before embarking the study of flow around a stepped cylinder, it may be beneficial to study flow around other similar structures. To some extent, vortex dislocations as observed for stepped cylinders, are also distinguished in the wake of tapered cylinders. Furthermore, the flow around the free end of a finite length cylinder may resemble the flow close to the junction between the small- and large cylinder in a stepped cylinder setup.

However, in understanding the wake flow of any cylindrical body, it is worth revisiting some fundamental fluid mechanics and flow physics as well. Section 2.1 in the present chapter thus gives a review of some basic properties of fluid flow. Section 2.1.3 and 2.1.4 focus on flow separation and vortex shedding characteristic for a *bluff body*[1]. Section 2.2 describes the flow around a circular cylinder, followed by sections 2.3 and 2.4 describing the flow around tapered and finite length cylinders, respectively. The flow around a stepped cylinder is then explored in section 2.5 by studying key references. Lastly, the flow around a dual stepped cylinder has been investigated in section 2.6 due to its equivalence to a stepped cylinder.

2.1 Fluid flow

Considered as one of the biggest breakthroughs in fluid mechanics is the paper by Ludwig Prandtl in 1904 (White, 2006). Prandtl showed that viscous effects were only confined to a narrow region near the solid body, named *boundary layer*. Outside the thin *boundary layer* the flow can be considered inviscid, and several well-known mathematical models can be employed (for example Euler's equation). The discovery made by Prandtl is valid for fluids with small viscosity, such as air and water.

2.1.1 Potential flow

Previous to Prandtl's discovery much effort was put in describing viscous flow as inviscid, thus neglecting the boundary layer. Potential flow theory treats the fluid as irrotational, incompressible and inviscid. The latter fact results in a non-existing boundary layer close to the body. Potential flow theory gives reasonable results outside the boundary layer, as found by Prandtl, but due to zero viscosity the drag force on the

[1] A bluff body is one in which the length in the flow direction is close to or equal to the length perpendicular to the flow direction. The wake is characterised by separated and unsteady flow.

body will be zero. Jean d'Alembert demonstrated this in 1752 (*d'Alemberts paradox*) that a body fully submerged in a frictionless fluid would have zero drag force (White, 2006). The variation of the pressure coefficient, $C_p = (p - p_\infty)/0.5\rho U^2$, along the circumference of a circular cylinder, calculated by the frictionless Bernoulli equation valid for potential flow theory, is shown in figure 2.3 , page 8.

2.1.2 Boundary layer

A real fluid does not behave like the inviscid fluid conceptualised in potential flow theory. At the body surface the fluid velocity must go to zero, due to intermolecular attractions that causes the fluid to stick to the wall (Schlichting, 1979). A boundary layer is defined between the body and the free-stream, in which the velocity is gradually increased from zero (on the body) to the free stream velocity outside the boundary layer. The thickness of the boundary layer, δ, is therefore defined as the point where the local fluid velocity, u, is equal to the free stream velocity, U, outside the boundary layer at that point, $u(y) = 0.99U(x)$. Inside the boundary layer viscous effects are important, as the tangential shear stress at the wall, $\tau_w = \mu du/dy$, depends on the velocity gradient du/dy. Additionally the existence of a boundary layer is the reason to why the flow separates and the wake flow becomes unsteady.

Figure 2.1(a) shows velocity vectors plotted at $\theta = 10, 30, 60, 90, 120, 150$ on top of the mean velocity magnitude at Reynolds number, $Re_D = 150$. The boundary layer is identified in the velocity vectors and the velocity magnitude contour plot, the thickness of δ increasing downstream. At $\theta \approx 120$ the fluid separates from the cylinder surface. Figure 2.1(b) shows details of the velocity profiles close to the cylinder surface, at $\theta = 110, 120, 130, 140, 150$, as well as streamlines showing the fluid particle path in this region. Backflow is identified at $\theta = 130$ along with a rotating vortex identified by pathlines.

The thickness of the boundary layer for a circular cylinder can be approximated as the ratio of the cylinder diameter, D, to the square-root of the Reynolds number.

$$\delta = \frac{D}{\sqrt{Re}} \tag{2.1}$$

2.1.3 Flow separation

Flow separation occurs when the boundary layer separates from the body. Downstream of the separation point, the fluid particles close to the body flow in the upstream direction so that vortices are formed and shed into the wake. Due to flow separation, the wake flow is chaotic and the pressure in the wake is lower than at the front of the cylinder. The net difference in pressure upstream and downstream of a cylinder (figure 2.3, page 8) creates a pressure induced *drag-force* when integrated over the cylinder surface, acting in the flow direction. A frictional drag-force, due to wall shear stress, exists as well - but is for bluff bodies at high *Re* considered being small when compared to the pressure-induced drag-force.

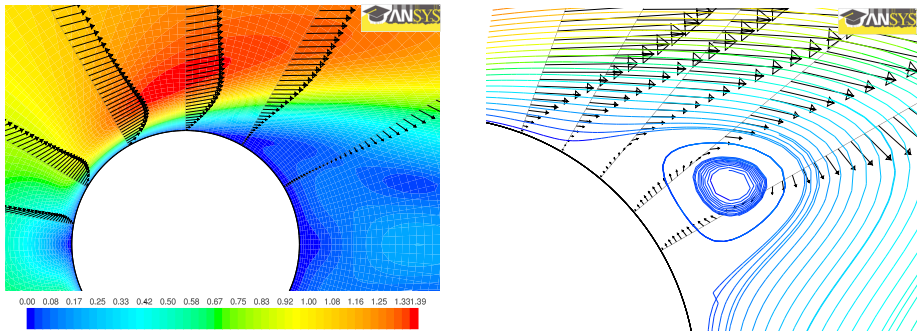

(a) Boundary layers at radial positions, $\theta = 10, 30, 60, 90, 120, 150$ plotted on top of a contour plot of the mean velocity magnitude.

(b) Details of the boundary layer at radial positions, $\theta = 110, 120, 130, 140, 150$ along with pathlines showing the fluid particle path.

Figure 2.1: Boundary layer at different radial positions on the cylinder surface, illustrated by velocity vectors. The flow visualisation is obtained from the two-dimensional simulation. $Re_D = 150$.

The mechanism behind flow separation is associated with the pressure distribution within the boundary layer. Schlichting (1979) gives the following physical explanation; Outside the boundary layer potential flow theory is assumed to be valid, so that the pressure distribution follows that of figure 2.3. One then assumes that the pressure variation over the width of the boundary layer is small, and that the pressure magnitude is similar to that outside of the boundary layer. A fluid particle moving in the immediate vicinity of the wall in the boundary layer thus remains under the same pressure field that exists outside the boundary layer, predicted by potential flow theory. As the fluid is accelerated towards a maximum at the top of the cylinder, $\theta = 90$, the pressure is at minimum (figure 2.3), *the pressure is transformed into kinetic energy*. As the fluid particle travels from $\theta = 90$ to 180 they are decelerated to merge with the ambient flow, the pressure increases, *kinetic energy is transformed into pressure*. Outside the boundary layer, at $\theta = 180$, the pressure is fully *recovered*. However, for the fluid particles in the immediate vicinity to the body, friction causes a *loss* in kinetic energy when the fluid particles travels from $\theta = 0$ to 90. The remainder of kinetic energy is therefore not large enough to overcome the increase in pressure on the downstream side of the cylinder, as the particles travels from $\theta = 90$ to 180. As a consequence, the motion of the fluid particles close to the surface eventually stops before reaching $\theta = 180$, and the pressure will cause a backward motion; the boundary layer separates and moves sideways from the wall (figure 2.1(b)). The fluid particles behind the point of separation generally follow the pressure gradient and moves in the direction opposite to the ambient flow. The fact that the pressure is not fully recovered is seen in figure 2.3 (as plotted in red) and is the reason for high drag-forces for flow around bluff bodies.

Figure 2.1(b) shows flow separation somewhere between $\theta = 110$ and 120. Downstream of the separation point, close to the body, backward flow is observed, causing the formation of a vortex (indicated by pathlines as a circle). Around the separation point the boundary layer thickness is observed to increase, and the separated flow follows the

separation streamline (indicated by an arc outside the vortex). Thus, the point of separation can be defined as the limit between forward and reverse flow in the immediate vicinity of the body. It may also be thought of as the point where the wall shear stress (section 2.1.2) is zero. Separation thus occurs if $\partial u/\partial y = 0$. Contrary, the flow sticks to the body in the opposite case, $\partial u/\partial y \geq 0$. Figure 2.4 depicts both cases for flow around a cylinder at Re = 150; $\partial u/\partial y$ is positive and at a maximum at $\theta = 60$ whereas the flow separates when $\partial u/\partial y = 0$ at $\theta = 114$.

Velocity profiles at $\theta = 60, 120, 130$ are illustrated in figure 2.2. For $\theta < 90$ the flow is accelerating and the pressure is dropping. A *favorable* pressure gradient exists, $dp/dx < 0$, and the flow is not separating ($\theta = 60$ in figure 2.2). For $\theta > 90$ the velocity is decelerating in order to merge with the ambient flow so that pressure is increasing. An *adverse* pressure gradient $dp/dx > 0$ exist close to the body and the profiles become more S-shaped ($\theta = 120, 130$ in figure 2.2). The adverse pressure gradient eventually retards the flow causing it to separate and make it go backward as seen close to the cylinder wall at $\theta = 130$ in figure 2.2. The inflexion point in the velocity-profile curves mark when the sign of dp/dx changes from positive to negative, due to merging with the free-stream velocity outside the boundary layer. Thus, if the velocity profile has an inflexion point flow separation is most likely present.

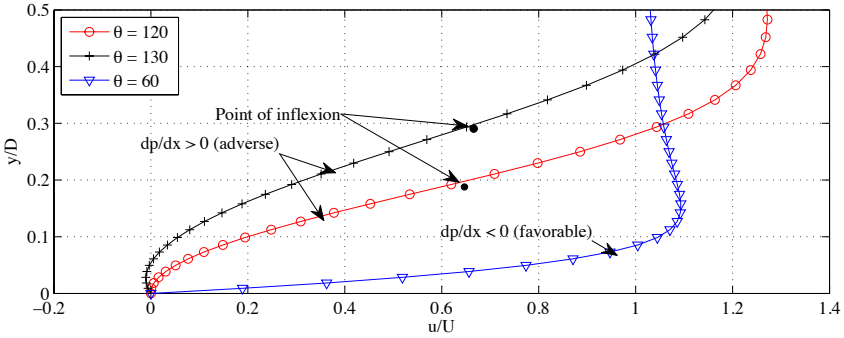

Figure 2.2: Velocity profiles in the boundary layer for $\theta = 60, 120, 130$. $Re_D = 150$

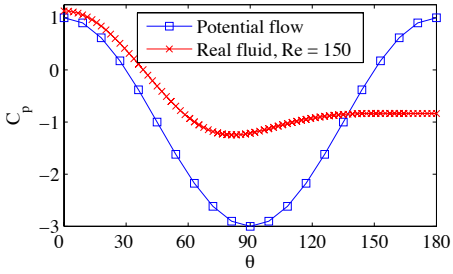

Figure 2.3: Pressure-coefficient calculated with potential flow theory compared with that obtained from a numerical simulation for flow around a cylinder compared. $Re_D = 150$.

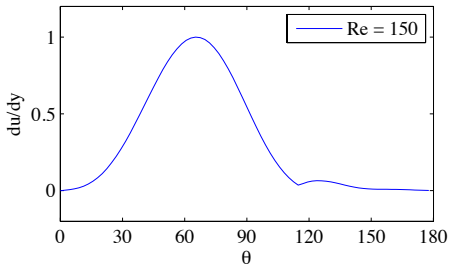

Figure 2.4: Velocity gradient, $\partial u/\partial y$, plotted along the cylinder circumference for $Re_D = 150$.

2.1.4 Vortex shedding

Most viscous flows separate when exposed to an adverse pressure gradient (Schlichting, 1979). The adverse pressure gradient is caused by the divergent geometry of the downstream side of the cylinder (Sumer and Fredsøe, 1997). For the flow around a circular cylinder for $Re > 49$ vortex shedding occurs as a result of flow separation. (Sumer and Fredsøe, 1997) give the following physical explanation to the mechanism behind vortex shedding.

For a viscous flow a typical boundary layer profiles are given in figure 2.2. The velocity gradient $\partial u/\partial y$, as discussed above, is large in the close vicinity of the body and reduces into the fluid. Hence, the vorticity is high within the boundary layer (section 3.6.1, page 35). Downstream of the separation point, vorticity is fed into a shear layer that causes the shear layer to roll up into a vortex, its sign matching the entering vorticity. Similarly, vorticity of the opposite sign is fed into the shear layer on the other side of the cylinder.

Due to its unstable nature ($Re > 49$), one of the vortices will grow larger than the other. The stronger vortex (A) will then be able to draw the opposite vortex (B) across the wake. As the vortex of opposite sign (B) crosses the wake it will cut the supply of vorticity to the initial stronger vortex (A). The cut-off in vorticity supply leads to the shedding of vortex A. Taking the place of vortex A, vortex C is now drawn across the wake in a similar manner by the increased strength of vortex B. Vortex C cuts the supply of vorticity to vortex B that leads to the shedding of vortex B.

The above process will now continue in a periodic alternating manner between the upper and lower side of the cylinder, as shown by contour plots of vorticity magnitude in figure 2.5 page 10.

Vortex shedding frequency

Vortex shedding is a periodic behaviour as discussed in section 2.1.4. The vortex shedding frequency, f_v, is defined as the cycle ($[1/second]$) between vortices shed from the same side of the cylinder. The time between two successive vortices shed from the same side of the cylinder is thus the vortex shedding period, T_v (vortex A and C in figure 2.5). If one considers the alternating shedding of vortices from both sides of the cylinder, the time between the shedding of two vortices are $T_v/2$ (vortex A and B in figure 2.5).

The shedding of vortices results in pressure differences between the upper and lower side of the cylinder resulting in a lift force acting perpendicular to the flow direction. Due to the alternating manner of the vortex shedding this lift force changes between acting in the negative and positive direction, perpendicular to the flow-direction. The lift force is seen oscillating with the vortex shedding frequency in figure 2.6 page 11, where $C_L = F_L/0.5\rho U^2 A$ represents the dimensionless lift force. The dimensionless drag force, $C_D = F_D/0.5\rho U^2 A$, is in the same figure seen oscillating with a frequency twice the shedding frequency, $2T_v$. Note that the mean value of the lift force is zero whereas the mean drag-force is non-zero.

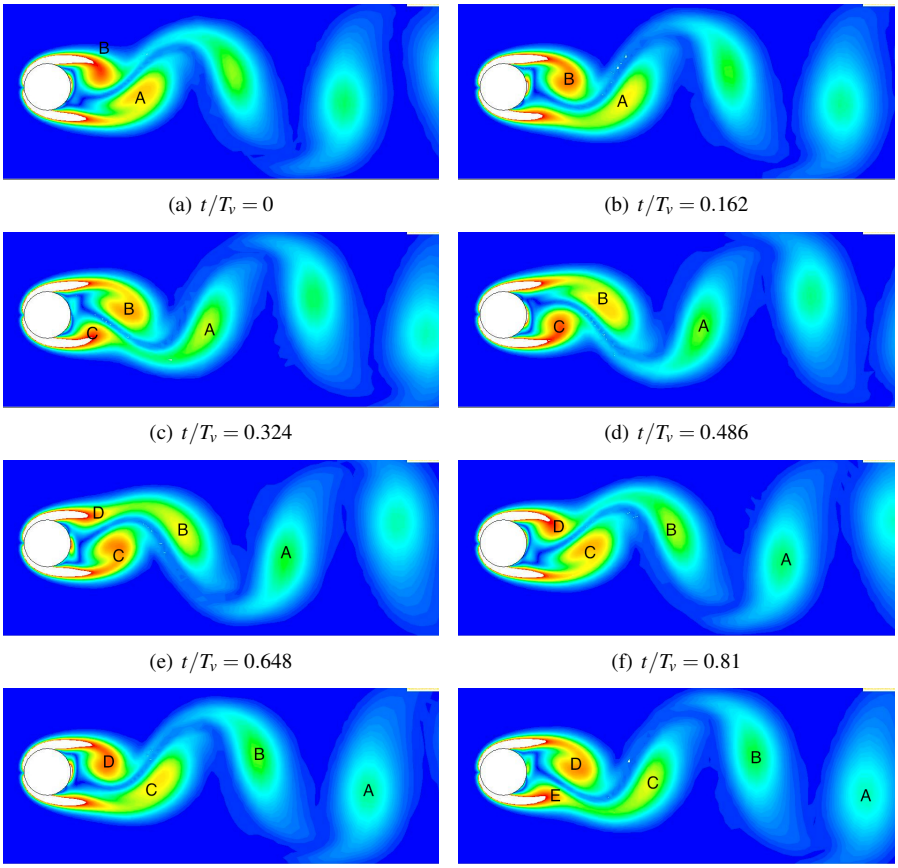

(a) $t/T_v = 0$ (b) $t/T_v = 0.162$

(c) $t/T_v = 0.324$ (d) $t/T_v = 0.486$

(e) $t/T_v = 0.648$ (f) $t/T_v = 0.81$

(g) $t/T_v = 0.972$ (h) $t/T_v = 1.134$

Figure 2.5: Contour plots of vorticity magnitude showing periodic vortex shedding in the wake of a circular cylinder at Re = 150. T_v represents the vortex shedding period and t, flow time in seconds.

By normalising the vortex shedding frequency using the inflow velocity U and the cylinder diameter D, *Vincenc Strouhal* found in 1878 the following dimensionless expression for the vortex shedding frequency:

$$\text{Strouhal number, St} = \frac{f_v D}{U} \tag{2.2}$$

The Strouhal number, St, is a function of the Reynolds number and the St-Re relationship for low Reynolds (Williamson, 1996) is shown in figure 2.7. For the whole range of *Re* confer figure A.2, page I.

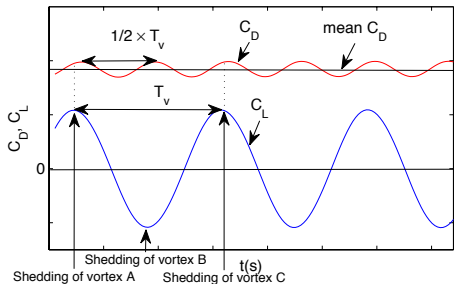

Figure 2.6: Oscillations of the dimensionless lift force, C_L and dimensionless drag force C_D, as function of time. The vortex shedding peiod is identified as T_v.

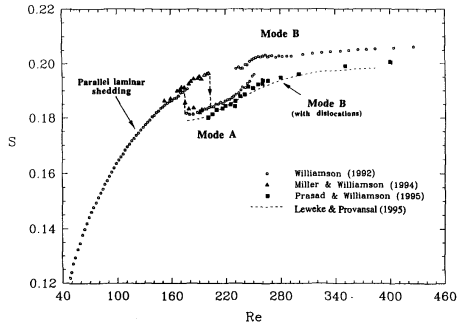

Figure 2.7: Dimensionless vortex shedding frequency, St, as function of the Reynolds number, Re. In the figure S = St. Reprinted from Williamson (1996)

2.1.5 Reynolds number

The Reynolds (*Re*) number acts as a controlling parameter for viscous flows.

$$Re = UD/\nu = \rho UD/\mu \tag{2.3}$$

The Reynolds number (named after Osborne Reynolds in 1883) gives the ratio between inertia forces and viscous forces. ρ is fluid density; ν is kinematic viscosity whereas μ is dynamic viscosity. If the flow velocity, U, is low the forces are dominated by viscous forces acting as friction forces along the body. In the opposite case when the flow velocity is high, the force necessary to overcome the inertia of water dominates the forces acting on the body.

The Reynolds number is also related to hydrodynamic stability of the flow. For low Reynolds number the flow is generally smooth and predictable (*laminar*) whereas for high Reynolds number the flow is highly disordered and unpredictable (*turbulent*).

2.2 Flow around a circular cylinder

The Reynolds number acts as a controlling parameter for viscous flow around a circular cylinder. The behaviour of the viscous boundary layer, and the vortex dynamics in the cylinder wake changes as the Reynolds number is increased. A brief overview based on Sumer and Fredsøe (1997); Williamson (1996); Zdravkovich (1997) is therefore convenient to reintroduce. Since the present study will focus on low Reynolds numbers the literature review for high *Re* is omitted.

For *Re* lower than 49 two steady recirculating vortices appear in the cylinder wake. They are symmetrically placed and their length tends to increase with increased *Re* (Williamson, 1996). As the Reynolds number is increased beyond this value the wake

becomes unsteady and vortex shedding eventually starts. The recirculation region seen for lower *Re* develops instabilities that increases in strength and amplitude for increasing *Re*. Two-dimensional laminar periodic vortex shedding is thus observed in the range $Re = 49$ to $140 - 194$ (Sumer and Fredsøe, 1997; Williamson, 1996). Vortex shedding occurs in a characteristic von-Karman vortex street downstream of the cylinder, as shown in figure 2.5, page 10.

In the 3-D wake transition regime, spanning from $Re \sim 190$ to 260, the flow is associated with two discontinuities in the St-Re graph (figure 2.7 page 11) as *Re* is increased. Described as *mode A*, the first discontinuity occurs at $Re = 180 - 194$ and is the origin of 3-D streamwise vortex loops. *Mode B* present itself at the other discontinuity, $Re \approx 230 - 250$, and involves finer-scale streamwise vortices (Williamson, 1996).

As *Re* is increased towards $Re = 1000$, the fine scale three-dimensionality becomes increasingly disordered, appearing to reduce the drag-coefficient (cf figure A.1, page I).

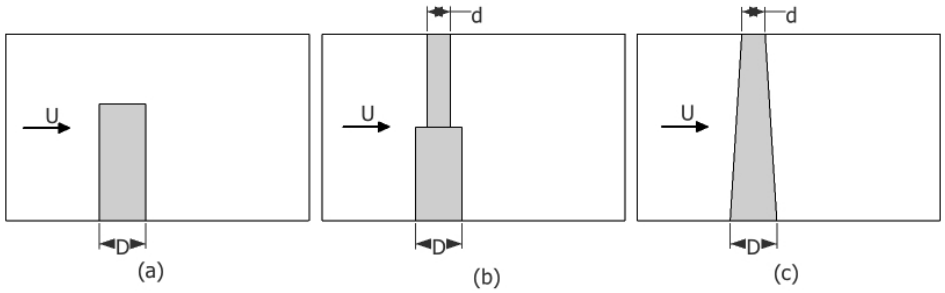

Figure 2.8: test

2.3 Flow around a tapered cylinder

Based on the local Reynolds number, *Re*, it is assumed that the flow around a tapered cylinder (figure 2.8(c), page 12) follows the same behaviour as flow around an uniform cylinder based on the local diameter. However, one-sided vortex dislocations are commonly observed in the wake of such non-uniform flows; as reported by Gaster (1969) ($Re_D \sim 50 - 200$): ”coupling between regions of different characteristic (vortex shedding) frequency introduces a certain amount of amplitude modulation to the motion.”

In Gaster (1971), vortex shedding from a slightly tapered cylinder was studied and was found to be regular and periodic within a number of spanwise cells ($Re_D \approx 80 - 120$). Between the cells, a jump in the shedding frequency was present and modulation of the motion due to this jump was identified at the beat of the vortex shedding frequency, $f_{cell1} - f_{vcell2}$, indicating vortex dislocations between the cells.

Recently, similar experimental studies have been performed by Visscher et al. (2011) on the turbulent wake behind tapered cylinders using particle image velocimetry (PIV)

($Re \sim 1.15 - 18.4 \times 10^3$). Three-dimensional flow effects such as oblique vortex shedding and vortex dislocations were identified in the wake. It was found that for larger aspect ratios, L/D, and larger Reynolds numbers, Re, the smaller vortex shedding cells along the span emerged.

Narasimhamurthy et al. (2009) performed similar analysis and found that the streamwise vorticity increased as vortex dislocation occurred for Reynolds numbers between $102 - 300$. By identifying vortex cores, helical twisting of vortex tubes was observed close to vortex dislocations. For the selected Reynolds number range, *Figure 8* in the above reference demonstrates that mode A and B (Williamson, 1996), were detected in the cylinder wake.

2.4 Flow around a finite length cylinder

In addition to tapered cylinders, flow past circular cylinders of finite length (figure 2.8(a), page 12) shows complicated three-dimensional wake structures. Park and Lee (2000) have performed experiments on finite length cylinders of different aspect ratios, $L/D = 6, 10, 13$, for a Reynolds number of 20000. Flow visualisation near the free end uncovered two streamwise, counter rotating vortices, separated from the free end of the cylinder. Downstream of the cylinder the vortices were observed to expand and shift slightly downwards in the spanwise direction due to downwash at the free end.

Sumner et al. (2004) produced similar results as Park and Lee (2000) and found that the tip vortices interacted with the regular vortex shedding from the cylinder, such that the dimensionless vortex shedding frequency, St, may vary along the cylinder span. Moreover, for low aspect ratio finite length cylinders ($L/D <\sim 3$), the tip vortices were observed to fully suppress regular vortex shedding.

Kawamura et al. (1984) found that the downwash and the trailing tip vortices, control the regular vortex shedding in the wake of the cylinder. Similarly, they found that for cylinders attached to a bottom plate, a critical aspect ratio exist for when regular vortex shedding is suppressed. The critical value varies in the literature between $L/D = 1 \sim 7$ which might be due to varying influence of the boundary layer of the endplate.

2.5 Flow around a stepped cylinder

The flow around stepped cylinders (figure 2.8(b), page 12) incorporates three-dimensional flow effects from both tapered and finite length cylinders. Three-dimensional flow effects are strongly dependent on the geometrical body shape and the viscous flow regime governed by the Reynolds number. The diameter ratio, d/D, may be the paramount factor determining the wake flow. Lewis and Gharib (1992) investigations revealed two distinct wake flows governed by the diameter ratio. A *direct* mode was observed for $d/D > 0.8$ and an *indirect* mode was observed for $d/D < 0.8$.

For the cylinders having a smaller step in the diameter ($d/D > 0.8$), a direct mode was

observed. In this mode, the vortices shed from the small and large cylinder, connected directly over the step, when they were in phase. The zone in which the vortices connected over, was of narrow character and was found to be located right behind the step (Lewis and Gharib, 1992).

Opposite to the direct mode, an indirect mode was observed for diameter ratios smaller than $d/D < 0.64$. The indirect mode observed by Lewis and Gharib (1992) was far more complicated than the direct mode. In the indirect mode, the vortices did not connect directly over the step any more, but connected through a buffer region - the modulated zone, positioned in the wake of the large cylinder. In addition to the vortex shedding frequency measured from the small and large cylinder, f_d and f_D, a shedding frequency f_N was measured in the modulated zone. Lewis reported that this frequency was always lower than f_d and f_D, and was not a sub-harmonic nor a quasi-periodic interaction of the two (Lewis and Gharib, 1992).

For uniform flow around a stepped cylinder, three-dimensional effects have been detected in a region extending up to $10D$ into the large cylinder for laminar and turbulent flows (Dunn and Tavoularis, 2006; Lewis and Gharib, 1992; Norberg, 1992; Vallés et al., 2002b; Yagita et al., 1984). Moreover, it is found that the presence of the step, to a larger extent, deteriorates regular von Karman vortex shedding in the wake behind the large diameter cylinder, D, than the small diameter cylinder d.

Yagita et al. (1984) argues that factors affecting the non-dimensional vortex shedding frequency, St, are the Reynolds number, Re, diameter ratio (d/D) and aspect ratio of the cylinders D and d (L/D and l/d). Numerous combinations of these parameters turns a complete understanding of the wake flow into a delicate problem.

2.5.1 Spanwise vortex shedding cells

Based on a spectrum analysis of velocity fluctuations three spanwise vortex shedding cells have been detected in the wake of a stepped cylinder (Dunn and Tavoularis, 2006; Lewis and Gharib, 1992; Morton and Yarusevych, 2010c; Norberg, 1992). By adapting the terminology of Dunn and Tavoularis, the L-cell and S-cell shed vortices at frequencies f_L and f_S in the wake of the large diameter cylinder, D, and the small diameter cylinder, d, respectively. In the step region a third cell, named the N-cell, was detected shedding vortices at a frequency f_N, f_N being lower than f_L and f_S. It is instructive to copy a figure produced in Dunn and Tavoularis (2006) to further illustrate the presence of these spanwise cells (cf figure 2.9 and 2.10 on page 14).

S-cell and L-cell

Away from the step, regular two-dimensional vortex shedding was detected in the cylinder wake behind cylinders D and d. The vortex shedding frequencies, f_L and f_S for the L-cell and S-cell respectively, were comparable to that of a straight circular cylinder based on the local spanwise Reynolds number (Dunn and Tavoularis, 2006; Lewis and Gharib, 1992; Morton and Yarusevych, 2010c; Norberg, 1992).

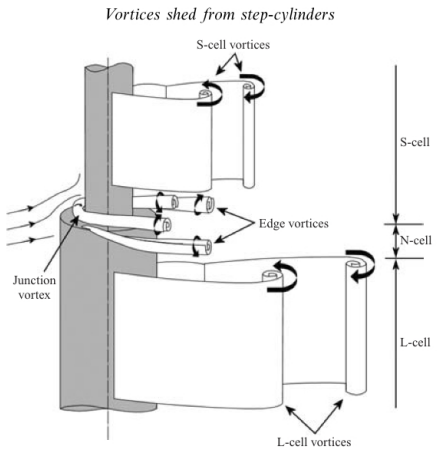

Figure 2.9: Sketch illustrating the spanwise and streamwise vortices shed from a stepped cylinder with d/D = 0.5, flow coming from left to right. Reprinted from Dunn and Tavoularis (2006)

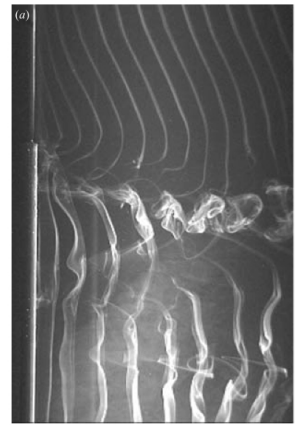

Figure 2.10: Visualisation of the wake flow behind a stepped cylinder with d/D = 0.5 at $Re_D = 150$. Flow coming from left to right. Reprinted from Dunn and Tavoularis (2006)

The flow behind the large cylinder was to a great extent affected by the step, so that regular vortex shedding was not detected until $\approx 3-4D$ into D. Due to the periodic variation in spanwise length of the N-cell, L-cell vortices were at some time-instants not detected until $\approx 10D$ into D (Norberg, 1992).

Chua et al. (1998); Dunn and Tavoularis (2006); Lewis and Gharib (1992); Morton and Yarusevych (2010c); Norberg (1992); Yagita et al. (1984) concludes that the small diameter cylinder is less affected by the step than the large diameter cylinder. Almost unaffected, regular vortex shedding takes place behind the small diameter cylinder, d, until about $1D$ away from the step. In the vicinity of the step, Norberg (1992) reports of S-cell vortices extending about $1D$ into D for diameter ratios $d/D = 0.5$ and 0.6. For a larger diameter ratio, d/D=0.8, an extension of $2D$ into D was present.

For $Re_D = 304$, Dunn and Tavoularis (2006) observed a similar extension of the S-cell $\approx 1D$ into D for a diameter ratio $d/D = 0.5$, and explains that a lower base pressure behind D may draw S-cell vortices into the wake of D were they connect with N-cell vortices (figure 2.10).

N-cell

In the junction between the cylinders d and D, a cell shedding vortices at a distinct frequency has been detected for stepped cylinders with d/D < 0.6. Contrasting the regular vortex shedding behind d and D, the observed shedding frequency around the step, f_N, was lower than both f_L and f_S (Dunn and Tavoularis, 2006; Lewis and Gharib,

1992; Morton and Yarusevych, 2010c; Norberg, 1992).

The spanwise extension of the N-cell has been found to vary in a cyclic manner (Morton and Yarusevych, 2010c). Through their experiment on a stepped cylinder, Dunn and Tavoularis (2006) similarly identifies a cyclic behaviour of the N-cell, which they in essence explains as follows; a short spanwise length was observed as the N-cell emerged, which uninterrupted grew until it instantly disappeared. After a short time the N-cell reappeared thus representing a new cycle. However, a complete disappearance of the N-cell prior to a new cycle has been a topic of some discussion in Morton and Yarusevych (2010c). Contradicting Dunn and Tavoularis (2006), Morton and Yarusevych (2010c) argues in their CFD-analysis of a stepped cylinder, that the N-cell do not disappear prior to a new cycle, but is merely reduced to such a spanwise extent difficult to reveal visually in experiments.

The N-cell was found extending up to $9D$ into D, thus affecting the large diameter cylinder wake the most (Dunn and Tavoularis, 2006; Lewis and Gharib, 1992; Morton and Yarusevych, 2010c; Norberg, 1992). Similarly to the S-cell extending $\approx 1D$ into the D, the N-cell has a similar extension of $1D$ into d (Dunn and Tavoularis, 2006; Norberg, 1992).

By means of spectral analysis Norberg (1992) ($Re = 4 - 11 \times 10^3$, d/D = 0.6) showed that a frequency modulation of f_L starts about $10D$ into D modulating f_L into f_N as the step is approached. Up to $3D$ away from the step, spectral peaks of f_N and f_L coexists, but with f_N becoming increasingly dominant closer to the step. $3D$ away from the step f_L is no longer present, the dominant vortex shedding frequency represented by f_N.

Despite a difference of factor 20 in Reynolds number, a similar behaviour of the N-cell was detected for lower ReD. For $d/D = 0.5$ and $ReD = 304$, Dunn and Tavoularis (2006) identified a small spectral peak of f_N $9.1D$ into D. Similarly to Norberg (1992), N-cell and L-cell vortices coexisted in the region from $7.6D$ to $3.5D$ confirming the periodic spanwise extension on the N-cell.

2.5.2 Streamwise vortices

In addition to the spanwise vortices, two pair of streamwise vortices were identified at the step (Dunn and Tavoularis, 2006), and are sketched in figure 2.9, page 14. The junction vortex was seen wrapping around the small cylinder base, whereas two edge vortices, on each side of the cylinder, spilled over the side of the large cylinder trailing downstream. However, shortly downstream, the streamwise vortices were entangled by the much stronger spanwise vortices and could thus not be observed further downstream in the wake.

2.5.3 Vortex inclination near the step

By studying videos of flow visualisation, Dunn and Tavoularis (2006) identified a notable inclination, with respect to the cylinder axis, of the S-cell vortices close to the step. A

similar, but not as strong, inclination was observed at the border connecting the N-cell vortices and L-cell vortices. Again, it is instructive to study figure 2.10 on page 14, copied from the excellent flow visualisation by Dunn and Tavoularis (2006), illustrating the inclination of vortices.

Dunn and Tavoularis (2006) argues that inclination of S-cell vortices occurs due to different position of flow separation along the span of d caused by the presence of the step. Below the step, S-cell vortices were inclined reversely as they connected with the N-cell due to the frequency difference between the S-cell and N-cell (Dunn and Tavoularis, 2006).

A similar deceleration of the L-cells is observed when connecting to the N-cells. Due to smaller frequency difference between the L-cell and N-cell, the inclination is not as strong as in the S-N-cell boundary.

2.5.4 Vortex dislocations

The difference in vortex shedding frequency between D and d results in vortex dislocations between vortices shed from the S-cell and N-cell and vortices shed from the N-cell and L-cell. Vortices from the N-cell connected directly with the vortices from the L-cell forming a direct connection, when the vortex shedding were in phase. As the N-cell became out of phase with the L-cell a vortex dislocation occurred, that is, an L-cell vortex forming a looped connection to a subsequent counter-rotating L-cell vortex, rather than connecting to an N-cell vortex (Dunn and Tavoularis, 2006; Morton and Yarusevych, 2010c).

Similarly, due to a discrepancy in the number of shed vortices from the S-cell and N-cell, the S-cell vortices that did not form a direct connection with N-cell vortices, formed looped connections with a subsequent counter-rotating S-cell vortex (Dunn and Tavoularis, 2006; Morton and Yarusevych, 2010c).

2.6 Flow around a dual step cylinder

The geometry of a dual step cylinder and a single step cylinder resemble each other closely (figures 2.11, page 17). However, as found, the wake depends to a great extent on the aspect ratio of the large diameter cylinder (Morton and Yarusevych, 2010b, 2011). Morton and Yarusevych (2010b, 2011) varied the aspect ratio, L/D, of the middle cylinder between 0.2-17 discovering varying wake behaviour; primarily the disappearance of the N-cells for aspect ratios below a critical value. The diameter ratio, d/D, was fixed at 0.5 and the Reynolds number, Re_D, was set to 1050.

For L/D=17 five shedding cells were observed in the wake. At the middle span of the large cylinder, the familiar L-cell appeared in addition to two N-cells at the large cylinder ends. Behind the small cylinders a single cell shedding regular vortices was distinguished, similar to the S-cell. For the current, and possibly larger aspect ratios, the

behaviour close to the steps is comparable to that of a single step cylinder (Morton and Yarusevych, 2010b, 2011).

As the large cylinder aspect ratio was reduced, the N-cell's close to the steps vanished for aspect ratios in the range 7-14, resulting in a single vortex shedding cell across the large cylinder span. As the aspect ratio was reduced from 14 to 7, St reduced in a similar manner from 0.193 to 0.175 respectively. The shedding cells behind the small cylinders persisted, hence a total of three shedding cells were identified in the wake (Morton and Yarusevych, 2010b, 2011).

Similarly, for aspect ratios between 2-7, a single vortex shedding cell across the large cylinder was identified. Large three-dimensional effects deformed the vortices shed behind the large cylinder into hairpin-like structures difficult to discern from flow visualisation. However, a dominant vortex shedding frequency was detected in the L-cell and found to be decreasing as the aspect ratio decreased (Morton and Yarusevych, 2010b, 2011).

Lastly, when the aspect ratio was reduced to L/D=1, no distinct vortex shedding frequency was recognised in the large cylinder wake, but rather broad peaks centered about $St = 0.203$ are discernable (Morton and Yarusevych, 2010b, 2011).

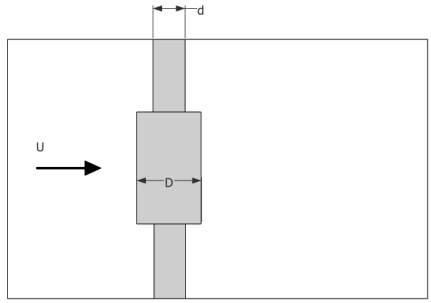

Figure 2.11: Flow around a dual step cylinder

2.7 Previous numerical studies on flow around a stepped cylinder

As opposed to the many experimental articles on the topic, only four published articles have been found concerning CFD analysis of a stepped cylinder. These articles focus mainly on recreating experimental results, but they also provide new insight into vortex dynamics. Morton and Yarusevych (2010c), performed laminar incompressible Navier-Stokes simulations on a stepped cylinder. The diameter ratio and Reynolds number ($Re_d = 150$ and $Re_D = 300$) was selected similar to what Dunn and Tavoularis (2006). The finite-volume based code, ANSYS CFX was used to solve the equations.

The same authors published in 2009 a similar article (Morton et al., 2009), analysing a

stepped cylinder with the diameter ratio of 0.5, using a URANS-based numerical solver, at a Reynolds number of 2000.

The last of the four articles is the one by Vallés et al. (2002a). It concerns a DNS simulation of a stepped cylinder with a diameter ratio 0.74 and Reynolds numbers of $Re_D = 94$ and $Re_d = 74$. The direct mode, as observed by Lewis and Gharib (1992), was for the first time reproduced numerically in this article.

The most comprehensive article, is the one by Morton and Yarusevych (2010c), and some of the results from this articles is given in the following sections. Many of their findings are similar to those by Dunn and Tavoularis (2006), so they are not repeated here. In general, the numerical articles report of good representation of the experimental findings.

Chapter 3

Numerical Method

The set of equations characterising viscous fluid flow are known as the Navier-Stokes equations. Due to a limited number of known analytical solutions, numerical solvers have been created to provide approximate solutions for fluid flow described by these equations (White, 2008).

The strategy in obtaining a solution of the flow field by approximation, usually includes the following five steps: (i) Development of a mathematical model to describe the flow (ii) Discretise the continuous flow domain into a finite number of elements (iii) Decide on an approximate version of the governing equations for each element at any given moment in time (iv) Reduce the number of unknowns by further approximation to obtain a closed system of equations (v) Assemble the system of equations, one system for each element, so that time integration is possible (vi) Solve the equations (vii) Present the results (Day, 2010).

In the present thesis the commercial code Fluent 13.0 by Ansys has been chosen as the numerical solver. Within Fluent, a laminar model has been selected. The outline of this chapter can be summarised as follows. In section 3.1, a brief overview of the mathematical equations to be solved is given, followed by establishing a numerical grid for flow around a straight cylinder in section 3.2. The choice of boundary conditions is discussed in section 3.3, along with the choice of settings in Fluent in section 3.4. A grid convergence study concerning the element distribution in the grid has been conducted in section 3.5.2 - 3.5.3. The straight cylinder grid tested in sections 3.5.2 - 3.5.3 is then used as foundation in modelling the stepped cylinder (section 3.5.4). The chapter finishes by exploring various methods of vortex identification in section 3.6.

3.1 Governing equations

The governing equations for incompressible viscous fluid flow are the continuity-equation (3.1) and the Navier-Stokes equations (3.2)-(3.4). The solution of these equations will provide the unknown velocities u, v and w representing the velocities in the x, y and z direction of a cartesian coordinate system. In addition the unknown pressure p is computed.

Knowing the velocities u, v, w and pressure p at any given point in the flow domain provides an unique opportunity of examining the fluid flow, and is thus one of the strengths using CFD.

$$\frac{\partial u}{\partial x}+\frac{\partial v}{\partial y}+\frac{\partial w}{\partial z}=0 \tag{3.1}$$

$$\frac{\partial u}{\partial t}+u\frac{\partial u}{\partial x}+v\frac{\partial u}{\partial y}+w\frac{\partial u}{\partial z}=-\frac{\partial p}{\partial x}+\nu(\frac{\partial^2 u}{\partial x^2}+\frac{\partial^2 u}{\partial y^2}+\frac{\partial^2 u}{\partial z^2}) \tag{3.2}$$

$$\frac{\partial v}{\partial t}+u\frac{\partial v}{\partial x}+v\frac{\partial v}{\partial y}+w\frac{\partial v}{\partial z}=-\frac{\partial p}{\partial y}+\nu(\frac{\partial^2 v}{\partial x^2}+\frac{\partial^2 v}{\partial y^2}+\frac{\partial^2 v}{\partial z^2}) \tag{3.3}$$

$$\frac{\partial w}{\partial t}+u\frac{\partial w}{\partial x}+v\frac{\partial w}{\partial y}+w\frac{\partial w}{\partial z}=-\frac{\partial p}{\partial w}+\nu(\frac{\partial^2 w}{\partial x^2}+\frac{\partial^2 w}{\partial y^2}+\frac{\partial^2 w}{\partial z^2}) \tag{3.4}$$

Equations (3.1) - (3.4) can be normalised using the cylinder diameter D and free stream velocity U_∞ to be expressed in the following dimensionless form:

$$\begin{gathered} u'=\frac{u}{U} \quad v'=\frac{v}{U} w'=\frac{w}{U} \quad x'=\frac{x}{D} \quad y'=\frac{y}{D} \quad z'=\frac{z}{D} \\ t'=\frac{t}{T_0} \quad p'=\frac{P}{P_0} \\ T_0=\frac{D}{U} \quad \text{and} \quad P_0=\rho U^2 \end{gathered} \tag{3.5}$$

By substituting (3.5) into the equations(3.1) - (3.4), collecting and dividing out dimensional constants, the equations can be represented on a dimensionless form as follows:

$$\frac{\partial u'}{\partial x'}+\frac{\partial v'}{\partial y'}+\frac{\partial w'}{\partial z'}=0 \tag{3.6}$$

$$\frac{\partial u'}{\partial t'}+u'\frac{\partial u'}{\partial x'}+v'\frac{\partial u'}{\partial y'}+w'\frac{\partial u'}{\partial z'}=-\frac{\partial p'}{\partial x'}+\frac{1}{Re}(\frac{\partial^2 u'}{\partial x'^2}+\frac{\partial^2 u'}{\partial y'^2}+\frac{\partial^2 u'}{\partial z'^2}) \tag{3.7}$$

$$\frac{\partial v'}{\partial t'}+u'\frac{\partial v'}{\partial x'}+v'\frac{\partial v'}{\partial y'}+w'\frac{\partial v'}{\partial z'}=-\frac{\partial p'}{\partial y'}+\frac{1}{Re}(\frac{\partial^2 v'}{\partial x'^2}+\frac{\partial^2 v'}{\partial y'^2}+\frac{\partial^2 v'}{\partial z'^2}) \tag{3.8}$$

$$\frac{\partial w'}{\partial t'}+u'\frac{\partial w'}{\partial x'}+v'\frac{\partial w'}{\partial y'}+w'\frac{\partial w'}{\partial z'}=-\frac{\partial p'}{\partial w'}+\frac{1}{Re}(\frac{\partial^2 w'}{\partial x'^2}+\frac{\partial^2 w'}{\partial y'^2}+\frac{\partial^2 w'}{\partial z'^2}) \tag{3.9}$$

3.2 Computational grid

The following section describes how the continuous flow domain is divided into a finite number of elements into a grid. The process of creating an efficient grid representing the physics correctly, is largely based on the creation- and testing of several different grids. Thus making this a time-consuming part of the CFD-analysis. However, the quality of the CFD-analysis is largely dependent on the grid quality in the sense that a too coarse grid

may give erroneous results. A large number of elements throughout the domain is preferably, but is computational expensive, so that a compromise between accuracy and number of elements is needed. An understanding of fundamental fluid dynamics of the problem is necessary so that high-density grids can be used in regions of flow where complex behaviour is expected.

3.2.1 Geometry

Figure 3.1 shows the geometry of a stepped cylinder. The small diameter cylinder, d, is joined with the large diameter cylinder, D, at the step. The aspect ratio, AR, is for D defined as AR = L/D and for d, AR = l/d.

The stepped cylinder is placed in a continuous uniform flow, U, applied upstream and flowing in the positive x-direction.

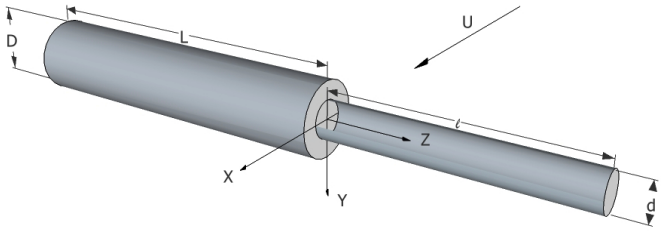

Figure 3.1: The geometry of a stepped cylinder with its principal dimensions as depicted in the figure. A uniform flow, U, is applied upstream of the cylinder and travels in the positive x-direction.

3.2.2 Grid topology

The continuous flow domain has been discretised into a finite number of elements in a structured multiblock O-H type grid in the $x-y$-plane (figure 3.2a). A similar layout has been successfully used by Krajnović (2011); Kravchenko and Moin (2000); Lei et al. (2000); Morton and Yarusevych (2010c); Nishino et al. (2008), and it is an acceptable grid topology to be used with Fluent (ANSYS, 2010, Chapter 6). The selected grid topology offers good control over the element distribution in the different grid-blocks; coarse gridding can be applied in the blocks far from the cylinder, whereas a fine grid can be applied close to the cylinder.

There are several drawbacks using a structured grid. A structured grid provides finer grid resolution in areas of less importance exemplified in figure 3.2c. High grid-density around the step is seen extending both upstream and downstream of the step, where it is not needed. Further, strange-shaped cells can appear in some regions (tall and thin, or distorted) so that inspection of the grid is of importance.

The choice of hexahedral elements permits larger aspect ratio of the elements compared with triangular elements (ANSYS, 2010). For simple geometries in which the flow conforms well to the shape of the geometry, ANSYS (2010) recommends the use of

hexahedral elements. The grid is then likely to have fewer cells than if triangular cells are used.

The grid has been designed such that a hexahedral box confines the total flow domain. An inner cylindrical block of diameter $5\sqrt{2}D$ encloses the cylinder with diameter $1D$ (figure 3.2a). The size of the domain is discussed in section 3.5.1.

The origin is placed so that the step lies in $x = y = z = 0$. The span of the cylinder is aligned along the z-axis, while the flow direction is aligned along the x-axis. To create the three-dimensional grid, the two-dimensional flow topology (figure 3.2a) has been extracted in the Z-direction. Special attention has been directed at the step-region where cylinder d and D meet, to sufficiently resolve the complex flow here (figure 3.2d). Thus, additional blocks, extending $1D$ in the spanwise direction into each of the cylinders are created to account for the intersection of the cylinders D and d.

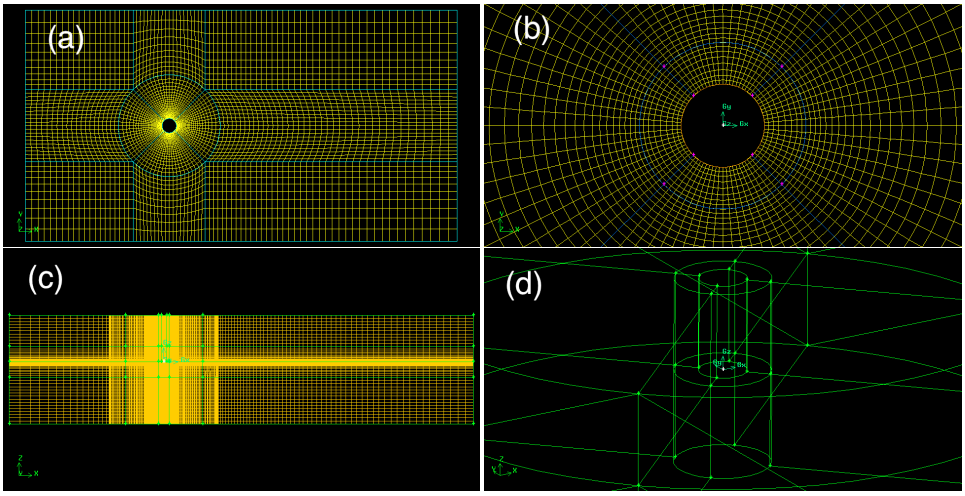

Figure 3.2: (a): Grid topology in the x-y-plane (Structured O-H block grid), (b): Grid topology in the x-y-plane for a stepped cylinder (note: every second element is plotted for better visibility), (c): Grid topology in the x-z-plane showing grid refinement around the cylinders as well in the step-region, (d): 3-D view of the block-structure around the step, the step being located at the origin. Refinement blocks extend 1D each, in the spanwise direction.

3.3 Boundary conditions

The computational grid cannot be infinite, so a set of boundaries must be positioned to enclose the grid. At the boundaries certain conditions for the velocities u, v, w, pressure p and normal gradients, $\frac{\partial u_i}{\partial x_i}$ needs to be prescribed so that a solution for the mathematical equations (section 3.1) is possible. By prescribing the value of a variable at the boundary a *Dirichlet* boundary condition is used, and when using a *Neumann* boundary condition the gradient normal to the boundary of a variable at the boundary is set. The choice of *boundary conditions* is important in the way that they should not affect the solution in a

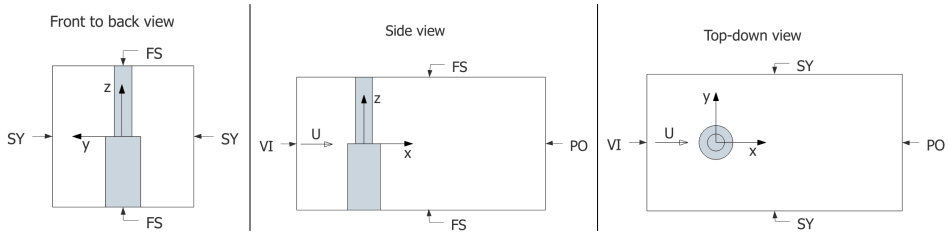

Figure 3.3: Overview of boundary conditions illustrated from different viewpoints.

non-physical way. It should also be noted that the choice of boundary conditions essentially reflects what we want to model.

For viscous flow, the relative velocities between the solid surface and fluid particle on the surface, is generally accepted to be zero. This is known as the *no-slip* boundary condition and prescribes the local fluid velocities as $u = v = w = 0$ on the surface. A *wall no-slip* boundary condition has been employed at the cylinders d and D for every simulation in the thesis. Upstream of the cylinder, a Dirichlet-type boundary condition has been employed in the form of a uniform velocity inlet (VI, figure 3.3, page 23), setting $u = 1[m/s]$ on the boundary. Downstream of the cylinder, a pressure outlet condition is assigned to the outflow boundary (PO, figure 3.3). Outlet boundary conditions are used to model flow exits where the details of the flow velocity and pressure are not known prior to solution of the flow problem. The pressure outlet condition requires the specification of static (gauge) pressure at the outlet boundary (ANSYS, 2010, Chapter 7.3.8). The pressure is defined as $p_{absolute} = p_{gauge/static} + p_{operating}$. At the boundary $p_{absolute} = p_{operating} = 101325[Pa]$ that is equal to the atmospheric pressure.

From a top-down view, the lateral walls were set to a symmetry condition (SY, figure 3.3)) assuming the flow on both sides of the wall is identical and parallel with the x-axis. A Dirichlet condition have been imposed by setting the velocity component normal to the boundary to zero as well as a Neumann condition of setting the velocity gradients at the wall to zero in all directions. The top and bottom boundaries have been assigned as free-slip walls (FS, figure 3.3), setting the shear stress equal to zero in all directions on theses surfaces. A summary of how the velocity-components, velocity-gradients and pressure are treated at the boundaries is given in table 3.1.

Table 3.1: Boundary conditions summarised

Boundary	Dirichlet condition	Neumann condition
VI (velocity inlet)	$u = 1[m/s], \quad v = w = 0[m/s]$	
PO (pressure outlet)	p = 101325 Pa	$dp/dx = dp/dy = dp/dz = 0$
SY (symmetry)	$v = 0[m/s]$	$\partial u/\partial y = \partial w/\partial y = 0$
FS (free-slip wall)	$w = 0[m/s]$	$\partial u/\partial z = \partial v/\partial z = 0$

3.4 Solver settings

A 3D, single precision, parallel version of Fluent 13.0 has been employed in the simulations. Single precision, storing data using 32 bits uses less RAM and is adequate for most cases (ANSYS, 2010). Most stepped cylinder simulations were performed on the HPC computers ”njord” and ”ve” on the NTNU network, whereas 2D and 3D straight cylinder simulations have been performed on a medium-performance desktop computer (IIMTMAL14 at NTNU). A PISO scheme has been used in the pressure-velocity coupling, recommended in ANSYS (2010). For spatial discretisation, the PRESTO! interpolation scheme have been applied for pressure whereas the momentum equations are discretised using a second order scheme (ANSYS, 2010, Chapter 28.2). For temporal discretisation, a first order implicit method based on the recommendations from (ANSYS, 2010, Chapter 28.14.1).

A sensitivity study of different discretisation schemes and pressure-velocity schemes have been outside the scope of this thesis, so that the choices made by the author has been based on ANSYS (2010), and limited previous experience. Likewise, the under-relaxation factors have been left at their default values of 1.0 for all equations, as recommended by ((ANSYS, 2010, Chapter 28.3.1.2)).

A laminar model has been chosen within Fluent due to the Reynolds number due tested ($Re = 75 - 300$) lays within the laminar range, although this might be questionable for $Re > 300$. Due to the time-varying vortex shedding the transient option is enabled. Since ANSYS Fluent is fully implicit there is no stability criterion that needs to be met in determining Δt (for instance Courant number < 1) (ANSYS, 2010, Chapter 28.14). ANSYS (2010) recommends using between 5-10 iterations per time-step and for a stable and efficient calculation . The Courant number, $U\Delta t/\Delta x$, should not exceed 20-40 in more sensitive transient regions of the domain.

The inflow velocity was set to 1 m/s and the density to 998 kg/m^3 for every simulation performed, so that the dynamic viscosity (μ) was varied in order to obtain the wanted Reynolds number. Fully developed flow was in general obtained after a dimensionless time of 200tU/D. As an attempt to advance the point of fully developed flow, a converged steady state solution was initially obtained before swithcing to the transient solver. This proved to be efficient for flow around a two-dimensional cylinder but had no effect of early trigging of vortex shedding for flow around the three-dimensional cylinders. Another attempt to trigger vortex shedding, such as patching the domain with different initial velocities, demonstrated to be of little effect in advancing regular vortex shedding.

3.4.1 Accuracy

When performing a CFD-analysis it is of importance to be aware of the accuracy of the results. Since the solver iterates to obtain the solution, a convergence criteria may be defined by the user as to when the solution has converged. The user may monitor the residuals and other integrated quantities to judge if the solution has converged and is physically correct. Fluent reports a *residual* for each of the governing equation (cf section

3.1, page 19), which is measure of how well the current solution satisfies the discrete form of each governing equation. A small residual thus yields that the solution satisfies the discrete equations well.

Additionally the user should also observe key integrated quantities, which for flow around a cylinder is represented by the mean drag-coefficient, $\overline{C_D}$, the dimensionless vortex shedding frequency, St and the root-mean-square value of the lift coefficient, $C_{L\,\mathrm{rms}}$. A solution may be judged to be converged if these quantities are within their expected values. It is thus paramount to compare the solution against similar experimental data, or similar numerical studies, in order to judge if the obtained solution is correct and physical sound.

The default globally scaled residual of 0.001 (ANSYS, 2010, Chapter 28.15), recommended by Fluent have been applied in the grid convergence study. The residual of the continuity equation and velocities u,v and w at an iteration is compared with the user-specified value (absolute convergence criteria (ANSYS, 2010, Chapter 28.15.1.7)), and if the residual is less than the user-specified value, that equation is considered to have converged at that time-step.

3.4.2 Residual analysis

For different residual values the flow around a 3D cylinder has been analysed for two different grids[1] for two different Reynolds numbers (table 3.2). For the coarse gird (B1) the Reynolds was set two 150 and for the finer grid (B4) to 300. For a constant residual value the time-step was varied to monitor the effect this had on the solution.

It should be emphasised that convergence is not guaranteed by solely monitoring the residuals - a low residual does not mean that the solution is converged. The mean drag coefficient $\overline{C_D}$, dimensionless vortex shedding frequency, St, and the root mean square of the lift coefficient, $C_{L\,\mathrm{rms}}$, have thus been used as means to judge convergence. Further, the mass flux in the domain have been measured. According to the continuity equation (section 3.1, page 19) mass should neither be created nor destroyed within the grid, so that the net flux of mass should be zero.

For a large residual of 0.01 or 0.001, as the time-step was lowered, the number of iterations per time-step decreased. It is most interesting to observe that when the solver uses only one iteration per time-step the solution become non-physical, when comparing with $\overline{C_D}, St, C_{L\,\mathrm{rms}}$, and should be avoided. For a smaller residual, say 0.0001, the time-step could be reduced similarly as above but the results remained physical. The reason for this effect is probably mainly connected to the grid-resolution and time-step and how the solution varies between two successive time-steps, but a further study in numerics of the solver would be beyond the scope of the thesis.

Unfortunately, the residual analysis was conducted as part of troubleshooting some

[1] In the x-y-plane the grids are similar whereas they have a different spanwise distribution of cells. The grids are further discussed in section 3.5.3, page 30

non-physical results obtained in the last part of the thesis. So, for the grid-convergence study a residual of 0.001 was used due to earlier execution of the convergence study. Some results presented in this chapter may thus be affected of this. For the main simulations on stepped cylinders (chapter 5.1) a residual of 0.0001 was applied.

Table 3.2: Analysis of the different combinations of time-step and residual values for flow around a straight 3-D cylinder.

Grid	Re	Residual	Δt	# Iterations	Mass flux	$\overline{C_D}$	St	C_L rms
B3	150	0.01	0.01	2-4	8×10^{-4}	1.214	0.137	0.098
B3	150	0.01	0.005	1	8×10^{-4}	1.232	0.108	0.107
B3	150	0.01	0.0025	1	4×10^{-4}	1.274	0.112	0.114
B3	150	0.0001	0.01	20	1×10^{-5}	1.263	0.190	0.061
B3	150	0.0001	0.005	14	2.3×10^{-6}	1.313	0.190	0.099
B3	150	0.0001	0.0025	10	3×10^{-6}	1.342	0.192	0.146
B3	150	0.0001	0.001	6-7	9×10^{-6}	1.360	0.185	0.18
B1	300	0.01	0.01	7	5×10^{-4}	1.231	0.187	0.315
B1	300	0.01	0.005	4	-4×10^{-4}	1.228	0.183	0.328
B1	300	0.01	0.001	1	-1.3×10^{-4}	1.269	0.142	0.333
B1	300	0.001(default)	0.001	4	-9×10^{-6}	1.280	0.190	0.301
B1	300	0.0001	0.001	10	-2.9×10^{-5}	1.338	0.206	0.460
B1	300	0.0001	0.0005	8	-4×10^{-6}	1.314	0.200	0.476
B1	300	0.00005	0.0005	12	-3×10^{-6}	1.324	0.200	0.486

3.5 Grid convergence study

The solution of numerical equations approaches their exact solution as the grid is refined. Thus, solutions on different grids, with significant different grid-resolutions should be performed to ensure that the solution is grid-independent. Accordingly, the purpose of the grid-convergence study is numerical accuracy (Spalart, 2000), solely to check how sensitive the grid is for changes in resolution.

A study considering the extents of the flow domain and element distribution in the circumferential- and spanwise direction, is given in sections 3.5.1 - 3.5.3. A grid-refinement study has also been performed in the step-region of a stepped cylinder with d/D = 0.5 (section 3.5.4).

To assess grid-convergence, the mean drag coefficient, $\overline{C_D} = \overline{F_D/0.5\rho V^2 A}$, non-dimensional vortex shedding frequency, $St = f_v D/U$ and the root-mean-square value of the lift coefficient, C_L r.m.s were compared for the different grids. Grid convergence were obtained when these values converged. A dimensionless time-step, $\Delta t U_\infty/D$, of 0.015 were used in testing the 2D-grids.

3.5.1 Domain size

It is well known that the size of the flow domain influences the numerical solution (Barkley and Henderson, 1996; Persillon and Braza, 1998). The wall blockage ratio, $D/(2Ly)$ (depicted in figure 3.4), should preferably be as low as possible to avoid locally increased velocities at the cylinder surface, due to space confinement.

The domain size used in previous CFD-analysis of flow around various circular cylinders has been found to vary (Afgan et al., 2007; Krajnović, 2011; Mittal, 2001; Nishino et al., 2008), but has been used as a starting point in the grid development.

For the same grid-resolution in the x-y-plane, the position of the inflow and lateral boundaries (Lx and Ly respectively, figure 3.4) was varied to study the effect of wall blockage and proximity to the velocity inflow boundary. The Reynolds number, *Re*, was kept constant at $Re = 150$.

While keeping the distance to the inflow boundary constant, Lx = 10D, the distance to the lateral boundary, Ly was altered between 6D - 15D. In a similar manner, the distance to the inflow boundary was altered between 5D - 15D while keeping the lateral boundaries fixed at a distance of $10D$.

For Ly<8D, the non-dimensional vortex shedding frequency, St, and the mean drag-coefficient, $\overline{C_D}$, were found to be larger when compared with experimental values, due to the blockage effect. The difference in dimensionless vortex shedding frequency, *St*, and $\overline{C_D}$ when Ly was equal to 10 and $15D$ was found to be small, hence a lateral position of $10D$ was found adequate. For flow around a circular cylinder at $Re = 100$, Behr et al. (1995) found that the lateral boundaries should be placed $8D$ from the cylinder center in order to avoid an artificially high value of *St* (*Note: in their study, the inflow boundary was fixed* $8D$ *ahead of cylinder*). The results found by in the present thesis is thus somewhat contradictory to what found by Behr et al. (1995), in that a larger lateral distance is required, for grid-convergence. The higher values of St may be explained by increased velocity past the cylinder due to the increased blockage effect, resulting in a higher local *Re*, which, for low Reynolds numbers, leads to a higher St (cf. figure 2.7, page 11).

Similarly, grid independence was obtained when the velocity inflow boundary was placed more than 10D away the cylinder center. Persillon and Braza (1998) concludes that varying the upstream distance of the inflow boundary seemed to have a greater influence on *St* than varying the lateral boundary. This is in agreement with what presently observed, though the difference being small.

Based on the results (table 3.3) the inflow boundary has been placed $10D$ **ahead of the cylinder center, the lateral boundaries** $10D$ **and the downstream boundary** $20D$ **from the cylinder center.**

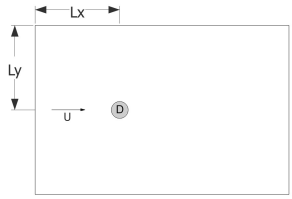

Figure 3.4: Top-down view (x-y-plane). Positions Lx and Ly represent the distance to the inflow boundary and lateral boundary respectively. The distances are both measured from the cylinder center.

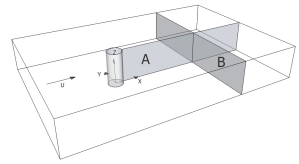

Figure 3.5: The two-dimensional circular cylinder shown extruded in the spanwise direction . The vertical transparent planes; *A* in the x-z-plane, and *B* in the y-z-plane, show the configuration of visualisation planes used in the thesis.

Table 3.3: Variation in the mean drag coefficient, $\overline{C_D}$, r.m.s of the lift coefficient, C_L r.m.s and dimensionless vortex shedding, St, by variation of the distance to the inflow and lateral boundaries. $Re = 150$

Lateral boundaries, Ly	Inflow boundary, Lx	$\overline{C_D}$	*St*	C_L rms
6*D*	10*D*	1.425	0.191	0.330
8*D*	10*D*	1.378	0.186	0.320
10D	**10D**	1.360	0.186	0.324
15*D*	10*D*	1.362	0.186	0.312
10*D*	5*D*	1.438	0.194	0.290
10D	**10D**	1.360	0.186	0.324
10*D*	12*D*	1.364	0.186	0.276
10*D*	15*D*	1.360	0.187	0.284

3.5.2 Element distribution in x-y plane

As discussed in section 3.5.1, the boundaries of the domain has been placed 10*D* upstream (Lx), 10*D* laterally (Ly) and 20*D* downstream - from the cylinder center - in the x-y-plane.

In order to decide on a proper element density in the x-y-plane, three grids with different resolutions were created. The following grid properties were varied: (i) The distance to the first element normal to the body, Δy (ii) the number of elements in the circumferential direction N_θ (iii) The number of elements in the radial direction normal to the cylinder N_r (table 3.5, page 29). A detailed figure of the element-distribution is given in the appendix figure B.1 page II.

Compared to previous studies of flow around circular cylinders (table 3.4), Δy, N_θ and N_r have been found to be in similar order of magnitude as those used in the literature. It should be noted that a variety of solvers were used in the papers referred to, so table 3.4 should merely be used as a starting point for conducting a grid-convergence study.

By using 185 elements in the circumferential direction, Kravchenko and Moin (2000) (Re=3900) obtained good results for flow around a circular cylinder, whereas Lei et al.

(2000) (Re = 80 - 1000) states that more than 128 grid points are needed to achieve a grid-independent solution. For the present grid density study 80, 160 and 200 elements were placed along the circumference for grid A1, A2 and A3 respectively.

$\overline{C_D}$, St, C_L and $C_{L\,\mathrm{rms}}$ are all quantities that are integrated based on u, v, w and p. It is thus beneficial to consider the quality of the raw-data produced by solving the Navier-Stokes equations, namely the pressure, p and velocities u, v and w. Figure 3.6, page 29 represents the velocity profile at $\theta = 90$ and 118. Grid points are placed on the curve representing the grid resolution. Adequate resolution is obtained with each grid, A1, A2 and A3. (ANSYS, 2010, Chapter 6.2.2) recommends using at least five cells in the boundary layer to adequately resolve the boundary layer. From the figure, the boundary layer in grid A2 is represented by 9 cells, and overall gives the best compromise between sufficient resolution and number of grid points.

Based on the Blasius solution for laminar flow over a flat plate at zero angle of incidence, ANSYS (2010) recommends that equation (3.10) should be obeyed in laminar flows. Grids A1, A2 and A3 all fulfill this requirement.

$$
\begin{aligned}
&y_p\sqrt{\frac{U_\infty}{\nu x}} \quad \text{where,} \\
&U_\infty = \text{free-stream velocity} \quad \nu = \mu/\rho = \text{kinematic fluid viscosity} \\
&x = \text{distance along the wall from start of boundary layer} \\
&y_p = \text{distance to the wall from the adjacent cell centroid}
\end{aligned}
\tag{3.10}
$$

The mean pressure coefficient, $\overline{C_p}$ (Figure 3.8, page 30) reveal no obvious differences between the grids, but similar to the mean friction coefficient, the discrepancy between grid A2 and A3 seem to be less than between A1 and A3.

The mean friction coefficient, $\overline{C_f} = \overline{\tau_{wall}}/0.5\rho U_\infty^2$ for grids A1, A2 and A3 are shown in figure 3.7. Based on the location of the $\overline{C_f}$-minimum, one may find the separation point. Based on curve fitting, Wu et al. (2004) showed that the mean separation angle, θ_s, was for $Re = 150$ found to be $\approx 112^\circ$. However a large scatter is reported in both experimental and numerical data due to differences in experimental and numerical setup (Wu et al., 2004). Grid A3 is ”closest” to the separation angle found by Wu et al. (2004), possibly due to an increased number of elements in the circumferential direction.

Table 3.4: Distance normal to the cylinder surface to first grid element (Δy) and number of elements used in the circumferential direction (N_θ) based on previous studies

Reference	Re	Δy	N_θ
Narasimhamurthy et al. (2009)	$100-300$	$0.01D$	
Mittal (2001)	$100, 300, 1000$	$0.001D$	
Pattenden et al. (2002)	2.9×10^5	$0.0006D$	
Nishino et al. (2008)	4×10^3	$0.0002D$	
Kravchenko and Moin (2000)	3900		163,185,291
Lei et al. (2000)	$80-1000$		64 - 160
Breuer (2000)	1.4×10^5		165, 325
Travin et al. (1999)	$5\times10^4, 1.4\times10^5$		118, 150, 210, 325

Table 3.5: Distance normal to the cylinder surface to first grid element (Δy) and number of elements used in the circumferential direction (N_θ). $Re = 150$

Grid	#elements (x-y)	Δy	N_θ	N_r	$\overline{C_D}$	St	C_L rms
A1	5200	$0.01D$	80	30	1.381	0.182	0.382
A2	17600	$0.008D$	160	60	1.370	0.186	0.345
A3	23200	$0.005D$	200	70	1.364	0.188	0.335

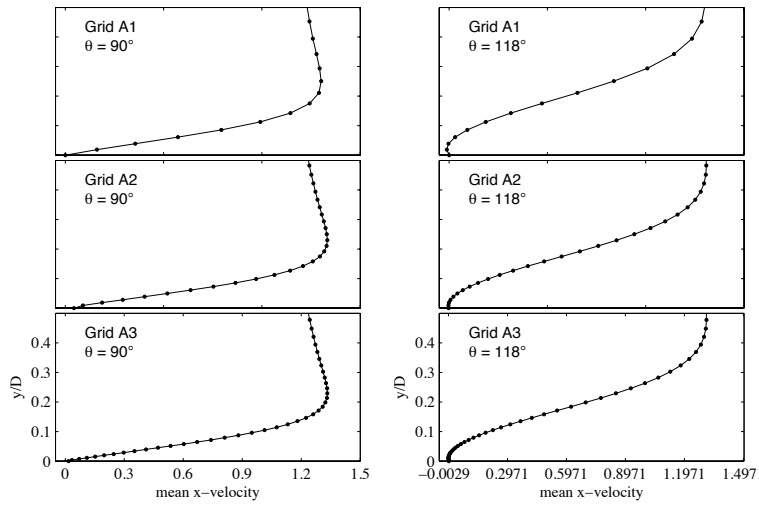

Figure 3.6: Velocity profile for grid A1, A2 and A3 (top to bottom) at a line normal to the cylinder surface at $\theta = 90°$and$118°$. The filled dots points represent grid lines.

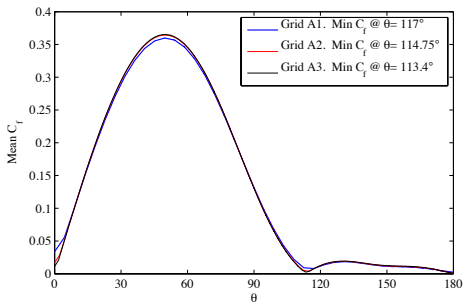

Figure 3.7: Mean friction coefficient, C_f, as function of θ. $Re = 150$

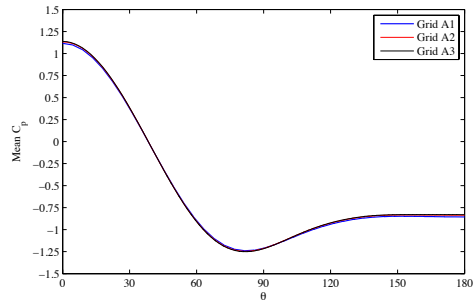

Figure 3.8: Mean pressure coefficient, C_p, as function of θ. $Re = 150$

3.5.3 Spanwise element distribution

An adequate grid-resolution is required in the spanwise direction to capture both small- and large scale three-dimensional effects for Re $>$ 194 (Williamson, 1996)). For flows with Reynolds $<$ 194, the flow is mainly two-dimensional so that a coarser grid-resolution may be used.

In the following, the three-dimensional flow around a straight cylinder is investigated by means of varying the grid-resolution in the spanwise direction (table 3.6). The spanwise resolution were kept constant along the cylinder span, and varied the space between each spanwise element varied between $\Delta z = 0.1 - 0.4$ (table 3.6). In order to capture the three-dimensional effects, the spanwise length of the cylinder was set to 4D, similarly to previous studies. Breuer (2000); Kravchenko and Moin (2000); Travin et al. (1999) successfully used a spanwise length of 2D, πD, 4.5D respectively, when conducting studies of flow around a 3D cylinder. The boundary conditions was set as discussed in section 3.3, page 22.

For $Re = 75$ small differences is seen when increasing the amount of elements in the spanwise direction, possibly due to the absence of any three-dimensional flow effects. Similarly, small differences are seen in $\overline{C_D}$ and St for grid B3 and B4 for $Re = 150$ and between B2 and B3 (table 3.6). Three-dimensional flow effects in the cylinder wake may be the cause for the discrepancy between grid B3 and B4 for $Re = 300$. To identify any three-dimensional effects plots of the crossflow velcity, v and both streamwise- and spanwise vorticity is shown in figures 3.9 - 3.16, page 32 visualised in the x-z-plane[2]. The plots show that far more flow details are captured for na increased number of elements in the spanwise direction. Figure 3.16 show small-scale streamwise vortices characteristic for *mode B* as detected by Williamson (1996). From this it may be concluded that the spanwise resolution should be $\Delta z/D = 0.1$ for $Re > 150$.

[2]Visualisation plane A is depicted in figure 3.5 on page 27

Table 3.6: Different grid resolution in the spanwise direction for flow around a 3-D straight cylinder. $\Delta z/D$ represents the spacing between grid points in the spanwise direction. $Re = 75, 150, 300$

Grid	Elements #Total	Spacing (z) $\Delta z/D$	Re	$\overline{C_D}$	St	C_L rms
B2	228800	0.3	75	1.390	0.149	0.092
B3	352000	0.2	75	1.389	0.149	0.103
B3	352000	0.2	150	1.370	0.187	0.283
B3	352000	0.2	300	1.300	0.201	0.368
B4	704000	0.1	150	1.349	0.183	0.257
B4	704000	0.1	300	1.280	0.189	0.301

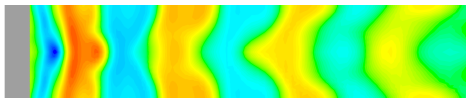

Figure 3.9: Instantaneous plot of velocity component, v, out of plane for grid B3 plotted in the x-z-plane. $Re = 300$

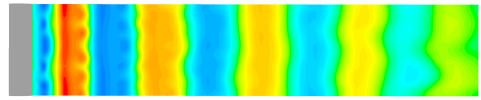

Figure 3.10: Instantaneous plot of velocity component, v, out of plane for grid B4 plotted in the x-z-plane. $Re = 300$

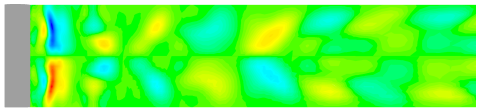

Figure 3.11: Instantaneous plot of streamwise vorticity, ω_x, plotted in the x-z-plane for grid B3. $Re = 300$

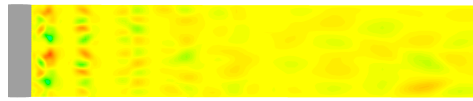

Figure 3.12: Instantaneous plot of streamwise vorticity, ω_x, plotted in the x-z-plane for grid B4. $Re = 300$

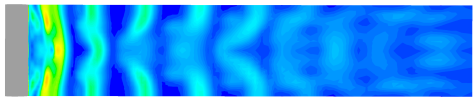

Figure 3.13: Instantaneous plot of vorticity magnitude, plotted in the x-z-plane for grid B3. $Re = 300$

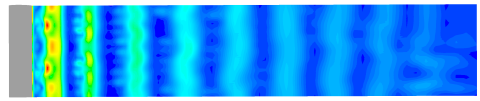

Figure 3.14: Instantaneous plot of vorticity magnitude, plotted in the x-z-plane for grid B4. $Re = 300$

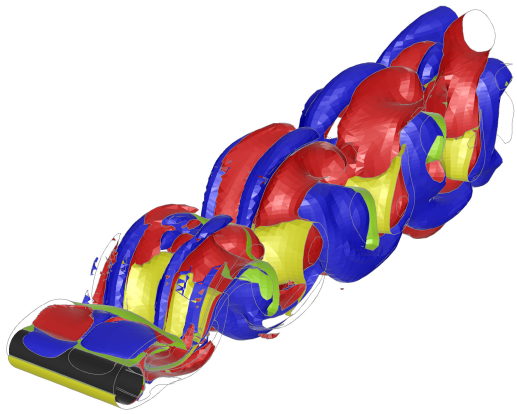

Figure 3.15: Instantaneous plot of vorticity magnitude, plotted in the x-z-plane for grid B3. $Re = 300$

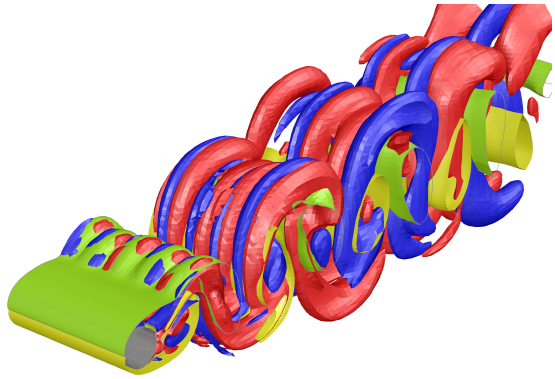

Figure 3.16: Instantaneous plot of vorticity magnitude, plotted in the x-z-plane for grid B4. $Re = 300$

3.5.4 Grid refinement around the step

Having decided on the element distribution for the flow around a straight circular cylinder it is appropriate to continue with an investigation of the sensitivity to different grid resolutions in the step region. The step region represent the zone where cylinder D attaches cylinder d. Due to the no-slip boundary condition a boundary layer will develop on D and d. Additionally, for diameter ratios $d/D < 1$, a boundary layer will be present at the step.

Refinement regions were created to fully resolve the velocity gradients in the step region, extending $1D$ into each of the cylinders D and d. Outside this refinement region, the two-dimensional grid developed in section 3.5.3 have simply been extruded to create the remaining span.

The number of cells in each $1D$ segment was varied between $10, 20$ and 40 giving a total of 20, 40 and 80 cells in the step region respectively. The mean pressure coefficient, C_p, and the mean streamwise velocity, $\overline{u}$ measured along a spanwise line parallel to the cylinder axis, have been plotted and compared in figure 3.17, page 34. Additionally the distribution of the mean pressure coefficient, C_p, along the span for differerent radial position are given in the appendix figure B.5, page VII.

Throughout, the discrepancy in C_p and $\overline{u}$ calculated for the 40 and 80 elements grid (green- and red line, respectively), is small, therefore a total number of 40 cells has been assumed to sufficiently resolve the grid, and has been employed in the further studies.

Table 3.7: Step region refinement

		#Elements		$\overline{C_D}$		St		C_L rms	
Grid	Re	Total	Step	D	d	D	d	D	d
E1	150	856000	20	1.116	1.382	0.099	0.174	0.074	0.029
E2	150	1240000	40	1.126	1.418	0.150	0.307	0.075	0.060
E3	150	2252800	80	1.130	1.420	0.153	0.308	0.078	0.059
E1	300	856000	20	1.091	1.313	0.145	0.298	0.137	0.144
E2	300	1240000	40	1.107	1.322	0.174	0.369	0.157	0.158
E3	300	2252800	80	1.100	1.323	0.172	0.371	0.141	0.155

3.5.5 Time-step analysis

In table 3.8 an analysis of different time-steps have been performed (table 3.8). The C_L rms has shown to be the quantity most affected by a change in time-step. **Based on the small difference between a time-step of tU/D = 0.01 and 0.005, a time-step of tU/D = 0.01 has been selected for the further studies.**

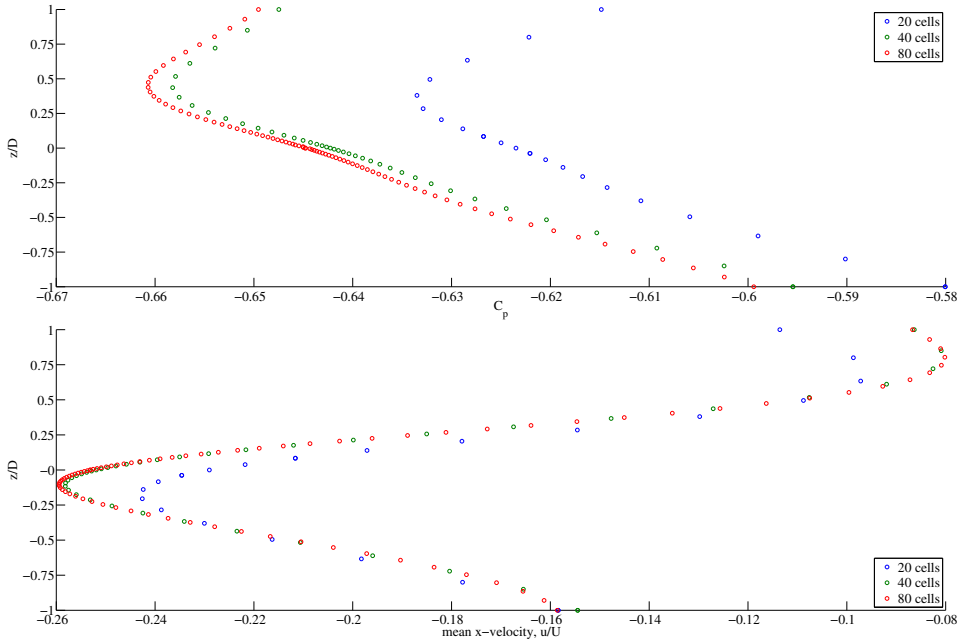

Figure 3.17: Grid refinement study in the step region. The mean pressure coefficient, C_p, and mean streamwise velocity $\overline{u}$ measured along a spanwise line in the wake has been compared for different step resolutions.

Table 3.8: Step region refinement

			$\overline{C_D}$		St		C_L rms	
Grid	Re	Time-step tU/D	D	d	D	d	D	d
E2	150	0.03	1.114	1.403	0.148	0.303	0.070	0.052
E2	150	0.015	1.126	1.418	0.151	0.309	0.087	0.069
E2	150	0.01	1.130	1.423	0.150	0.310	0.093	0.075
E2	150	0.005	1.134	1.429	0.150	0.311	0.103	0.086

3.6 Vortex identification

Due to flow separation, coherent vortex structures will be formed in the wake of a cylinder. For a stepped cylinder it is most interesting to study how the vortices shed from D and d connect over the step and also between the shedding cells along the stepped cylinder span.

Although the concept of a vortex is known to fluid dynamicists, a precise definition of the flow features of a vortex is still being researched (Rütten et al., 2008). Thus, a vast variety of methods have been created in order to detect and visualise vortices, some better than

others (Jeong and Hussain, 1995).

Characterised as conventional methods, plots of vorticity and pressure, and massless particles dropped into the fluid, can be used to detect vortices. Two-dimensional plots of vorticity and pressure show the contours of the vortices whereas isosurfaces show three-dimensional vortex structures (cf figures 3.12 and 3.16, page 32).

More sophisticated vortex identification methods consists of the *Q-criterion* (Hunt et al., 1988), and λ_2 (Jeong and Hussain, 1995) which have been developed in order to visualise vortex cores. The selection of the methods to display vortex structures is case dependent. (ANSYS, 2010).

3.6.1 Vorticity

A physical characterisation of a vortex may be given in terms of water particles rotating in the same manner around a vortex core. A vortex axis is defined in the center of the vortex core in which the vortex rotates about. Within the vortex core the circumferential velocity is at is highest and decreases at the outer part of the vortex. Hence, a low pressure region is distinct at the vortex core. Due to viscosity and shear, the water particles close to the vortex core is angularly deformed. Such deformations are derived in classical fluid mechanics (White, 2008) by differential analysis, in which the *vorticity* vector can be derived as one-half of the velocity vector, or twice the angular velocity of a fluid element. Thus, vorticity plots in the wake of a cylinder may indicate the existence of vortices.

Using the present coordinate system ω_z and ω_x represent spanwise vorticity and streamwise vorticity respectively, whereas ω_y represents vorticity in the x-z-plane. Definition of positive direction is given in figure 3.18, page 35.

$$\omega_x = \left(\frac{\partial w}{\partial y} - \frac{\partial v}{\partial z}\right) \quad (3.11)$$

$$\omega_y = \left(\frac{\partial u}{\partial z} - \frac{\partial w}{\partial x}\right) \quad (3.12)$$

$$\omega_z = \left(\frac{\partial v}{\partial x} - \frac{\partial u}{\partial y}\right) \quad (3.13)$$

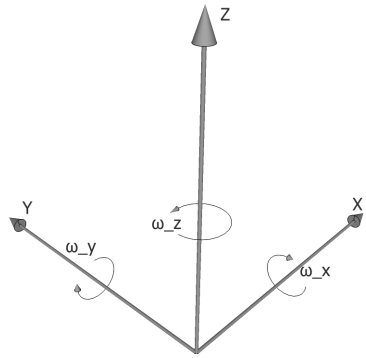

Figure 3.18: Indication of positive vorticity of a fluid element.

3.6.2 Q-criterion and λ_2 criterion

Common to both the Q-criterion and λ_2 is that they have been developed based on decomposition of the velocity gradient tensor into a rate of rotation (Ω_{ij}) and rate of strain (S_{ij}).

$$\nabla u = \frac{\partial u_i}{\partial x_j} = \frac{1}{2}(\frac{\partial u_j}{\partial x_i} + \frac{\partial u_i}{\partial x_j}) + \frac{1}{2}(\frac{\partial u_i}{\partial x_j} - \frac{\partial u_j}{\partial x_i}) \tag{3.14}$$

$$\text{where } \Omega_{ij} = \frac{1}{2}(\frac{\partial u_i}{\partial x_j} - \frac{\partial u_j}{\partial x_i}) \tag{3.15}$$

$$\text{and } S_{ij} = \frac{1}{2}(\frac{\partial u_j}{\partial x_i} + \frac{\partial u_i}{\partial x_j}) \tag{3.16}$$

Based on an eigenvalue analysis of the velocity gradient tensor, ∇u, vortical motion can be detected (Chong et al., 1990). The Q-criterion (Hunt et al., 1988), is based on the second invariant, Q, of ∇u being positive:

$$Q = \frac{1}{2}(\Omega_{ij}\Omega_{ij} - S_{ij}S_{ij}) \tag{3.17}$$

A positive Q thus implies that a point in the fluid is dominated by rotation, $\Omega > S$. Iso-surfaces of positive Q isolate areas where the strength of rotation overcomes the strain, hence showing vortex structures.

One of the disadvantages of the Q-criterion is its exclusive characteristics, that is, the threshold value of Q needs to be set. A lower, but positive Q-value tends to include more coherent structures (figure 3.22, page 37) than a larger value (figure 3.20, page 37).

Another disadvantage of the Q-criterion is that it may display non-vortex structures, for instance shear layers close to the cylinder surface, due to high vorticity in these parts of the flow. An example of this is shown in figure 3.22 where isosurfaces of Q have been plotted in the flow around a straight cylinder at $Re = 300$, identifying streamwise and spanwise vortices in the wake.

Vortex identification may be case dependent, so a comparison between the Q-criterion and λ_2-criterion have been performed, in figure 3.21 and 3.22, page 37. Despite λ_2 being favoured as a vortex identification method (Jeong and Hussain, 1995), the differences between the two methods have been found negligible.

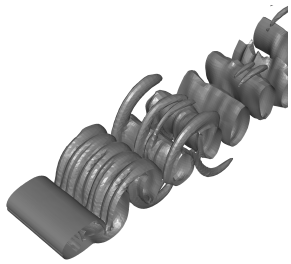

Figure 3.19: Iso-surface of vorticity magnitude. Grid B4 $Re = 300$

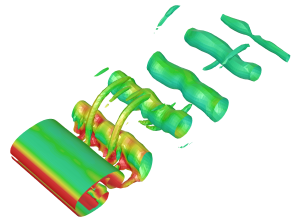

Figure 3.20: Iso-surface of Q=29 coloured by vorticity magnitude. Grid B4 $Re = 300$

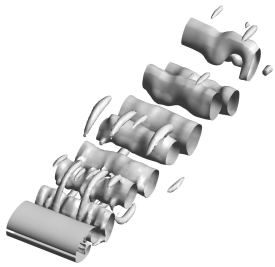

Figure 3.21: Iso-surface of λ_2. Grid B4 $Re = 300$

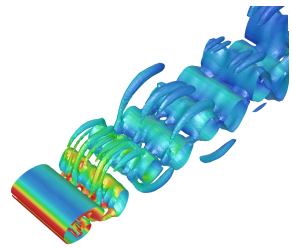

Figure 3.22: Iso-surface of Q=0.038 coloured by vorticity magnitude. Grid B4 $Re = 300$

Chapter 4

Verification of numerical model

4.1 Verification of model

In order to gain further confidence in the numerical model, the flow around a stepped cylinder with d/D = 0.5 at Re_D = 150 have been compared against similar studies. Whereas Dunn and Tavoularis (2006) have performed experiments on a stepped cylinder, Morton and Yarusevych (2010c) conducted numerical studies on a stepped cylinder with diameter ratio d/D = 0.5 at a similar Reynolds number, Re_D = 150.

By means of plotting the Q-criterion in the wake it is possible to discern spanwise vortex shedding. Figure 4.1 shows isosurfaces of the Q-criterion (discussed in section 3.6, page 33) plotted on contours of the crossflow velocity v, in the x-z-plane. Regular vortex shedding is observed taking place behind the small cylinder (d) at $z/D > 1$, and behind the large cylinder (D) at $z/D < -10$. In the region $-5 > z/D > -10$ an inclination of the spanwise vortices shed behind D is observed, as they are decelerated in order to connect to the vortices shed in the region $-0.5 > z/D > -4$. An inclination of the vortices shed behind the small cylinder, away from the cylinder axis, is observed taking place at z/D = 2 followed by a reverse inclination occurring z/D = 0.25, when the vortices connected over the step to the adjacent vortex shedding cell. This adjacent vortex shedding cell, occurring in the step-region, can be identified as the N-cell, whereas the S-cell and L-cell represents vortex shedding cells behind the small and large cylinder respectively. The three shedding cells identified are similar to what observed by Dunn and Tavoularis (2006); Lewis and Gharib (1992); Morton and Yarusevych (2010a,b, 2011); Norberg (1992) for stepped cylinders.

Figure 4.1 may be compared with the experimental results obtained by Dunn and Tavoularis (2006), in figure 4.2, for a similar Reynolds number, $Re_D = 150$, and diameter ratio, d/D = 0.5. Good agreement is observed between the numerical- and the experimental results.

The presence of the step, located in the junction between cylinder d and D, is the reason to why complex three-dimensional flow effects exist in the wake of a stepped cylinder. Close to the step the flow is observed to separate as the flow passes the step, and two streamwise vortices have been reported to exist (Dunn and Tavoularis, 2006; Morton et al., 2009). Figures 4.5 - 4.10, page 42 have been devoted to visualise particular flow phenomena detected at the step.

An attempt to visualise the two streamwise vortices through the use of pathlines are

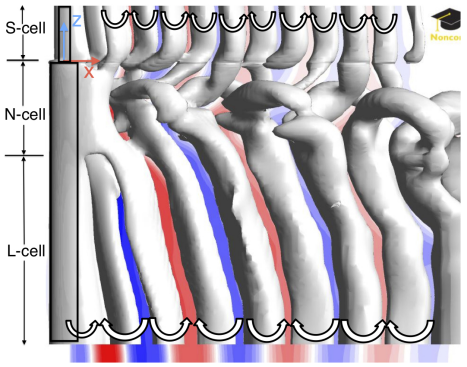

Figure 4.1: Isosurfaces of the Q-criterion plotted on contours of the crossflow velocity, v. Q = , depicts shed vortices in the wake of a stepped cylinder with d/D = 0.5 at $Re_D = 150$

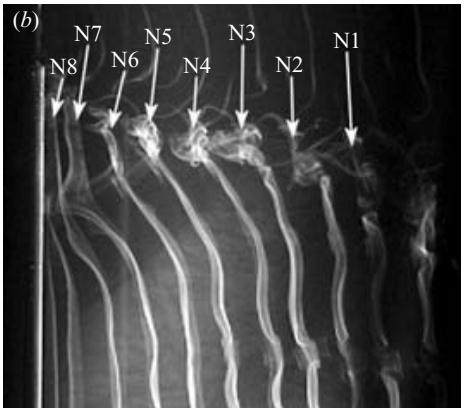

Figure 4.2: Vortices behind a stepped cylinder of d/D = 0.5, close to the step, visualised in the experiments by Dunn and Tavoularis (2006) for $Re_D =$ 152. Reprinted from Dunn and Tavoularis (2006)

shown in figures 4.7 and 4.8 for the junction- and edge-vortex respectively. These plots is in good agreement with what observed in the experiments by Dunn and Tavoularis (2006) (figure 4.9). Similarly to what Dunn and Tavoularis (2006) experienced, both the streamwise vortices disappeared shortly downstream, as they were entangled with the spanwise S-cell vortices. Figure 4.10 shows pathlines of the junction- and edge-vortices together as well as a contour-plot of streamwise vorticity, ω_x in the y-z-plane. As they travel downstream this figure indicate that the two streamwise vortices rotate in the same manner. Further downstream, both streamwise vortices are seen entangled by the spanwise vortices and deflected in the spanwise direction.

Furthermore, the mean pressure coefficient distribution have been plotted at different radial positions along the span to make a comparison to the study of Morton et al. (2009). Figure 4.3 shows the pressure coefficient from the flow around a stepped cylinder with d/D = 0.5 at $Re_D = 150$. Although a Reynolds number of Re_D = 2000 was used by Morton et al. (2009) a similar trend close to the step is observed.

The vortex shedding frequency distribution along the span of the stepped cylinder have been measured and compared against results from figure 6 and 7 in Morton and Yarusevych (2010c). For a stepped cylinder with d/D = 0.5 at Re_D = 150 the dimensionless vortex shedding frequency, St (figure 4.4), is in good agreement with that obtained by both Morton and Yarusevych (2010c) and Dunn and Tavoularis (2006).

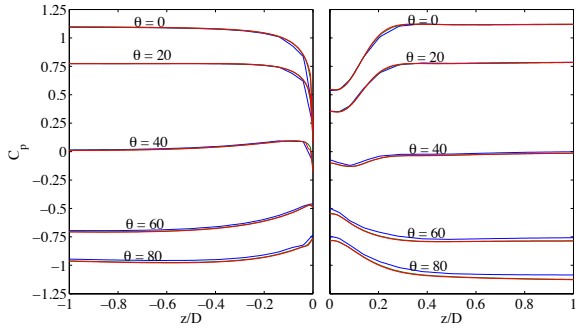

(a) Results obtained from the numerical model. d/D = 0.5 and Re_D = 150.

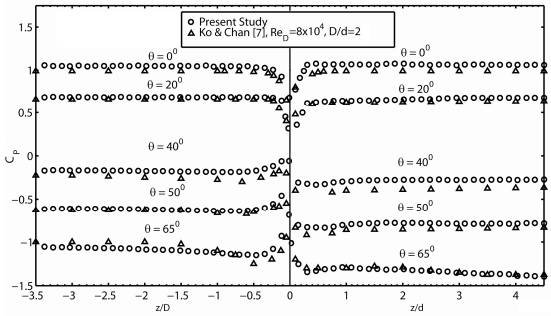

(b) Results from Morton et al. (2009). d/D = 0.5 and Re_D = 2000. Reprinted from Morton et al. (2009)

Figure 4.3: Spanwise variation of the mean pressure coefficient for different radial positions. $\theta = 0$ represents the forward stagnation point.

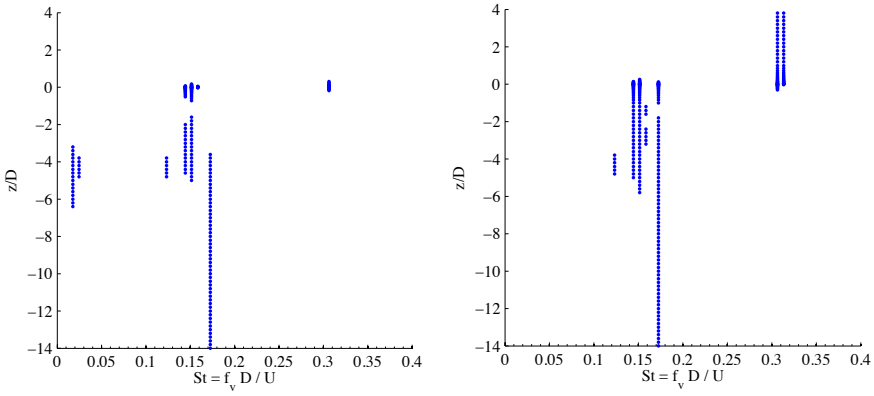

(a) Dimensionless vortex shedding frequency, St, based on a frequency analysis of the streamwise velocity u.

(b) Dimensionless vortex shedding frequency, St, based on a frequency analysis of the crossflow velocity v.

Figure 4.4: Variation of the dimensionless vortex shedding frequency, St, along the span of a stepped cylinder with d/D = 0.5 at Re_D = 150. The streamwise- and crossflow velocities have been measured at a line perpendicular to the cylinder axis, positioned in the wake at x/D = 1.8, y/D = -0.15

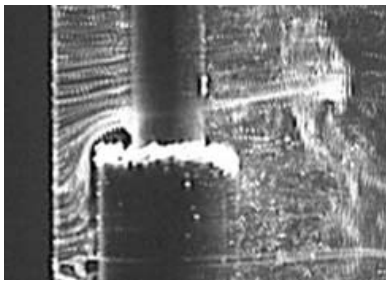

Figure 4.5: The resirculating bubble detected in experiments by Dunn and Tavoularis (2006). $Re_D = 1230$

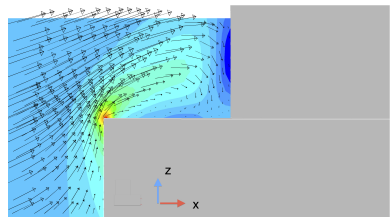

Figure 4.6: Velocity vectors plotted onto contours of instantaneous y-vorticity in the X-Z-plane at the leading edge of step. $Re_D = 150$

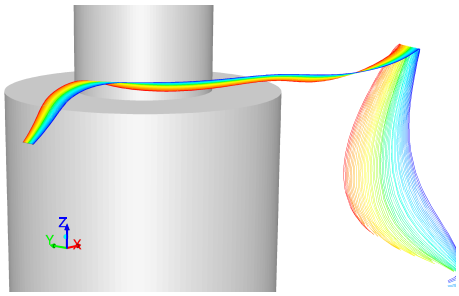

Figure 4.7: Pathlines showing the junction vortex formed at the leading edge of step, extending downstream. $Re_D = 150$.

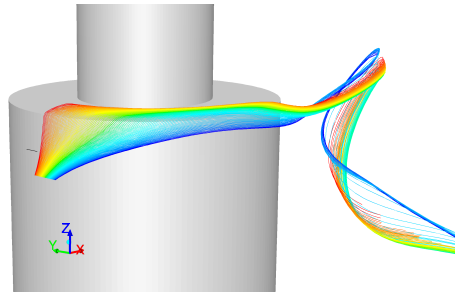

Figure 4.8: Pathlines showing tip vortices at the trailing edge of the step rotating in a counter-clockwise manner when seen from downstream. The pathlines are coloured by pathline-identity.

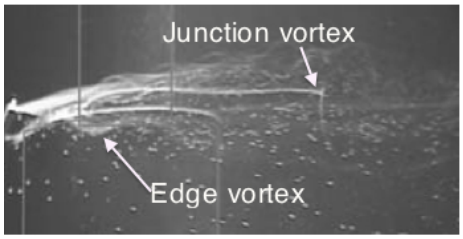

Figure 4.9: The "junction-vortex" as observed in experiments by Dunn and Tavoularis (2006) $Re_D = 1100$. The vortex is detected above the step, extending downstream until abrupt bended towards the cylinder span. Reprinted from Dunn and Tavoularis (2006).

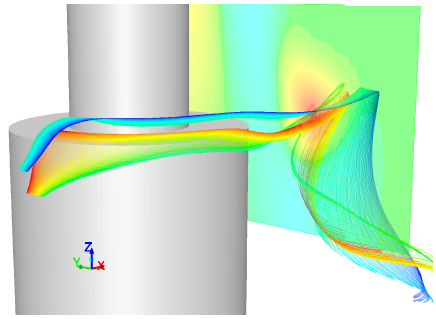

Figure 4.10: Pathlines showing the junction- and edge-vortices together. In the back, contour plots of streamwise vorticity, ω_x, is shown, positive vorticity marked red.

Chapter 5

Results and discussion

5.1 Flow around stepped cylinders with d/D = 0.3, 0.5, 0.8 and 0.9

Based on the convergence study performed in the previous chapter the distribution of elements was decided on. The grid A2 was decided for the x-y-plane whereas a difference spanwise resolution $\Delta z/D$, based on Reynolds number was suggested. The time-step for the simulations was set to tU/D = 0.01. In table 5.1 details about the grids are given, along with the geometry of the different cylinders.

Table 5.1: Grid used in simulations for the different Reynolds numbers.

d/D	Re_D (Re_d)	$\Delta z/D$	#Elements	L	l	D	d
0.3	150 (50)	0.2	2.4×10^6	14D	4D	1D	0.3D
0.5	150 (75)	0.2	2.3×10^6	14D	4D	1D	0.5D
0.8	150 (120)	0.2	2.2×10^6	14D	4D	1D	0.8D
0.9	150 (135)	0.2	2.2×10^6	14D	4D	1D	0.9D
0.3	300 (100)	0.1	3.8×10^6	14D	4D	1D	0.3D
0.5	300 (150)	0.1	3.7×10^6	14D	4D	1D	0.5D
0.8	300 (240)	0.1	3.5×10^6	14D	4D	1D	0.8D
0.9	300 (270)	0.1	3.5×10^6	14D	4D	1D	0.9D
0.3	600 (200)	0.1	3.8×10^6	14D	4D	1D	0.3D
0.8	600 (480)	0.1	3.5×10^6	14D	4D	1D	0.8D

5.1.1 Instantaneous wake flow

Figure 5.1 shows instantaneous plots of the crossflow velocity, v/U, and spanwise velocity, w/U, for flow around a stepped cylinder with diameter ratio d/D = 0.3, 0.5, 0.8 and 0.9 at $Re_D = 150$. The velocities have been plotted in the x-z-plane[1], the flow coming from left to right.

From the instantaneous plot of crossflow velocity, v/U, it is possible to discern spanwise vortex shedding. Positive v is defined into the paper-plane, so that one spanwise "tube" of positive- and one of negative velocity represents a vortex. The vortex rotates about the

[1] cf figure 3.5, page 27 describing the visualisation planes

spanwise ”tube” of zero crossflow velocity located between positive and negative *v*. To further elucidate this, rotating vortex structures depicted by means of the Q-criterion have been plotted on contours of the crossflow velocity *v* in figure **??** on page **??**.

For all cylinders except for d/D = 0.3, regular vortex shedding occurs in the wake of both the large and small diameter cylinder. The Reynolds number may be to small (Re_d = 50) for regular vortex shedding to occur (cf section 2.2, page 11). However, the difference in step size have a distinct effect on wake flow. For d/D = 0.8, 0.9 vortices from the L-cell and S-cell connect directly over step, the connection taking place slightly above the step. This behaviour is comparable to what observed by Lewis and Gharib (1992) as the *direct mode*. For d/D = 0.5, vortices behind the small and large diameter connect right below the step, and the connection is shifted in the negative z-direction further downstream.

When considering the spanwise velocity, *w*, distinct differences are observed between the different diameter ratios. For small d/D, a maximum is observed at the leading edge at x/D = -0.5 and z/D = 0, clearly indicating an upwards flow over the step. The upward flow over the step decreases significantly in magnitude as d/D is increased. The contours of positive and negative *w* in the wake of the cylinders are observed at positions where the spanwise vortices are inclined in the streamwise direction.

5.1.2 Velocity distribution in the laminar wake

It is difficult to determine a downwash effect from the instantaneous wake-plots in figure 5.1. The mean streamwise- and spanwise velocity are thus measured along a spanwise line perpendicular to the cylinder axis, placed downstream at x/D = 3 and shown in figure 5.2. For d/D = 0.8 and 0.9 the variations in the mean streamwise- and spanwise velocity along the span is less than for d/D = 0.3 and 0.5. Figure 5.2b indicate that the downwash is significant, and stronger, for the cylinders with smaller d/D. For larger d/D the mean z-velocity is close to zero. The positive spanwise velocity observed at z/D $\geq$ 0 may be related to when vortices connect over the step, due to streamwise twisting of the spanwise vortices as they are connected over the step. Interestingly, for the largest diameter ratio positive spanwise velocity is observed as far as 3D away from the step. One may identify vortex connections at a similar position in figure 5.1 indicating that the vortex connections, as d/D is increased, move in the positive spanwise direction.

Similarly, the variation in the mean streamwise velocity profile is less for the stepped cylinders with a larger d/D. It is observed that the streamwise velocity is decelerated as the step is approached. The deceleration is discerned to be larger for smaller d/D when comparing d/D = 0.5 and 0.8.

The difference in streamwise- and spanwise velocity between the different stepped cylinders is small for spanwise positions z/D $<$ -8. This might indicate that the effect of the step extends about 8D to 9D into the large diameter cylinder. Similar observation has been done by Dunn and Tavoularis (2006); Norberg (1992).

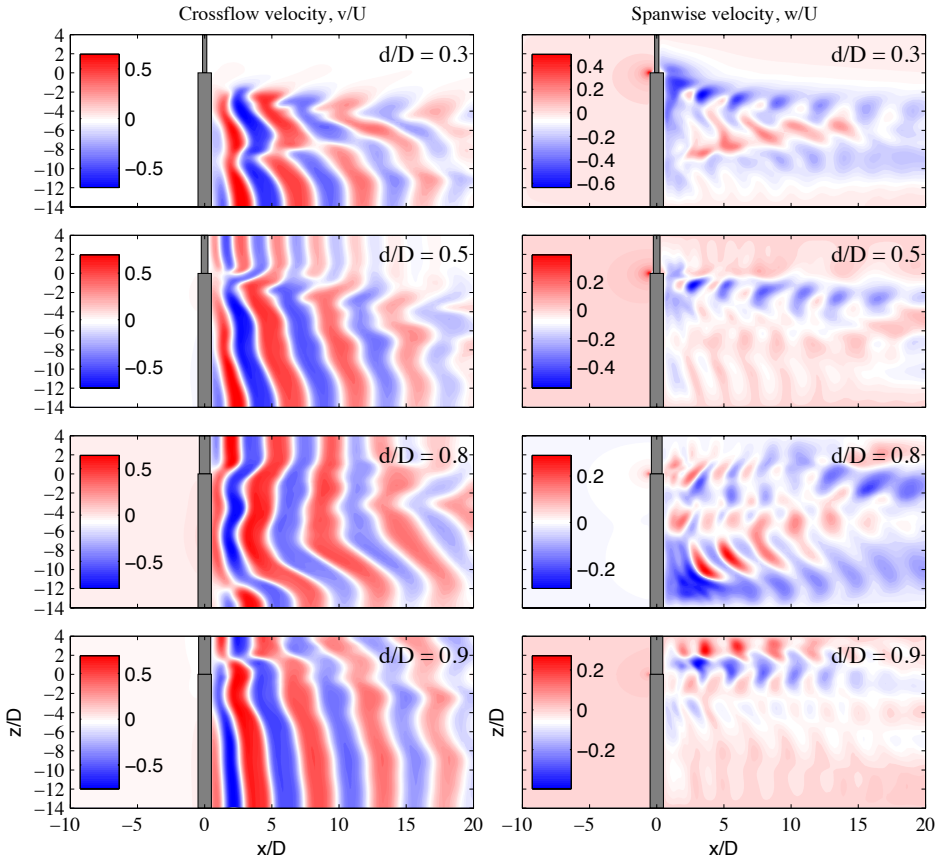

Figure 5.1: Instantaneous plots of crossflow velocity, v, and spanwise velocity, w, in the wake of stepped cylinders with d/D = 0.3, 0.5, 0.8 and 0.9. $Re_D = 150$

5.1.3 *Flow in the step region*

Figure 5.4 show mean pathlines in the wake of the stepped cylinders in the y-z-plane (visualisation plane B in figure 3.5, page 27) at a downstream position of 0.6D and 1D. The streamwise vortices, as found by Dunn and Tavoularis (2006) and Morton et al. (2009) have readily been located in the wake for flow around the cylinders with d/D = 0.3 and 0.5. For the larger diameter ratios, in particular d/D = 0.9, they have been difficult to identify.

The junction vortex (figure 4.9, page 42) may be identified in figures 5.4(a) and 5.4(b) at z/D = 0.5 and 0.75 on the small cylinder at a downstream distance of x/D = 0.6. Further downstream the junction vortex disappears for d/D = 0.3 but remains visible at z/D = 0.25 for for d/D = 0.5. The junction vortex has not been detected for d/D = 0.8 and 0.9 (figures 5.4(c) and 5.4(d)). Dunn and Tavoularis (2006) reports from their experiments that the

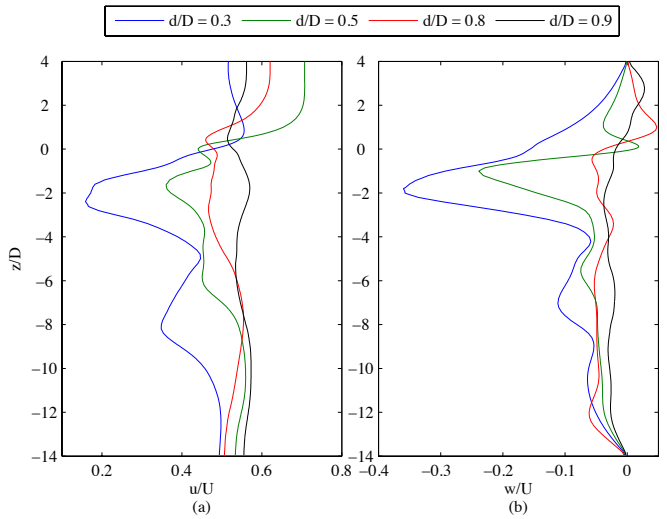

Figure 5.2: (a) Mean streamwise velocity (b) Mean spanwise velocity. Measured along a spanwise line parallel to the cylinder axis positioned at y/D = 0 and x/D = 3. $Re_D = 150$

recirculating fluid at the step is the main reason to why the junction vortex exist. Originating from the recirculating fluid, two branches of the junction vortex was observed to wrap around the small cylinder base as the fluid was conveyed downstream the step forming the junction vortex. Hence, a possible reason for the absence of the junction vortex for d/D = 0.8 and 0.9 may be tracked to the recirculating fluid at the leading edge. The upflow at the step have thus been investigated and illustrated in figure 5.3 by vectors of the mean velocity in the x-z-plane. For the smaller d/D the upflow and separation of fluid over the leading edge is obvious and a region of recirculating fluid is present at the step. For d/D = 0.9 (figure 5.3(d))) the recirculating bubble is not detected whereas it starts forming for d/D = 0.8 in figure 5.3(c).

Edge vortices have been detected for all cylinders being located in the step region on each side of the large cylinder, D. For d/D = 0.3 it is seen developing at z/D = -0.4 for a downstream position of x/D = 0.6 (figure 5.4(a)). Further downstream it is seen convecting in the negative spanwise direction, probably due to downwash (figure 5.4(e)). A similar behaviour is observed for d/D = 0.5 with the edge vortices developing at z/D = 0 (figure 5.4(b)), their position shifting in the negative spanwise direction as they travel downstream (figure 5.4(f)).

Although not as strong, edge vortices have been detected for d/D = 0.8 and 0.9 at approximately z/D = -0.5 at a downstream distance x/D = 0.6D (figures 5.4(c) and 5.4(d)). Contrary to d/D = 0.3 and 0.5 the edge vortices are shifted in the *positive* spanwise direction for d/D = 0.8 and 0.9. This finding has not been pursued in more detail but may be due to positive spanwise velocity in the wake as observed in figure 5.2b.

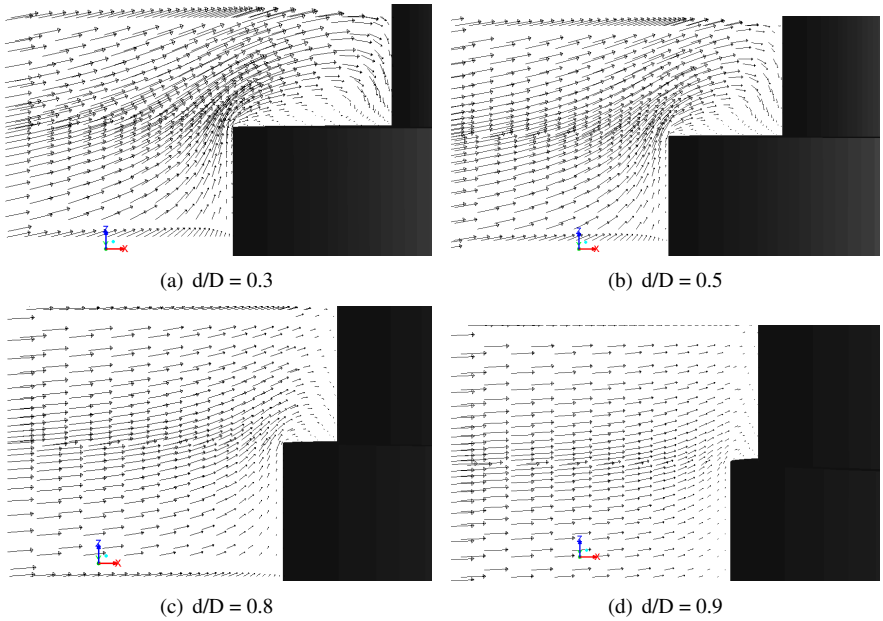

(a) d/D = 0.3 (b) d/D = 0.5

(c) d/D = 0.8 (d) d/D = 0.9

Figure 5.3: Upflow over the leading edge of the step for a stepped cylinder with d/D = 0.3, 0.5, 0.8 and 0.9. $Re_D = 150$

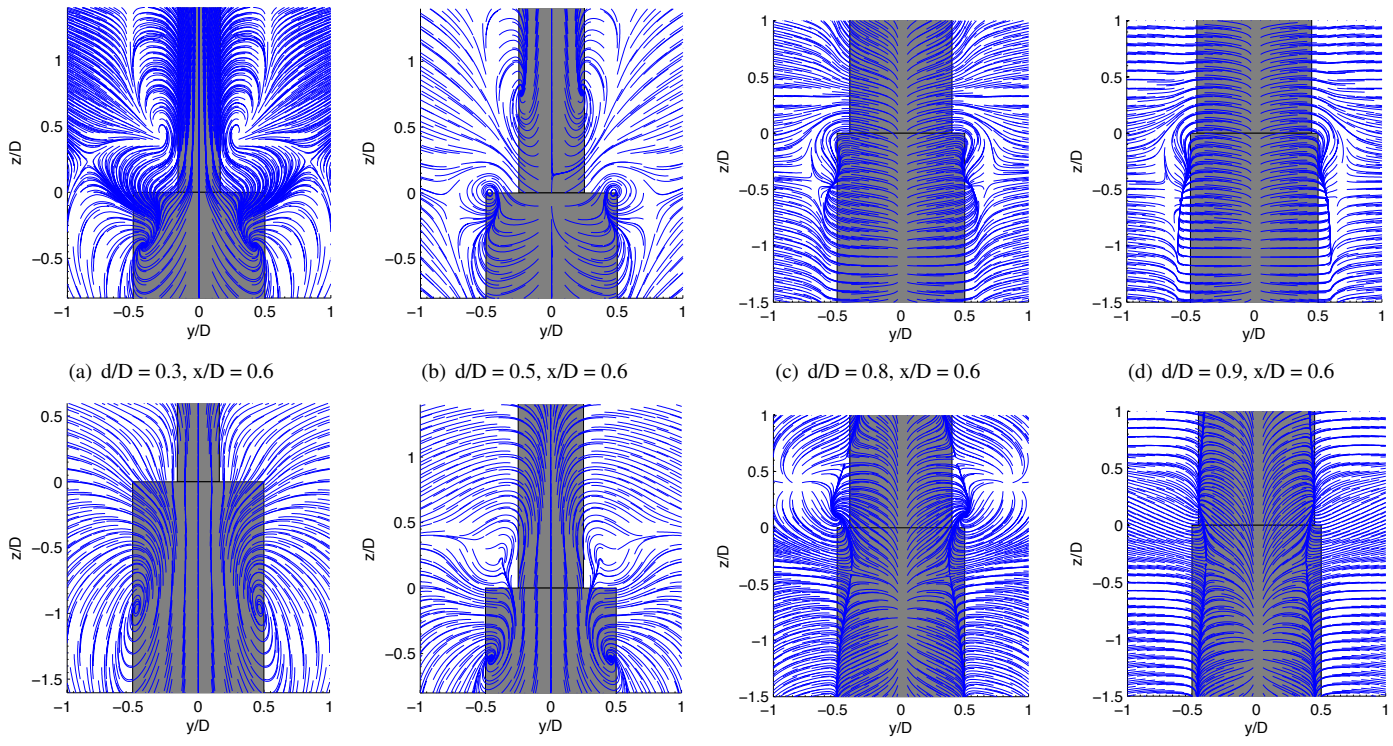

(a) d/D = 0.3, x/D = 0.6 (b) d/D = 0.5, x/D = 0.6 (c) d/D = 0.8, x/D = 0.6 (d) d/D = 0.9, x/D = 0.6

(e) d/D = 0.3, x/D = 1 (f) d/D = 0.5, x/D = 1 (g) d/D = 0.8, x/D = 1 (h) d/D = 0.3, x/D = 1

Figure 5.4: Pathlines in the y-z-plane in the wake of a stepped cylinder with d/D = 0.3, 0.5, 0.8 and 0.9 at downstream positions of x/D = 0.6 and 1. Re_D = 150.

5.1.4 Surface pressure distribution

Figure 5.5 shows contour plots of the mean pressure coefficient, C_p, on the cylinder surface for stepped cylinder with a diameter ratio d/D = 0.3, 0.5, 0.8 and 0.9. The pressure contour plots show the variation of the mean pressure coefficient along the circumference along the cylinder span. Nearly constant pressure contours along the span is observed for d/D = 0.9 being similar to that of a straight cylinder. As d/D is decreased the pressure contours for $\theta > 90$ in the region 0 > z/D > -5 behaves in a wavy fashion as the point of pressure recovery is shifted forward. The tendency is more distinct for d/D = 0.3 than the others.

For the small cylinders, the pressure contours for d/D = 0.3 and 0.5 behave in a similar manner. For the larger diameter ratio, d/D, the pressure contour lines continues in a straight manner across the step, whereas for lower d/D large variations in C_p are visible close to the step.

Within 2D of the step on the large diameter cylinder there is a depression in C_p for d/D = 0.3 at $\theta = 90$. One may argue that due to the large step, the additional fluid inflow to the rear side of the large cylinder D leads to a lower pressure coefficient in this region. Okamoto and Yagita (1973) have made a similar observation when studying flow over finite length cylinders. They argue that due to the additional inflow the *pressure recovery* at the free end behind is greater compared to that of an infinite cylinder leading to larger drag-coefficients near the free end. For the stepped cylinders, as d/D increases, the sudden drop in pressure close to the free end diminishes, and C_p varies less along the cylinder span.

Figure 5.6(a) show the distribution of the minimum value of C_p on the cylinder surface along the span. In immediate vicinity of the step a drop in pressure is observed, similar to what observed by Okamoto and Yagita (1973) at the free end of flow around a finite length cylinder. In the accompanying figure 5.6(b), the circumferential position the minimum pressure along the span is given. Again, similarities between finite length cylinders and stepped cylinders are observed for the lower d/D (Okamoto and Yagita, 1973). If flow separation occurs near the inflexion point in the C_p-θ curve (cf section 2.1.3, page 7), the point of flow separation may be assumed to follow the location of the minimum pressure (Okamoto and Yagita, 1973). It is thus possible to identify that flow separation varies in a narrow region within the step. Along the small cylinder span the separation point moves toward $\theta = 0$ as the step is approached. Earlier shedding of the vortices close to the step might explain the inclination of the vortices shed behind the small cylinder as observed in figure 5.1, page 44. The observation of a forward shifting in the separation point confirms the observation of early separation of S-cell vortices close to the step (Dunn and Tavoularis, 2006).

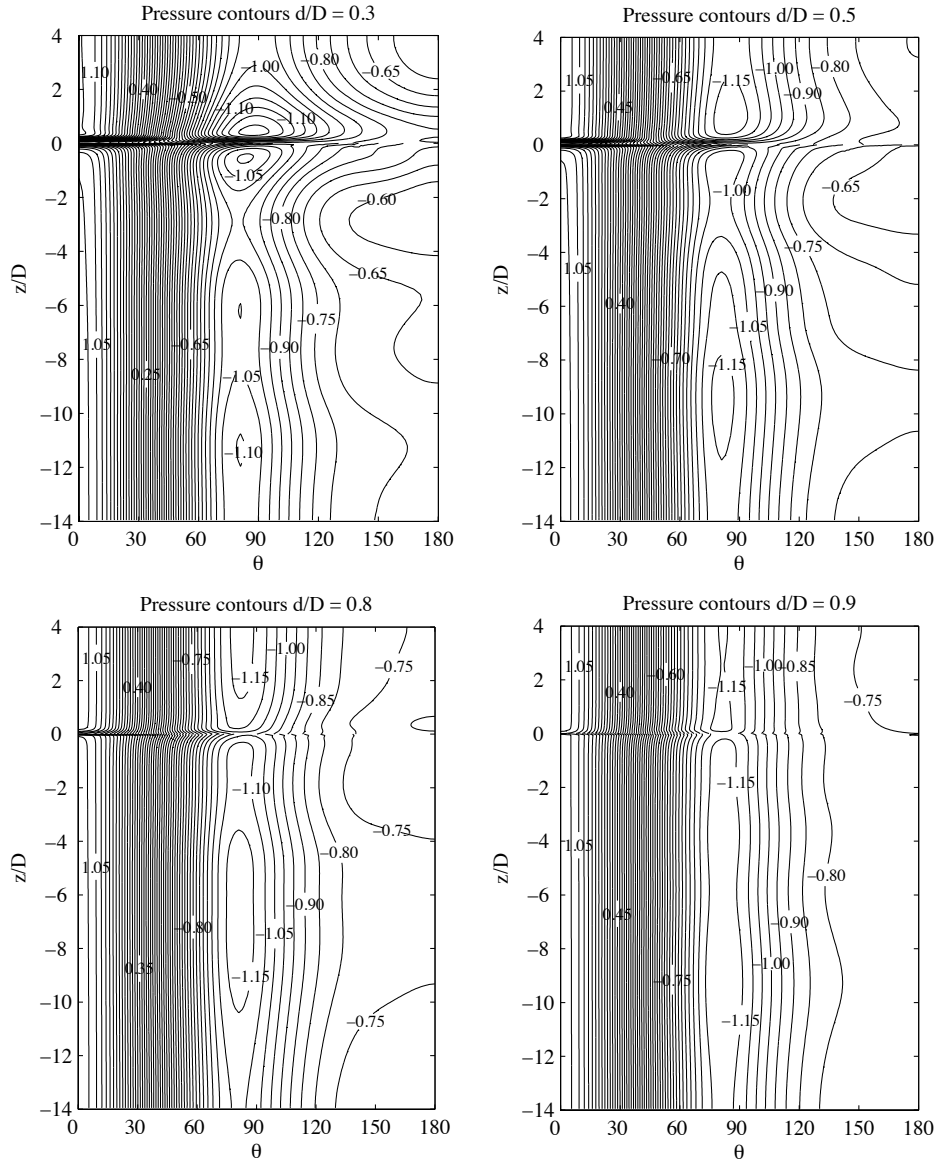

Figure 5.5: Contour plots of the distribution of the mean pressure coefficient, C_p, on the cylinder surface for stepped cylinders with d/D = 0.3, 0.5, 0.8 and 0.9. Re_D = 150.

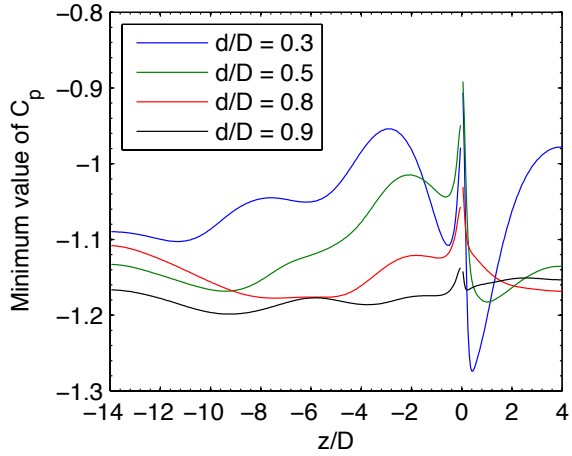

(a) Variation in the minimum value of the mean pressure coefficient, C_p, along the span

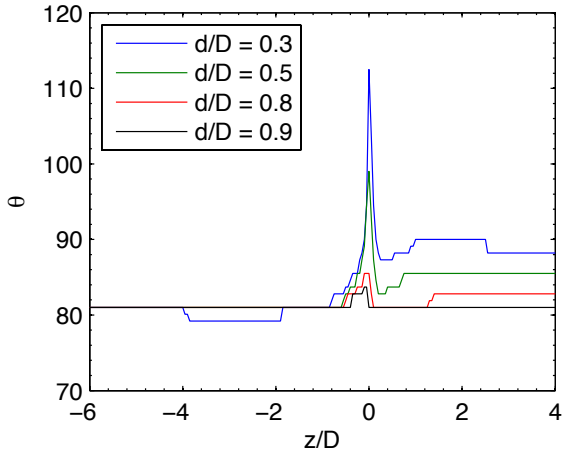

(b) Circumferential position (θ) of the minimum value of C_p along the span

Figure 5.6: Variation- and circumferential position of the mean pressure coefficient minimum along the stepped cylinder span, measured parallel to the cylinder axis at y/D = 0, x/D = 0.3. d/D = 0.3, 0.5, 0.8 and 0.9. $\mathrm{Re}_D = 150$.

5.1.5 *Drag- and lift forces*

The forces acting on the stepped cylinders have been measured as function of time. The time-series of the drag force measurement on the small and large cylinder (d and D, respectively) is shown in figure 5.7(a). Similarly, the lift-force due to periodic vortex shedding is shown in figure 5.7(b). Statistics such as $\overline{C_D}$, $C_{L\,\mathrm{r.m.s}}$ and St are given in table 5.2. The time-series were sampled when the flow was fully developed for a duration of

tU/D = 150 dimensionless time units.

The local minima and maxima in the C_D-curve have been found to coincide with vortex dislocations occurring in the wake of the stepped cylinders. A local minimum in the C_D for D is observed *prior* to the vortex dislocation in the N-L-cell boundary (cf figure 5.8, page 56). Similarly, a minimum in C_D for d is observed as a vortex dislocation occurs in the N-S-cell boundary.

The occurrence of vortex dislocations may be discerned in the time-series of the lift-coefficient, C_L, as well (figure 5.7(b)). A reduction in C_L is observed as vortices dislocate. For lower d/D the reduction is present for the large diameter cylinder D as observed for d/D = 0.5. As d/D is increased a reduction is visible for both d and D. In general C_L is reduced for d when a vortex dislocation occurs on the S-N-cell boundary, whereas a reduction in C_L for D is observed as a vortex dislocation occurs on the N-L-cell boundary.

The mean drag coefficient for D is seen increasing for increasing d/D, becoming equal to that of a straight cylinder at a similar Reynolds number. A comparison of the drag coefficient for d between the stepped cylinders is difficult as the local Reynolds number, Re_d, varies for different d/D.

The amplitude of C_L is also observed to increase for increasing d/D = 0.9. C_L r.m.s remain almost similar for d/D = 0.5 and 0.8 but experiences almost a doubling in amplitude for d/D = 0.9.

Based on the pressure contours (figure 5.5, page 50) the mean pressure induced drag coefficient variation along the span is shown in figure 5.7(c). Admittedly, at low Reynolds numbers viscous forces has a substantial contribution ($\approx$20%) and can be considered as the residue between the mean values shown in table 5.2 and the pressure induced C_D in figure 5.7(c).

Characteristic for each of the cylinders is a drop in C_D ranging from the step and about 5D into the large cylinder D. For d/D = 0.3 and 0.5 the drop is subsequent to a *rise* in C_D in the immediate vicinity of the step, extending about 0.5D into D. A similar behaviour has been observed for flow over finite length cylinders (Okamoto and Yagita, 1973) and may thus be related to the size of the step.

The rise in drag-coefficient may be tracked back to the decrease in minimum pressure close to the step (figure 5.6(a), page 51).

As the step is approached from the small cylinder side, a significant drop in C_D is observed for d/D = 0.3 and 0.5 in the immediate vicinity of the step. Prior to the drop an increase in C_D is observed, similar as for z/D < 0. This increase is most likely an effect due to the step size, but the cause has not been pursued any further in the present thesis.

Table 5.2: Statistics of the hydrodynamic forces acting on stepped cylinder with d/D = 0.3, 0.5, 0.8 and 0.9. $Re_D = 150$

		$\overline{C_D}$		St		C_L rms	
d/D	Re_D (Re_d)	D	d	D	d	D	d
0.3	150 (50)	1.214	1.605	0.173	0.145	0.105	0.001
0.5	150 (75)	1.261	1.456	0.179	0.315	0.147	0.128
0.8	150 (120)	1.290	1.326	0.178	0.214	0.147	0.191
0.9	150 (135)	1.318	1.305	0.188	0.197	0.246	0.195

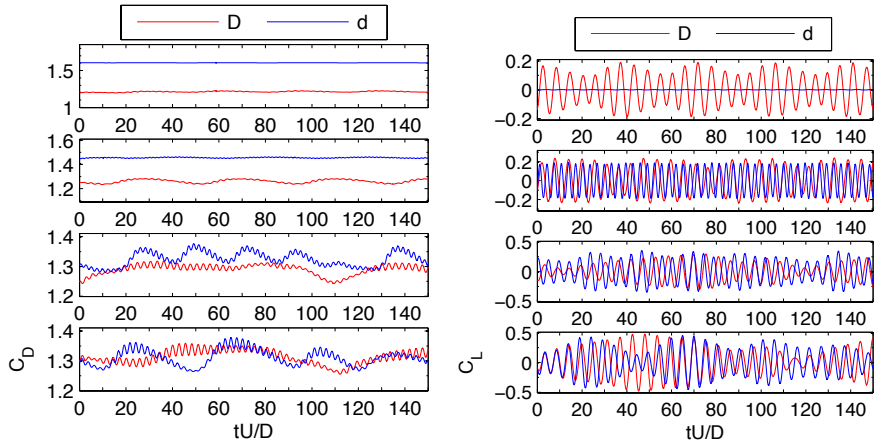

(a) C_D on d and D. From top to bottom: d/D = 0.3, 0.5, 0.8, 0.9.

(b) C_L on d and D. From top to bottom: d/D = 0.3, 0.5, 0.8, 0.9.

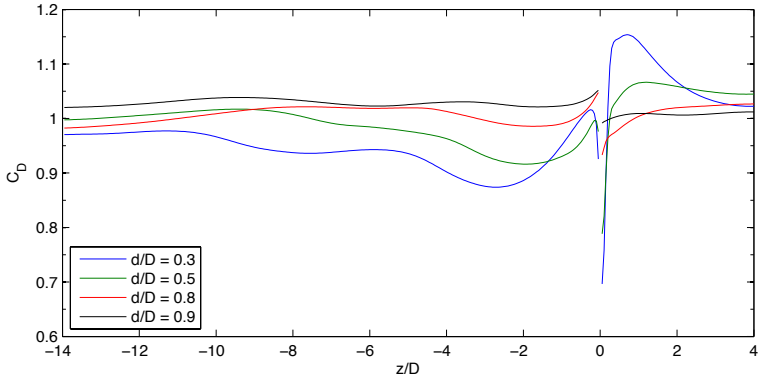

(c) Variation of pressure induced C_D along the span. Re_D = 150

Figure 5.7: (a,b): Timeseries of dimensionless drag-force, C_D, and dimensionless lift-force C_L on a stepped cylinder with d/D = 0.3, 0.5, 0.8 and 0.9, as function of dimensionless time tU/D. (c) Variation of the mean $\overline{C_D}$ along the cylinder span for d/D = 0.3, 0.5, 0.8 and 0.9. Re_D = 150.

5.1.6 Crossflow velocity fluctuations

As already indicated by the pressure contours in figure 5.5 page 50, the flow separates at different radial positions θ along the span for a stepped cylinder. It is expected that the point of flow separation varies more for lower values of d/D based on the discussion in section 5.1.4.

The crossflow velocity, v, has been sampled along a line parallel to the cylinder axis and is shown in figure 5.8. The line has been positioned in the wake at x/D = 1.8, y/D = -0.15 covering the entire span of the stepped cylinder, z/D = -14 to 4. The positioning of the line is similar to what used by Morton and Yarusevych (2010c) (x/D=2.5, y/D=0.75) in their numerical analysis of a stepped cylinder. Moreover, Visscher et al. (2011) argues that strong velocity signals have been detected at downstream positions of $2-3D_{middle}$ for flow around on tapered cylinders.

For the stepped cylinders with d/D = 0.5 it is possible to discern the S-cell, N-cell and L-cell (cf section 2.5.1, page 13) as found in previous studies (Dunn and Tavoularis, 2006; Lewis and Gharib, 1992; Morton and Yarusevych, 2010c; Norberg, 1992). Due to absent vortex shedding for d/D = 0.3 the S-cell is not identified for this case. For d/D = 0.8 and 0.9 the N-cell is difficult to discern, but regular vortex shedding in the L-cell and S-cell is present.

The time-series of the stepped cylinder with a diameter ratio d/D = 0.9, resembles that of a straight cylinder the most, with regular vortex shedding occurring in the wake. As d/D reduces, vortex dislocations occurred more frequently in the wake. Observation in time showed that as vortices shed from spanwise cells with different shedding frequency, f_v, became too much out of phase vortices dislocated. Vortex dislocations were for low d/D observed at the S-N-cell boundary, as well as N-L-cell boundary. Examples of vortex dislocations are observed along z/D = -8.5 at tU/D = 10, 45, 78, 112 and 142 behind the large diameter cylinder in figure 5.8(a). Dislocations between the S-cell and N-cell are depicted along z/D = 0.25 at tU/D = 20, 25, 30, 36 and 42 in figure 5.8(b). Admittedly, the time-series for d/D = 0.8 and 0.9 may be too brief as only one vortex dislocation is observed for d/D = 0.8 and two for d/D = 0.9.

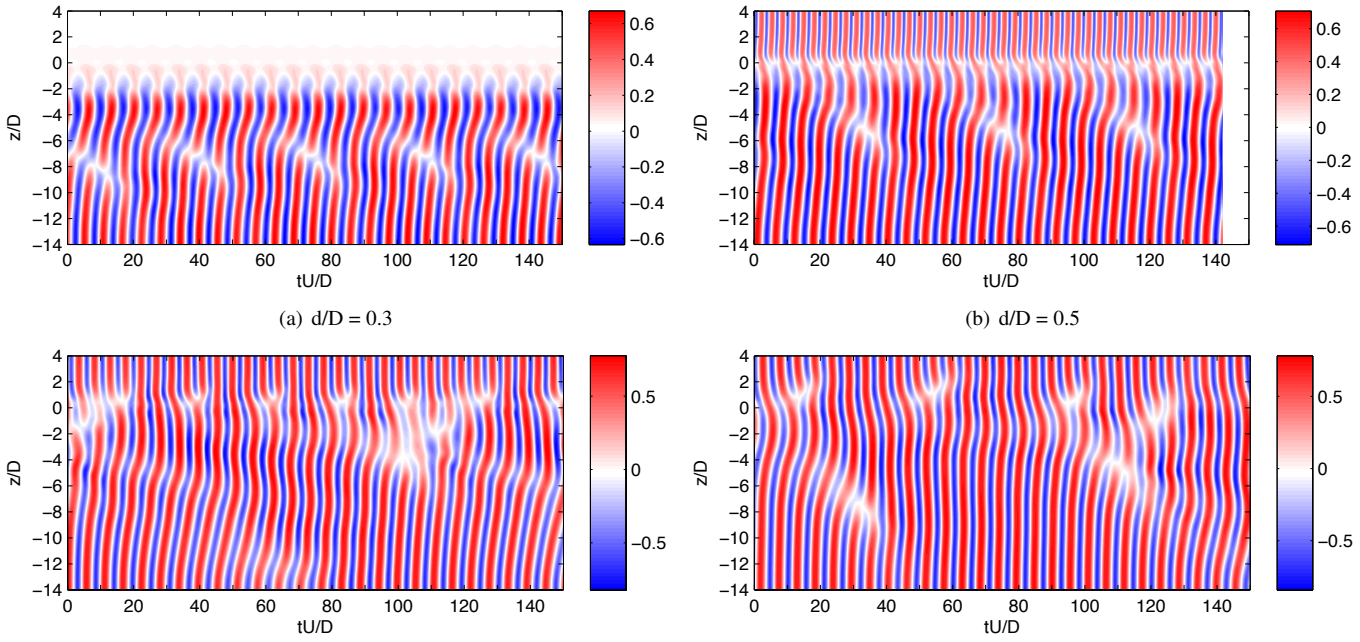

(a) d/D = 0.3

(b) d/D = 0.5

(c) d/D = 0.8

(d) d/D = 0.9

Figure 5.8: Time-series of the crossflow velocity, v, in the wake of a stepped cylinder with d/D = 0.3, 0.5, 0.8 and 0.9. The is line parallel to the cylinder axis and positioned in the wake at x/D = 1.8, y/D = -0.15. Re_D = 150.

5.1.7 Frequency analysis

The dimensionless vortex shedding frequency along the span, *St*, has been investigated based on a frequency-analysis of time-series of the streamwise velocity, u. As discussed in section 5.1.6 the velocity has been sampled along a line parallel to the cylinder axis positioned at x/D = 1.8, y/D = -0.15. For the frequency analysis, different data-acquisition rates were tested and no significant differences were found between the dimensionless sampling rates of $0.0008fD/U$ and $0.0004fD/U$ so that $0.0008fD/U$ was selected.

Based on a frequency analysis, the dimensionless vortex shedding frequency along the span is shown in figures 5.10 and 5.11, page 62. The power spectral density has been calculated based on fluctuations in the streamwise- and crossflow velocity. The spanwise vortex shedding in the L-cell, N-cell and S-cell were readily found in the frequency spectrum of v, whereas vortex dislocation frequencies additionally were detected in the spectrum based on u. Figures 5.10(a), 5.10(b), 5.10(c) and 5.10(d) thus illustrates the distribution of *St* along the span based on a frequency analysis of u. The scatter points are coloured by spectral strength. A perspective view of the variation in *St* along the span is given in figure5.11, page 62.

Table 5.3 summarises the vortex shedding frequencies detected along the span of a stepped cylinder. f_LD/U and f_SD/U represents the dimensionless vortex shedding frequencies from the large- and small diameter cylinder respectively. For smaller d/D an additional cell shedding vortices at f_ND/U was detected in proximity of the step. Strong signals were also detected in the power spectrum at the *beat* frequency $(f_L - f_N)D/U$ and $(f_S - f_N)D/U$, representing the frequency of the vortex dislocations.

Table 5.3: Dimensionless vortex shedding frequency, $St = f_vD/U$, detected along the cylinder span. $Re_D = 150$

		Dimensionless vortex shedding frequency $St = f_vD/U$				
d/D	Re_D (Re_d)	f_LD/U	f_ND/U	f_SD/U	$(f_L - f_N)D/U$	$(f_S - f_N)D/U$
0.3	150 (50)	0.171	0.143	-	0.027	-
0.5	150 (75)	0.173	0.151	0.306	0.022	0.155
0.8	150 (120)	0.172	-	0.213	0.012	-
0.9	150 (135)	0.179	-	0.193	-	-

L-cell vortex shedding

Regular spanwise vortex shedding is observed for each of the stepped cylinders. Away from the step, the dominant dimensionless vortex shedding frequency behind D is found to be similar and approximately $f_LD/U = 0.17$. In comparison, Morton and Yarusevych (2010c) reports of $f_LD/U = 0.179$ for a stepped cylinder with d/D = 0.5 at a $Re_D = 150$. It is observed that for d/D = 0.9, f_LD/U is becoming more similar to that of a straight cylinder (cf section **??**).

Regular vortex shedding in the L-cell is detected at $f_L D/U$ = 0.171 in a spanwise region of -14<z/D<-5 for d/D = 0.3 (figure 5.10(a)). As d/D increases, the spanwise range of the L-cell increases and is detected closer to the step. For d/D = 0.5 the L-cell is detected in a spanwise region of -14<z/D<-2 (figure 5.10(b)), whereas it is detected at z/D = 1.2 and 1.8 for d/D = 0.8 and 0.9 respectively (figure 5.10(c) and 5.10(d)). Hence, for the higher d/D it extends into the small diameter cylinder.

Additionally, energy is detected at several frequencies along the span of D. The small peaks detected at the higher frequencies have been identified as sums of f_L and f_N. Furthermore, the peaks identified at frequencies lower than the dominant ones, are identified at the beat frequency of f_L and f_N.

N-cell vortex shedding

As the step is approached from the large diameter cylinder the dominant vortex shedding frequency, f_L, is *modulated* into a lower shedding frequency, f_N. The frequency modulation is readily observed for d/D = 0.3 and 0.5, whereas it is not explicitly detected for d/D = 0.8 and 0.9 (figure 5.10).

A modulation of $f_L D/U$ into $f_N D/U$ is observed taking place in the region -10<z/D<-4 for d/D = 0.3. A gradual loss in energy is observed as $f_v D/U$ is shifted from $f_L D/U$ = 0.171 to $f_N D/U$ = 0.143. A similar behaviour is identified for the higher diameter ratio, d/D = 0.5. However, the modulation region is now shifted in the positive spanwise direction present at -6.8<z/D<-3. The vortex shedding frequency is here modulated from $f_L D/U$ = 0.173 into $f_N D/U$ = 0.151.

A similar modulation region has been observed by Dunn and Tavoularis (2006) and Morton and Yarusevych (2010c) for a stepped cylinder with d/D = 0.5 at $Re_D = 150$. Furthermore, for $Re_D = 6.5 \times 10^3$ Norberg (1992) detected a similar modulation region for d/D = 0.6. The ratio f_N/f_L, as well as the spanwise extension of the N-cell, has been calculated for the present results and compared to similar studies in table 5.4. Good agreement is seen between both the numerical and the experimental studies (Dunn and Tavoularis, 2006; Morton and Yarusevych, 2010c).

It is difficult to distinct an explicit N-cell for d/D = 0.8 and 0.9. It has, however, been detected in previous studies as just slightly lower than f_L (Norberg, 1992), giving the ratio f_N/f_L = 0.97. The time-series for the higher d/D could preferably have been longer, but due to limited computing power this was not feasible[2].

S-cell vortex shedding

As previously discussed in section 5.1.6, vortex shedding is absent behind the small cylinder diameter for d/D = 0.3. This may be confirmed in figure 5.11(a). For d/D = 0.5 and 0.8 the S-cell is seen extending 0.3D and 0.4D into the large diameter cylinder

[2]The HPC at NTNU was shut down in the 11th of the total 20 weeks available for the author to complete the master thesis.

Table 5.4: The ratio of f_N/f_L and the spanwise extension of the N-cell. The findings in the present thesis is compared with previous studies.

Study	d/D	Re_D (Re_d)	f_N/f_L	Extension of N-cell
Present	0.3	150 (50)	0.836	∼10D
Present	0.5	150 (75)	0.872	∼6.5D
Dunn and Tavoularis (2006)	0.5	152 (75)	0.841	∼13D (visually)
Morton and Yarusevych (2010c)	0.5	150 (75)	0.877	∼6.5D
Dunn and Tavoularis (2006)	0.5	304 (150)	0.947	∼7.3D (wavelet)
Morton and Yarusevych (2010c)	0.5	300 (150)	0.884	∼6.5D
Dunn and Tavoularis (2006)	0.5	627 (150)	-	∼5.2D
Morton and Yarusevych (2010b)	0.5	1050 (525)	0.97	∼3-5D
Norberg (1992)	0.6	6.5×10^3	0.93	∼ 7-10D

respectively. The extension of the S-cell into D has been difficult to discern for d/D = 0.9; from figure 5.10(d) the S-cell is detectable 2.8D into D thus differ quite much from d/D = 0.5 and 0.8.

For stepped cylinders with d/D = 0.5 - 1.0 and $Re_D \sim 10^3$, Norberg (1992) observed that the region associated with $f_S D/U$ extended 1D into D for d/D = 0.5 and 0.6. For a d/D = 0.8 it extended 2D or more. One might therefore question if the length of the time-series is adequate as the result deviates from the trend. This matter should be investigated in further work by longer time-series and possibly better numerical tools.

Vortex dislocation frequency

As discussed in section 5.1.6, vortex dislocations are present in the wake of the stepped cylinders. Due to different vortex shedding frequencies in the L-cell, N-cell and S-cell the number of shed vortices in the cells is different. A vortex dislocation thus occurs when a vortex in a shedding cell does not form a direct connection to a counterpart in an adjacent cell. By means of the Q-criterion vortex dislocations at the L-N-cell and N-S-cell boundary are illustrated in figure 5.9.

For d/D < 1 vortex dislocations vortex dislocations are expected to occur at the boundary of the S-cell and N-cell, and N-cell and L-cell. Due to a larger difference in shedding frequency between the N-cell and S-cell vortices(table 5.4), vortex dislocations occurs more frequently at the N-S-cell boundary. This may also be identified from figure 5.8.

Vortex dislocations have been detected at the beating frequencies $(f_L - f_N)D/U$ and $(f_S - f_N)D/U$ for the stepped cylinders in figure 5.10. Furthermore, nearly all the energy peaks located at lower fD/U in figure 5.10, are beat frequencies calculated as the difference between higher frequencies.

The beat frequency is readily detected for d/D = 0.3 and 0.5 as $(f_L - f_N)D/U$ = 0.027 and 0.022. In figures 5.10(a) and 5.10(b) energy is located at approximately these frequencies,

extending 8D and 6.5D respectively, in the spanwise direction. It should be noted that this frequency is equal to the modulation of the shedding in the L-cell. Further, its spanwise extension covers the region of modulation. For d/D = 0.8 and 0.9 energy is located at the beat frequencies but a distinct peak as for d/D = 0.3 and 0.5 is difficult to discern.

For d/D = 0.8 the vortex dislocation frequency between the S-cell and L-cell is located at $(f_S - f_L)D/U$ = 0.2137 - 0.1721 = 0.042, ranging from 0.5 $<$ z/D $<$ 1.8. Similarly, for d/D = 0.9, a vortex dislocation frequency between the S-cell and L-cell is located at $(f_S - f_L)D/U$ = 0.1934 - 0.1745 = 0.018, in the range 1.4 $<$ z/D $<$ 1.8. For d/D = 0.5 the vortex dislocation frequency between the S-cell and N-cell, $(f_S - f_N)D/U$ = 0.306 - 0.151 = 0.155 is difficult to discern at it is located at approximately $f_N D/U$ = 0.151.

However, the vortex dislocation periods, $1/((f_S - f_N)D/U)$, $1/((f_L - f_N)D/U)$, $1/((f_S - f_L)D/U)$ may be investigated visually in figure 5.8. For d/D = 0.3 this means a dimensionless period of TU/D = 37 between dislocations at the N-L-cell boundary. For d/D = 0.5 the dimensionless period between dislocation in the N-L-cell boundary is TU/D = 45.45, whereas TU/D = 6.6 for dislocations in the N-S-cell boundary.

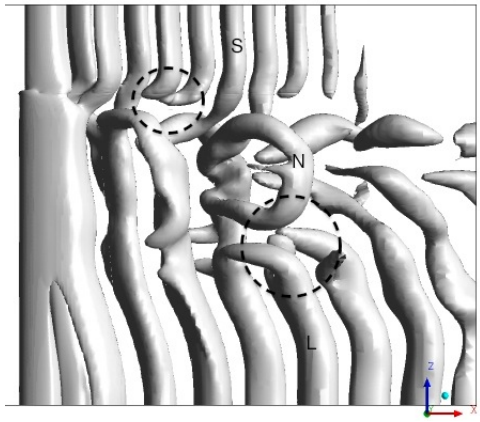

Figure 5.9: The wake flow behind a stepped cylinder with d/D = 0.5 at $Re_D = 150$ depicted by means of the Q-criterion. S-cell, N-cell and L-cell vortices are marked by the letters S, N and L. Dislocations in the N-S-cell and N-L-cell are marked by the dotted lines.

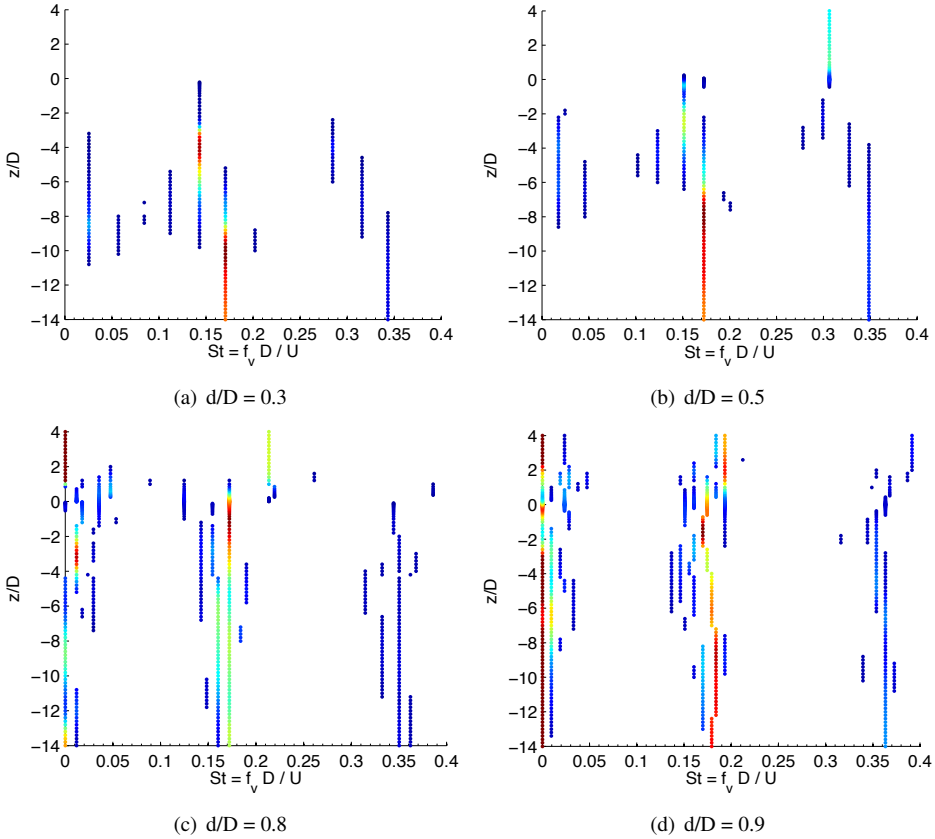

(a) d/D = 0.3

(b) d/D = 0.5

(c) d/D = 0.8

(d) d/D = 0.9

Figure 5.10: Scatter plot of the streamwise velocity spectra for a stepped cylinder with d/D = 0.3, 0.5, 0.8 and 0.9. The discrete scatter points represent spectrum energy ranging from low (blue) to high (red). Re_D = 150.

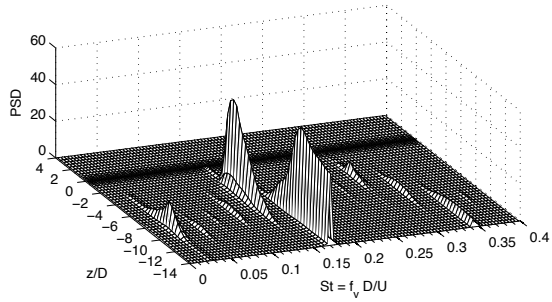

(a) d/D = 0.3

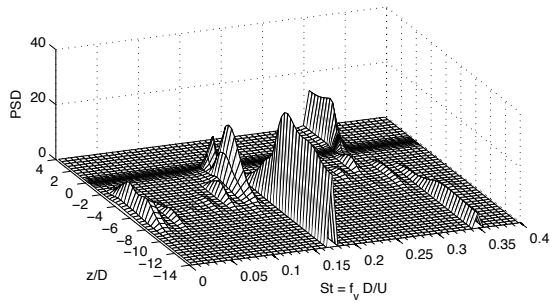

(b) d/D = 0.5

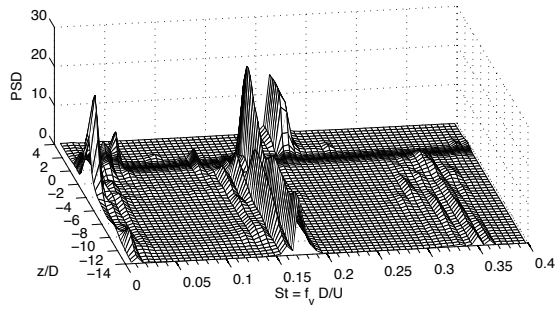

(c) d/D = 0.8

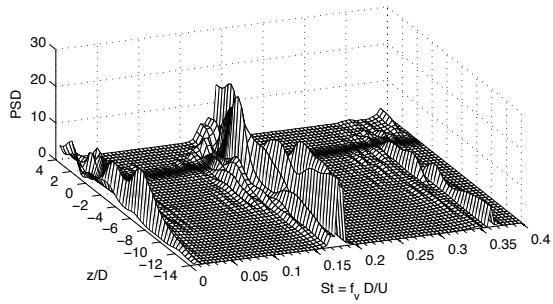

(d) d/D = 0.9

Figure 5.11: Perspective view of the streamwise velocity spectrum for a stepped cylinder of d/D = 0.3, 0.5, 0.8 and 0.9. Re_D = 150.

5.1.8 Instantaneous Vortical Structures

Figures 5.12 - 5.15 show vortical structures in the wake by means of iso-surfaces of the Q-criterion (cf section 3.6, page 33). A perspective view, allowing to observe the three-dimensionality of the flow is shown for d/D = 0.3, 0.5, 0.8 and 0.9 at $Re_D = 150$.

The Q-criterion iso-surface value was set to $\approx 2.3s^{-2}$ in all figures. The stepped cylinders are placed at the very left in the figures, covered by sheaths of Q-criterion, an effect discussed in section 3.6. The S-cell, N-cell and L-cell have been depicted to illustrate their instantaneous spanwise extension.

The present section ends by examining vortical wake structures at higher Reynolds numbers.

$Re_D = 150$

The S-cell, N-cell and L-cell is readily identified for d/D = 0.3 and 0.5 in figures 5.12(a) and 5.12(c), respectively. The vortex shedding behind d for d/D = 0.3 is absent as discussed in section 5.1.1 page 43. In the wake of the stepped cylinder with d/D = 0.5 regular spanwise vortex shedding is observed. Most vortices in the L-cell connected directly to vortices in the N-cell. The S-cell vortices without a counterpart in the N-cell, are seen forming a looped connection to a subsequent counter rotating vortex within the same cell. This event typically occurred at a vortex dislocation.

For low d/D streamwise connections between subsequent N-cell vortices were observed frequently. For higher d/D such streamwise connections were observed close to vortex dislocations. Dunn and Tavoularis (2006) argues that connections between subsequent N-cells are present due to varying strengths of the vortices in the N-cells and S-cells. When the stronger N-cell vortex connects to the weaker S-cell vortex, the remains of circulation (vortex strength) in the N-cell vortex requires a connection to a third vortex for its strength to be constant along its length (Dunn and Tavoularis, 2006). A reason for streamwise connections not occurring for higher d/D might thus be due to similar strength in the S-cell vortices and N-cell vortices.

It is interesting to observe the highly three-dimensional character of the streamwise connection between the N-cells vortices. The streamwise vortices crosses the wake, overlapping each other, connecting the N-cell vortices. The flow around d/D = 0.3 close to the step is similar to the flow around the free end of a finite length cylinder (personal communication with Levold (2012)). One explanation to why the streamwise connection exist for d/D = 0.3 may be that the N-cell vortices cannot terminate in the fluid (Dunn and Tavoularis, 2006), instead they form looped connection to a subsequent N-cell vortex.

It is interesting to determine when a typical stepped cylinder behaviour presents itself. From the limited number of diameter ratios tested, d/D = 0.8 may represent a limit to when the flow becomes affected by the step size. In the present thesis a limited time-series of d/D = 0.8 and 0.9 makes a conclusion based on the frequency analysis difficult. However, figure 5.13(a) might show the presence of an N-cell, making it more

similar to d/D = 0.3 and 0.5 than previously assumed by the frequency analysis in section 5.1.7. A similar observation has been done by Lewis and Gharib (1992) and they conclude that for low Reynolds number, d/D = 0.8 marks the limit between a *indirect* and *direct* mode.

For d/D = 0.9, vortex dislocations are observed in a close proximity to the top boundary (figure 5.13(c)). The top boundary might not be far enough away in the spanwise direction to not affect the solution, and in further work the spanwise domain should possibly be extended.

$Re_D = 300$

As the Reynolds number is increased beyond $Re > 230 \sim 250$ small scale streamwise vortices start developing (Williamson, 1996). This section thus examines, visually, how the instantaneous wake flow is affected by the streamwise vortices.

The Reynolds number is first increased to $Re_D = 300$. The Q-criterion show the wake structures for a stepped cylinder with d/D = 0.3, 0.5, 0.8 and 0.9 in figure 5.14. Contrary to Re_D vortex shedding is now present for both d and D in each of the stepped cylinders. However, due to the increased Re_D the wake flow has been increasingly distorted by the streamwise vortices.

For each of the stepped cylinders, *mode B* (Williamson, 1996) is observed behind the large diameter cylinder D. The regular spanwise vortex shedding is still discernible but identification of streamwise connections between the N-cells, and vortex connections across the cell boundaries are difficult to determine.

For the small cylinder diameter d, the flow is two-dimensional for d/D = 0.3 and d/D = 0.5 ($Re_d = 100$ and 150 respectively) whereas *mode A* is observed behind d for d/D = 0.8, characterised by a "waviness" of the spanwise shed vortices, and large scale streamwise vortices. For d/D = 0.9 *mode B* is present behind both d and D.

It is interesting to observe the wake flow behind the stepped cylinder with d/D = 0.3. It is identified that regular spanwise vortex shedding is *suppressed* in the vicinity of the step and is detected until z/D $<$ -2. Further, vortices from the S-cell are not detected connecting to the N-cell for a Q-criterion of $2.3s^{-2}$.

$Re_D = 600$

The instantaneous wake flow have been investigated at a Reynolds number $Re_D = 600$ for the stepped cylinders with a diameter ratio, d/D = 0.3 and 0.8. It should be noted that a laminar model is still employed which might be questionable as the Reynolds number is increased beyond $Re_D = 300$. However, this fact have not been studied any further.

Although the flow is highly detailed with small scale streamwise vortices the large spanwise vortex structures are discernible in the stepped cylinder wake for $Re_D = 300$ and 600. Contrary to $Re_D = 300$ *mode B* is now detected behind the small

cylinder d for d/D = 0.8.

Similarly to $Re_D = 300$ a connection between vortices from the S-cell and N-cell was not detected for $Re_D = 600$, probably because of a too high value of the Q-criterion. The wake flow behind the small cylinder diameter is still outside the critical Reynolds number Re_d for any streamwise vortices to exist.

Regular vortex shedding on the large diameter cylinder is, similarly to $Re_D = 300$ shifted in the negative spanwise direction on D.

It is interesting to observe the pair streamwise vortices extending from the step until the end of the domain. The presence of such a pair of streamwise vortices have been solely detected for $Re_D = 600$. Both edge vortices and a junction vortex were observed to exist for a d/D = 0.3 (cf section 5.1.3, page 45), but were for lower Reynolds numbers not detectable at downstream positions of x/D > 1.5. Hence, it may be a Reynolds number effect. Due to limited time this matter has not been pursued any further.

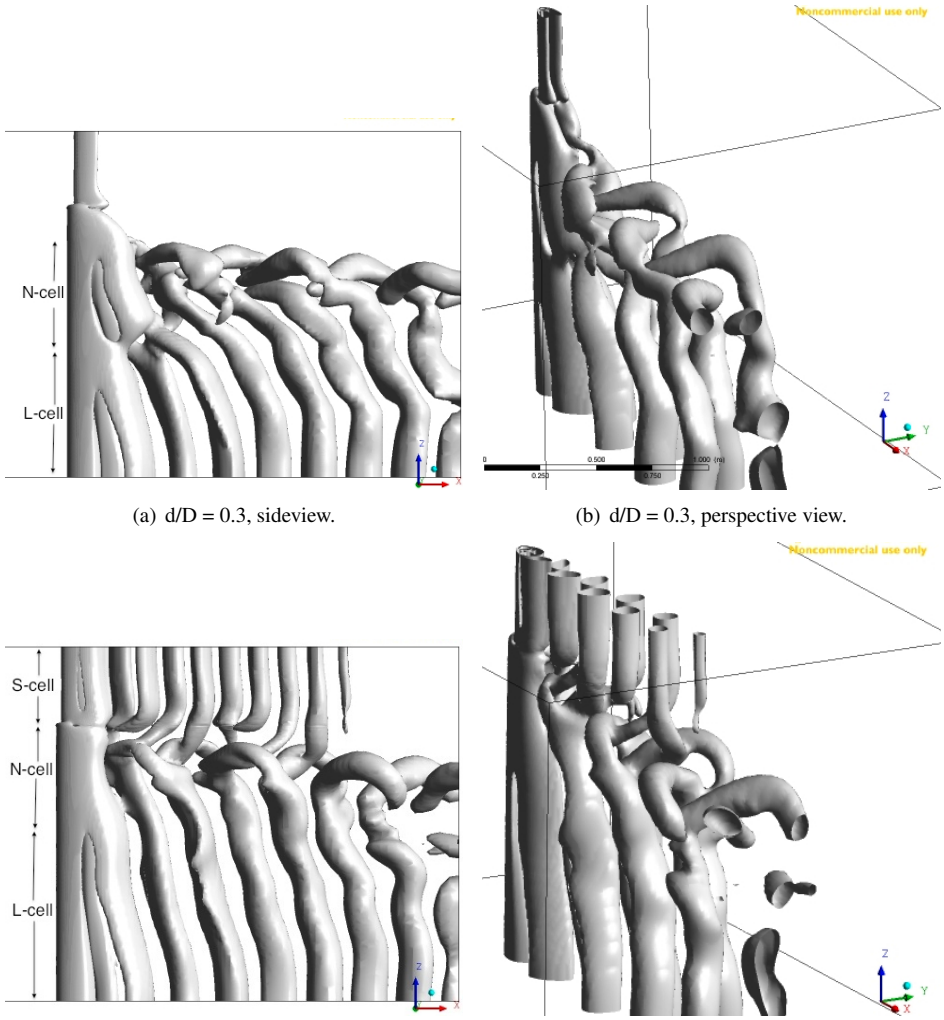

(a) d/D = 0.3, sideview.

(b) d/D = 0.3, perspective view.

(c) d/D = 0.5, sideview.

(d) d/D = 0.5, perspective view.

Figure 5.12: Isosurface of Q-criterion, $Q \approx 2.3s^{-2}$, for a stepped cylinder with d/D = 0.3, 0.5. (a,c) contains a sideview of the wake, whereas (b,d) provides a perspective view into the wake to elucidate three-dimensional effects. $Re_D = 150$.

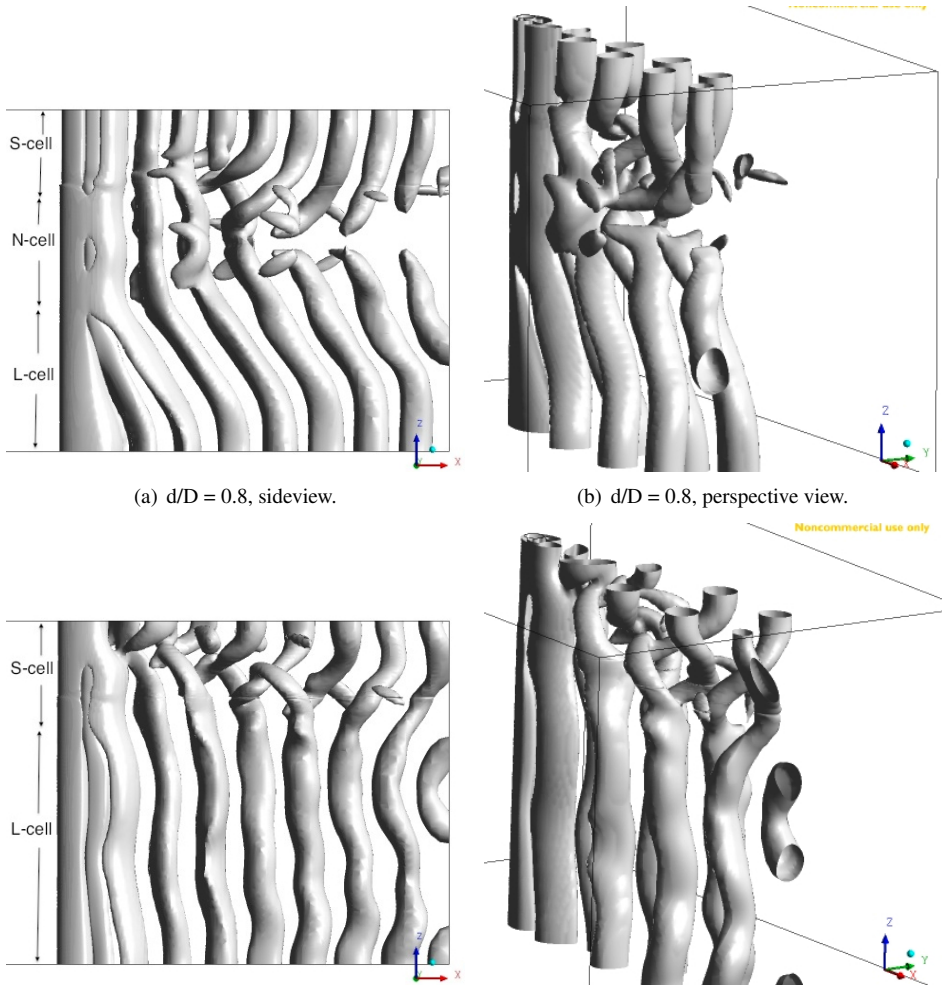

(a) d/D = 0.8, sideview.

(b) d/D = 0.8, perspective view.

(c) d/D = 0.9, sideview.

(d) d/D = 0.9, perspective view.

Figure 5.13: Isosurface of Q-criterion, $Q \approx 2.4s^{-2}$, for a stepped cylinder with d/D = 0.8 and 0.9. (a,c) contains a sideview of the wake, whereas (b,d) provides a perspective view into the wake to elucidate three-dimensional effects. Re_D = 150.

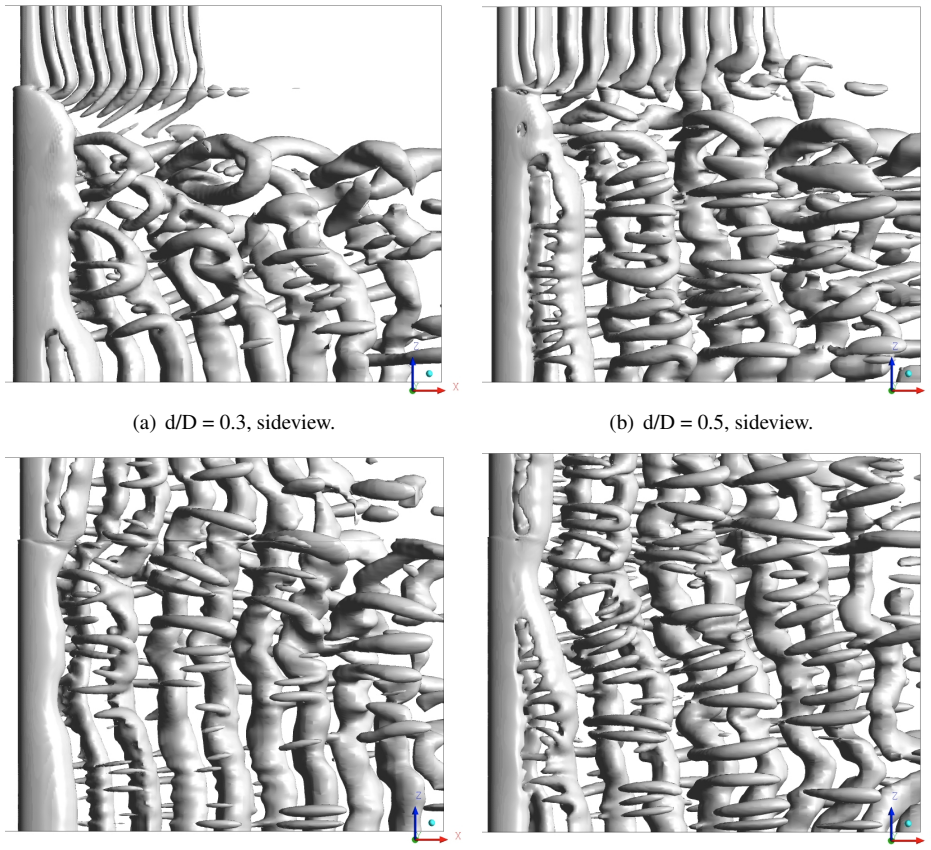

(a) d/D = 0.3, sideview.

(b) d/D = 0.5, sideview.

(c) d/D = 0.8, sideview.

(d) d/D = 0.9, sideview.

Figure 5.14: Isosurface of Q-criterion, $Q \approx 2.2s^{-2}$, for a stepped cylinder with d/D = 0.3, 0.5, 0.8 and 0.9. (a:d) contains a sideview of the wake. Re_D = 300.

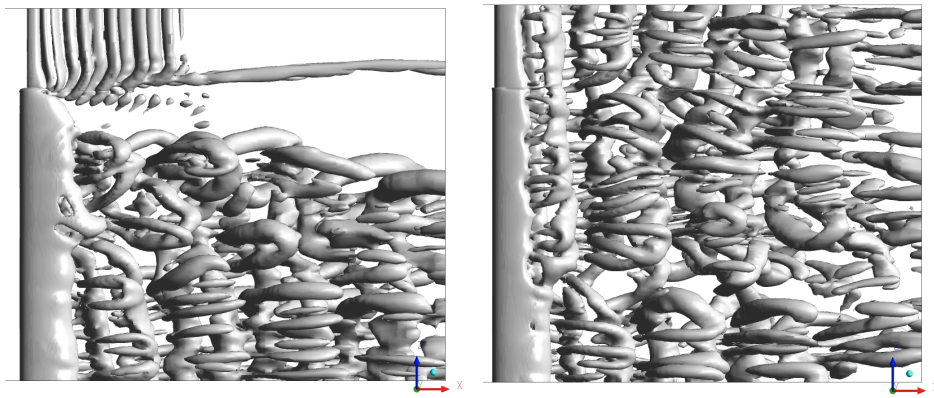

(a) d/D = 0.3, sideview.

(b) d/D = 0.8, sideview.

Figure 5.15: Isosurface of Q-criterion, $Q \approx 2.2 - 2.4s^{-2}$, for a stepped cylinder with d/D = 0.3, 0.8 (a,b) contains a sideview of the wake. Re_D = 600.

Chapter 6

Conclusion

6.1 Conclusion

The flow around stepped cylinders with a diameter ratio, d/D = 0.3, 0.5, 0.8 and 0.9 was investigated numerically for Reynolds number, $Re_D = 150, 300$ and 600. From the results of the study the following conclusion were drawn:

- **Agreement with previous studies**. The results show good agreement with previous studies, for similar diameter ratios and Reynolds numbers (Morton and Yarusevych, 2010c). For d/D = 0.8 the present observations deviate some from what obtained by Norberg (1992) and may be explained by brief time-sampling.
- **Spanwise velocity at the step**. For the stepped cylinders with lower diameter ratios, d/D = 0.3 and 0.5, significant spanwise velocity was detected in the step region. The change in diameter caused a strong upflow over the leading edge of step for d/D = 0.3 and 0.5. At the trailing edge of the step strong downwash was detected for d/D = 0.3 and 0.5, believed to be caused by additional inflow into the wake of the large diameter cylinder, D.
- **Extent of step effects**. The step was found to affect the flow $\approx$ 10D into D independent of diameter ratio for $Re_D = 150$. •The wake flow behind the small diameter cylinder was less affected by the step than the large for d/D < 0.5, as most vortex connections occurred at the step and below. For higher d/D, vortex connections took place above the step thus affecting the wake flow behind d.
- **Streamwise vortices**. In the step region two distinct streamwise vortices were detected. A pair of edge vortices as well as a junction vortex were readily detected for d/D = 0.3 and 0.5. Due to a small step the junction vortex was not detected for d/D = 0.8 and 0.9, and the edge vortices were reduced in strength.
- **Surface pressure distribution**. The surface pressure on the stepped cylinders showed that the point of flow separation varied along the cylinder span. Larger variation was found for low d/D. Similarities to the flow around a finite length cylinder could be drawn for d/D = 0.3 and 0.5, whereas d/D = 0.8 and 0.9 resembled that of a straight cylinder.
- **Periodic drag- and lift forces**. The drag force on D was found to increase as d/D increased. The amplitude of the lift force was also found to increase as d/D increased. The reduction in amplitude for low d/D is believed to be in close relation to the varying vortex shedding frequency along the cylinder span.

- **Local mean drag force**. The mean pressure induced drag-coefficient varied along the span. Peaks in the local drag-coefficient were observed in close vicinity of the step. The variation in drag-coefficient was larger for smaller d/D.
- **Spanwise vortex shedding frequency**. Regular spanwise vortex shedding was detected away from the step at a frequency similar to that of a straight cylinder. In the step region, located mainly on D, a cell of lower vortex shedding frequency was detected for d/D = 0.3 and 0.5. As d/D increased this cell seemed to disappear.
- **Wake vortex structures**. By using a vortex identification scheme vortex structures in the wake was examined. The vortex structures revealed a possible vortex shedding cell close to the step - not revealed by the frequency analysis for d/D = 0.8. Suppression of regular vortex shedding close to the step for d/D = 0.3 was observed for $Re_D = 150, 300$ and 600. Due to a difference in vortex strength, streamwise vortices were observed connecting spanwise vortices close to the step. For $Re_D > 150$ the large spanwise vortex structures were still discernible, but the presence of small scale streamwise vortices complicated the flow.

6.2 Relevance to marine applications

The Reynolds number employed in the present thesis ($Re_D < 600$) represent an idealistic case and does not represent real conditions. In real life conditions the Reynolds number on a SPAR buoy of diameter, say, D = 50m in a current of U = 1 m/s is in the range of 50×10^6. Both the drag-coefficient, $C_{L\,\mathrm{r.m.s}}$ and dimensionless vortex shedding frequency *St* varies as function of the Reynolds number. Regardless of this, studying the physics of the problem, and the qualitative behaviour of the flow problem is important. The quantities may not be correct but the general behaviour *may* observed in the laminar be similar for, say, a much higher Reynolds number. Different vortex shedding cells seem to be a feature of the step size, not the Reynolds number (Norberg, 1992). Similarly an increase in drag-coefficient is most likely present for a full scale *Re* as well. The downwash detected in the wake of the cylinder with a large step will probably be *larger* for higher Reynolds number and the streamwise vortices may exist as well.
In the following possible utilisation of the stepped cylinder features are given:

- **Vortex shedding depression**. For low d/D it is observed (figure 5.14(a) and 5.14(b) , page 68) that regular vortex shedding is depressed in the spanwise direction. Such a stepped configuration could be used to avvoid vortex induced vibrations/motions.
- **Flow at the step**. For low d/D a recirculating bubble of fluid is present at the step (figure 5.3(b), page 47). Furthermore, high frictional forces is also detected at the leading edge of the step due to high upflow velocities over the leading edge. The streamwise vortices (figure 5.4(b), page 48) should also be kept in mind for any operation taking place at, or around the step. If a mooring system is to be attached close to the step, one should be aware of the interaction possibly existing between the streamwise vortices and the system.
- **Spanwise variation in drag-coefficient**. The mean pressure drag-coefficient varies along the span a stepped cylinder with low d/D (figure 5.7(c), page 54). Peaks in

the drag-coefficient exist in close proximity to the step. Moreover, if a free-surface boundary condition is introduced, this will probably have an additional effect of the distribution of C_D, and should this effect should be pursued in further work.

6.3 Recommendations for further work

This thesis has just scratched the surface of possible studies of a stepped cylinder. A limited number of studies of flow around stepped cylinders have been published - the majority studying large aspect ratio cylinders with varying diameter ratio. Only four published numerical studies exist to this day (Morton and Yarusevych, 2010a,c; Morton et al., 2009; Vallés et al., 2002a), and they all consider uniform flow around a single stepped cylinder with d/D = 0.5. Examples of interesting topics concerning the stepped cylinder could be:

- Study the flow around stepped cylinder with very low d/D. Interesting wake flow behaviour is observed in figures5.14(a) and 5.15(a). How is the flow affected by an even smaller diameter d? (*This implicates that Re_D needs to be increased to have vortex shedding on both cylinders*)
- The higher d/D has in this thesis shown to behave quite differently than the low d/D with vortex connections between the S-cell and N-cell occurring above the step. A limit to where the N-cell becomes present is suggested to be for d/D $\leq$ 0.8. Furthermore, a proper explanation to why the N-cell exists has not been given in the literature, but downwash is suggested as the cause (Dunn and Tavoularis, 2006; Morton and Yarusevych, 2010c; Yagita et al., 1984).
- Study the flow around a stepped cylinder at an angle of attack
- Study the flow around a surface piercing stepped cylinder, and how the submergence of the step changes the flow. (*The reader may find the following paper interesting: Kawamura et al. (2002)*)
- Design the large diameter cylinder as a finite length cylinder, and study how the step and free-end behaves together. (*This creates a need for grid refinement at both the step and free end, which could possibly be computer demanding*)
- Varying the aspect ratios of the larger diameter cylinder, L/D, and small diameter cylinder l/d, and study how this affects the spanwise extents of the vortex shedding cells.
- Another interesting study would be interaction of buoy to ship interaction. Let the buoy have a stepped cylinder geometry and simulate how the presence of the ship affects the vortex shedding in the wake of the buoy.
- There is currently no existing study of a stepped cylinder that is free to oscillate in a uniform flow. This could possibly be implemented in a numerical solver and vortex induced motion (VIM) could be studied. An interesting matter would be if VIM is less for a stepped cylinder compared to a straight one.

Chapter A

St-Re Cd-Re

A.1 Div.

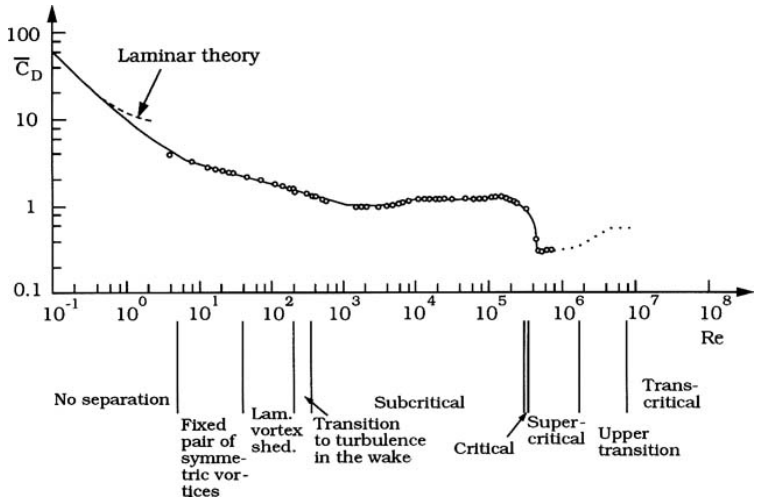

Figure A.1: C_D-*Re* relationship. Reprinted from Sumer and Fredsøe (1997)

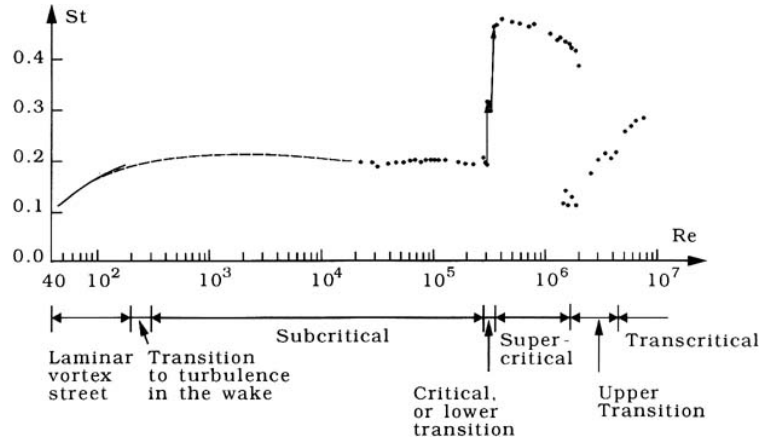

Figure A.2: *St-Re* relationship. Reprinted from Sumer and Fredsøe (1997)

Chapter B

Grid convergence study

B.1 Grid topology

Figure B.1 describes the flow topology used. Table. XX shows the element distribution in the $(x-y)$-planes for the different grids.

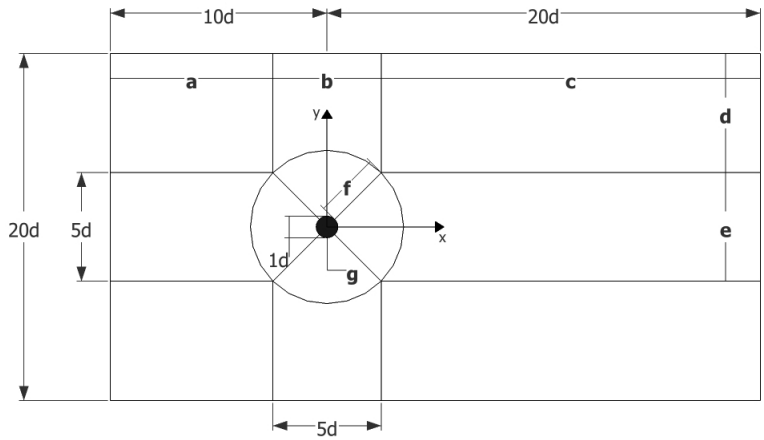

Figure B.1: Grid topology in the $(x-y)$-plane. The distribution along the edges a-f is shown in table. XX.

Table B.1: Distribution of nodes on edges for the different mesh used in the convergence study. S.R = sucessive ratio, F.L = first length. The column named: "*factor*", represents the spacing factor used on the specific edges for the different meshes respectively. In the second last and last row, the distance to the first node normal from the surface and number of elements in the boundary layer is given.

Edge	Mesh			Spacing of Nodes	
	A1	A2	A3	Function	Factor
a	20	20	20	S.R	1.02, 1.08, 1.08
b	20	40	50		1.00
c	40	60	60	S.R	1.02, 1.02, 1.02
d	10	20	20	S.R	1.17, 1.13, 1.13
e	20	40	50		1.00
f	30	60	70	S.R, F.L, F.L	1.1, 0.15, 0.17
g	80	160	200		1.00
1st element	$0.01d$	$0.01d$	$0.005d$		
#elements B.L	4	8	13		
Tot. elements	5200	17600	23200		

B.2 Grid resolution at the step

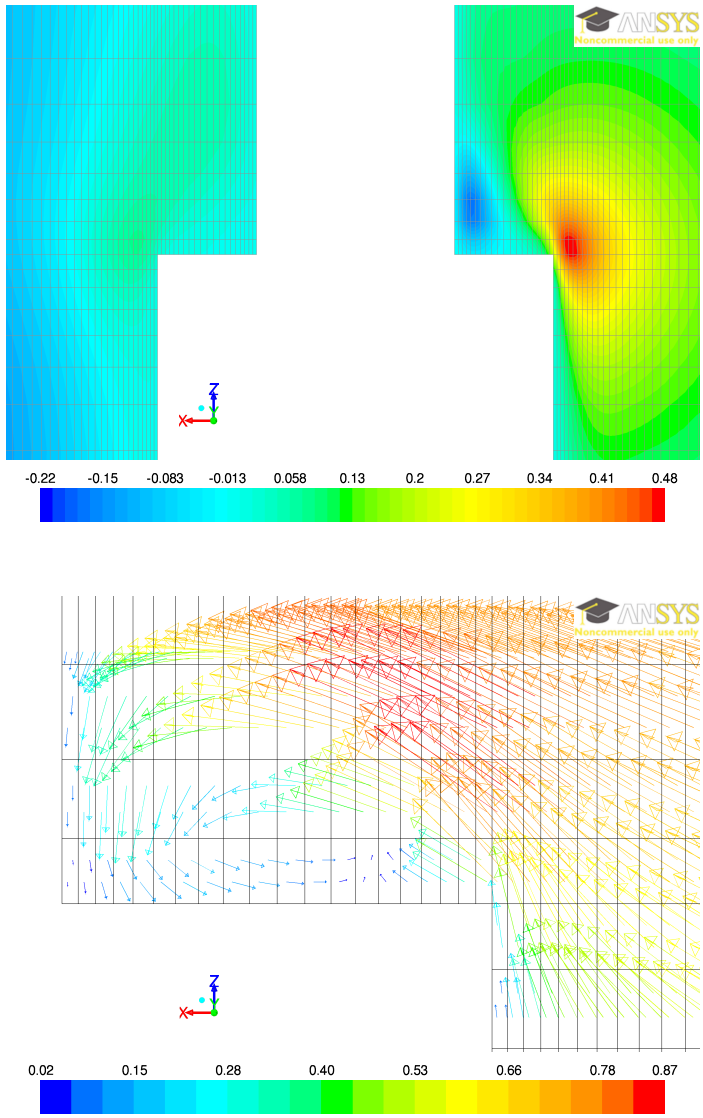

Figure B.2: Grid 10 cells.

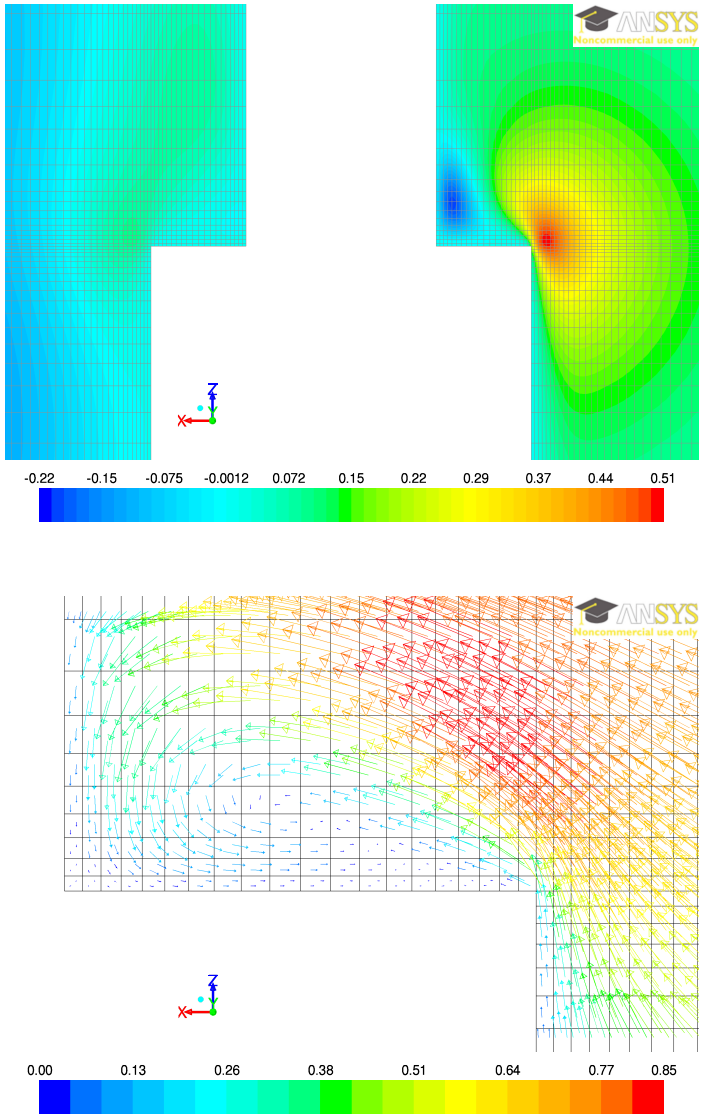

Figure B.3: Grid 10 cells.

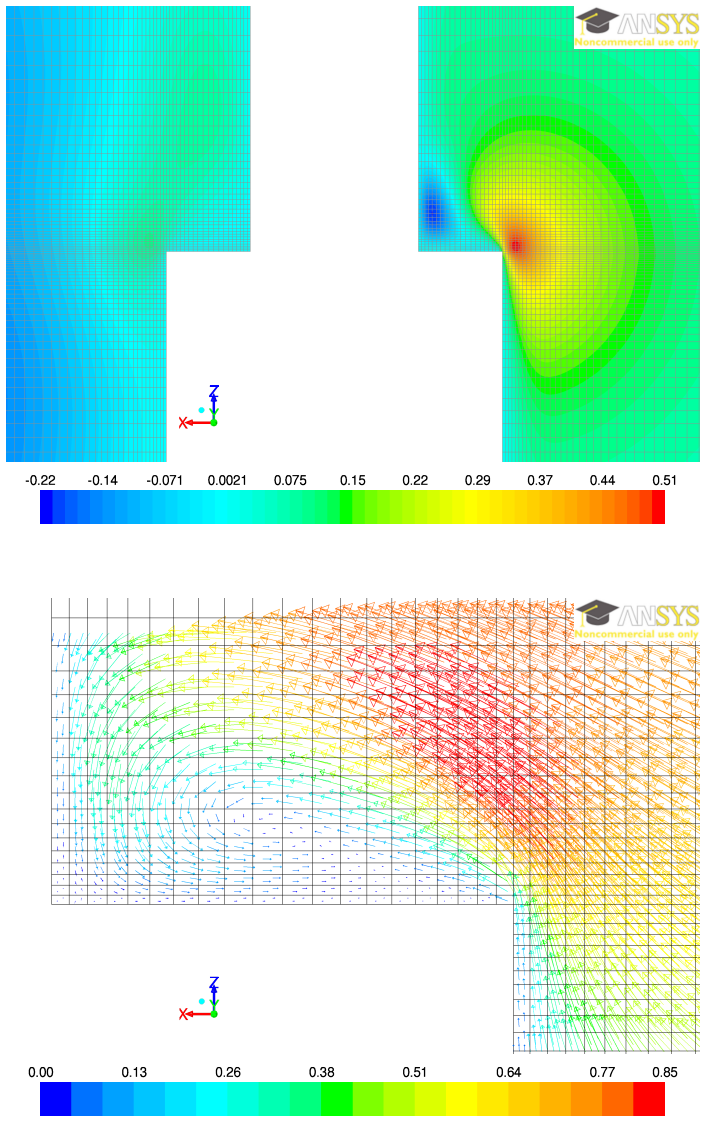

Figure B.4: Grid 10 cells.

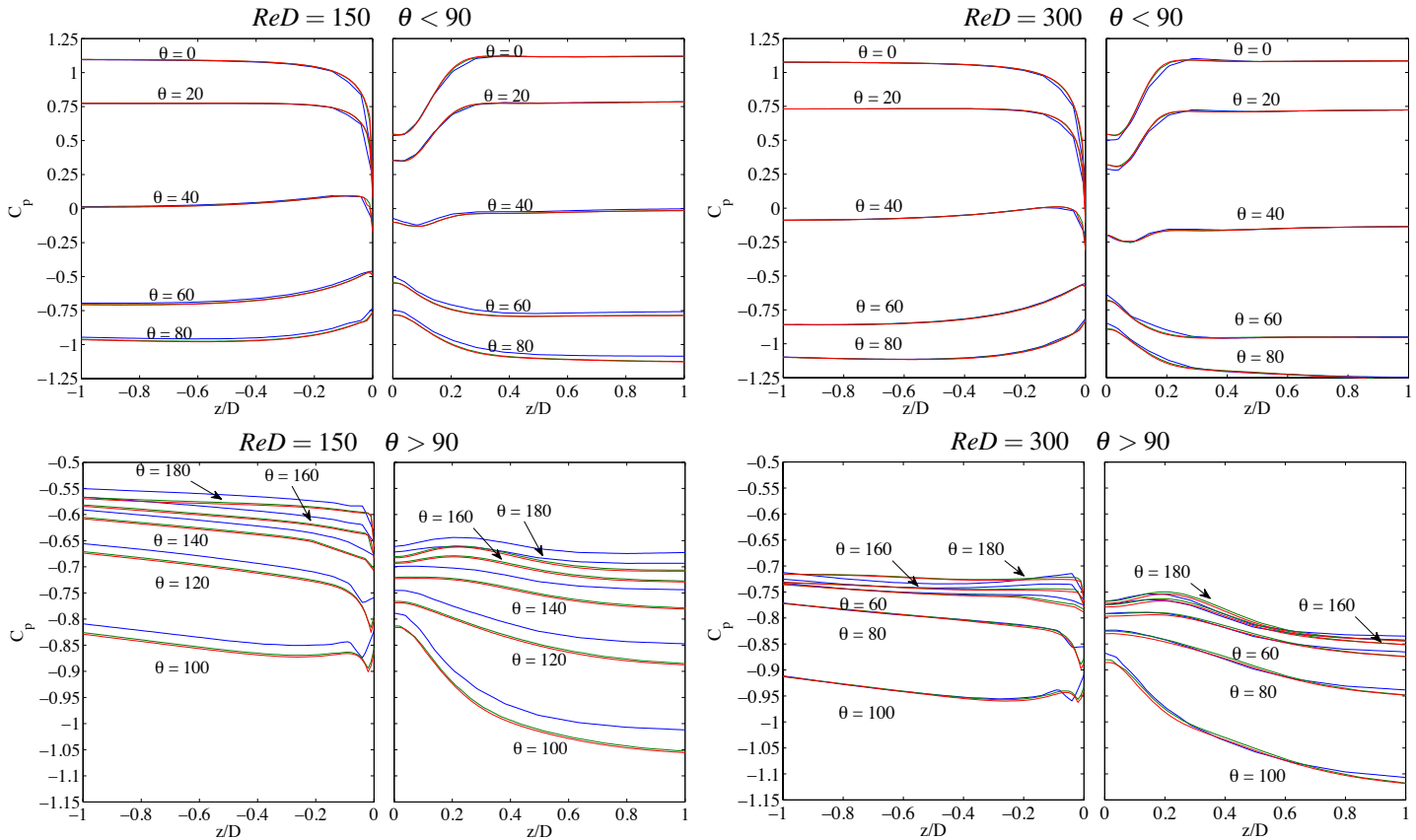

Figure B.5: Mean pressure coefficient, C_p, in the spanwise direction for different angular positions along the circumference, θ, for different grid resolutions in the step region. The grid were tested in a $ReD = 150$ and300. The blue line depicts the more coarse grid having 20 elements in the step region, whereas the green- and red lines represents distribution of 40 and 80 elements in the step region respectively.

References

Afgan, I., C. Moulinec, R. Prosser, and D. Laurence (2007). Large eddy simulation of turbulent flow for wall mounted cantilever cylinders of aspect ratio 6 and 10. *International Journal of Heat and Fluid Flow 28*, 561–574.

ANSYS (2010, November). *ANSYS FLUENT User's Guide* (13.0 ed.). ANSYS Inc.

Barkley, D. and R. D. Henderson (1996). Three-dimensional floquet stability analysis of the wake of a circular cylinder. *Journal of Fluid Mechanics 322*, 215–241.

Behr, M., D. Hastreiter, S. Mittal, and T. E. Tezduyar (1995). Incompressible flow past a circular cylinder: dependence of the computed flow field on the location of the lateral boundaries. *Computer methods in applied mechanics and engineering 123*, 309–316.

Berger, E. and R. Wille (1972). Periodic flow phenomena. *Annual Review of Fluid Mechanics 4*, 313–340.

Breuer, M. (2000). A challenging test case for large eddy simulation: high reynolds number circular cylinder flow. *International Journal of Heat and Fluid flow 21*, 648–654.

Chong, M. S., A. E. Perry, and B. J. Cantwell (1990). A general classification of threedimensional flow fields. *Physics of Fluids 2*, 765–777.

Chua, L. P., C. Y. Liu, and W. K. Chan (1998). Measurements of a step cylinder. *Int. Comm. Heat Mass Transfer 25*, 205–215.

Day, D. A. H. (2010). "theory and practice of marine cfd". Lecture notes.

Dunn, W. and S. Tavoularis (2006). Experimental studies of vortices shed from cylinders with a step-change in diameter. *Journal of Fluid Mechanics 555*, 409–437.

Gaster, M. (1969). Vortex shedding from slender cones at low reynolds numbers. *Journal of Fluid Mechanics 38*, 565–576.

Gaster, M. (1971). Vortex shedding from circular cylinders at low reynolds numbers. *Journal of Fluid Mechanics 46*, 749–756.

Hunt, J. C. R., A. Wray, and P. Moin (1988). Eddies, stream, and convergence zones in turbulent flows. *Center for Turbulence Research.*, Report CTR–S88.

Jeong, J. and F. Hussain (1995). On the identification of a vortex. *Journal of Fluid Mechanics 285*, 69–94.

Kawamura, T., M. Hiwada, T. Hibino, I. Mabuchi, and M. Kumada (1984). Flow around a finite circular cylinder on a flat plate. *Bulletin of JSME 27*, 2142–2151.

Kawamura, T., S. Mayer, A. Garapon, and L. Sørensen (2002). Large eddy simulation of a flow past a free surface piercing cicular cylinder. *Journal of Fluids Engineering 124*, 91–101.

Krajnović, S. (2011). Flow around a tall finite cylinder explored by large eddy simulation. *Journal of Fluid Mechanics 676*, 294–317.

Kravchenko, A. G. and P. Moin (2000). Numerical studies of flow over a circular cylinder

at red = 3900. *Physics of Fluids 12*, 403–417.

Lei, C., L. Cheng, and K. Kavanagh (2000). A finite difference solution of the shear flow over a circular cylinder. *Ocean Engineering 27*, 271–290.

Levold, P. (2012). Personal communication. Levold studied the flow around a finite length cylinder at Re = 100 in his MSc thesis using a numerical solver (MGLET, DNS).

Lewis, C. G. and M. Gharib (1992). An exploration of the wake three dimensionalities caused by a local discontinuity in cylinder diameter. *Physics of Fluids 4*, 104–117.

Mittal, S. (2001). Computation of three-dimensional flows past circular cylinder of low aspect ratio. *Physics of Fluids 13*, 177–191.

Morton, C. and S. Yarusevych (2010a). A combined experimental and numerical study of flow past a single step cylinder. In *Proceedings of the ASME 2010 3rd Joint US-European Fluids Engineering Summer Meeting and 8th International Conference on Nanochannels, Microchannels, and Minichannels FEDSM-ICNMM2010*, August 1-5, 2010, Montreal, Canada, pp. 1–11.

Morton, C. and S. Yarusevych (2010b). An experimental study of flow past a dual step cylinder. In *Proceedings of the ASME 2010 3rd Joint US-European Fluids Engineering Summer Meeting and 8th International Conference on Nanochannels, Microchannels, and Minichannels FEDSM-ICNMM2010*, August 1-5, 2010, Montreal, Canada, pp. 1–11.

Morton, C. and S. Yarusevych (2010c). Vortex shedding in the wake of a step cylinder. *Physics of Fluids 22*, 083602–1–12.

Morton, C. and S. Yarusevych (2011). Cross flow over cylinders with two stepwise discontinuities in diameter. In *Seventh International Symposium on Turbulence and Shear Flow Phenomenon TSFP-7*, July 28-31, 2011, Ottawa, Canada, pp. 1–6.

Morton, C., S. Yarusevych, and I. Carvajal-Mariscal (2009). Study of flow over a step cylinder. *Applied Mechanics and Material 15*, 9–14.

Narasimhamurthy, V. D., H. I. Andersson, and B. Pettersen (2009). Cellular vortex shedding behind a tapered circular cylinder. *Physics of Fluids 21*, 044106–044106.12.

Niemann, H. and N. Hölscher (1990). A review of recent experiments on the flow past circular cylinders. *Journal of Wind Engineering and Industrial Aerodynamics 33*, 197–209.

Nishino, T., G. T. Roberts, and X. Zhang (2008). Unsteady rans and detached-edyy simulations of flow around a circular cylinder in ground effect. *Journal of Fluids and Structures 24*, 18–33.

Norberg, C. (1992). An experimental study of the flow around cylinders joined with a step in the diameter. In *Proceedings of the 11th Australasian Fluid Mechanics Conference*, University of Tasmania, Hobart, Australia, 14-18th December 1992, pp. 507–510.

Okamoto, T. and M. Yagita (1973). The experimental investigation on the flow past a circular cylinder of finite length placed normal to the plane surface in a uniform stream. *Bulletin of JSME 16*, 805–814.

Park, C.-W. and S.-J. Lee (2000). Free end effects on the near wake flow structure behind a finite circular cylinder. *Journal of Wind Engineering and Industrial Aerodynamics 88*, 231–246.

Pattenden, R. J., S. R. Turnock, and N. W. Bresshof (2002). An experimental and computational study of three-dimensional unsteady flow features found behind a truncated cylinder. In *24th Symposium on Naval Hydrodynamics*, Fukuoka, Japan, 8-13 July 2002.

Persillon, H. and M. Braza (1998). Physical analysis of the transition to turbulence in the wake of a circular cylinder by three-dimensional navier-stokes simulation. *Jouranl of Fluid Mechanics 365*, 23–88.

Roshko, A. (1993). Perspectives on bluff body aerodynamics. *Journal of Wind Engineering and Industrial Aerodynamics 49*, 79–100.

Rütten, M., T. Alrutz, and H. Wendland (2008). A vortex axis and vortex core border grid adaptation algorithm. *International Journal for Numerical Methods in Fluids 58*, 1379–1405.

Schlichting, H. (1979). *Boundary Layer Theory* (Seventh ed.). McGraw-Hill.

Spalart, P. R. (2000). Strategies for turbulence modelling and simulations. *International Journal of Heat and Fluid Flow 21*, 252–263.

Sumer, B. M. and J. Fredsøe (1997). *Hydrodynamics around Cylindrical Structures*. Advanced Series on Ocean Engineering - Volume 12. World Scientific.

Sumner, D., J. L. Heseltine, and O. J. P. Dansereau (2004). Wake structure of a finite circular cylinder of small aspect ratio. *Experiments in fluids 37*, 720–730.

Travin, A., M. Shur, M. Strelets, and P. Spalart (1999). Detachted-eddy simulations past a circular cylinder. *Flow, turbulence and Combustion 63*, 293–313.

Vallés, B., H. I. Andersson, and C. B. Jenssen (2002a). Direct-mode interactions in the wake beind a stepped cylinder. *Physics of Fluids 14*, 1548–1551.

Vallés, B., H. I. Andersson, and C. B. Jenssen (2002b). Oblique vortex shedding behind tapered cylinders. *Jouran of Fluids and Structures 16*, 453–463.

Visscher, J., B. Pettersen, and H. I. Andersson (2011). Experimental study on the wake behind tapered circular cylinders. *Journal of Fluids and Structures 27*, 1228–1237.

White, F. M. (2006). *Viscous Fluid Flow* (Third ed.). McGraw-Hill.

White, F. M. (2008). *Fluid Mechanics* (Sixth ed.). McGraw-Hill.

Williamson, C. H. K. (1992). The natural and forced formation of spot-like 'vortex-dislocations' in the transition of a wake. *Joural of Fluid Mechanics 243*, 393–441.

Williamson, C. H. K. (1996). Vortex dynamics in the cylinder wake. *Annual Review of Fluid Mechanics 28*, 477–539.

Wu, M.-H., C.-Y. Wen, R.-H. Yen, M.-C. Weng, and A.-B. Wang (2004). Experimental and numerical study of the separation angle for flow around a circular cylinder at low reynolds number. *Journal of Fluid Mechanics 515*, 233–260.

Yagita, M., Y. Kojima, and K. Matsuzaki (1984). On vortex shedding from circular cylinder with step. *Bulletin of JSME 27*, 426–431.

Zdravkovich, M. M. (1997). *Flow around Circular Cylinders*. Oxford University Press.